

LOW FREQUENCY ELECTROMAGNETIC WAVE PROPAGATION IN 3D PLASMA CONFIGURATIONS

THÈSE N° 3063 (2004)

PRÉSENTÉE À LA FACULTÉ SCIENCES DE BASE

CRPP Association Euratom

SECTION DE PHYSIQUE

ÉCOLE POLYTECHNIQUE FÉDÉRALE DE LAUSANNE

POUR L'OBTENTION DU GRADE DE DOCTEUR ÈS SCIENCES

PAR

Pavel POPOVITCH

ingénieur-physicien, Institut National d'Ingénierie et de Physique, Moscou, Russie
et de nationalité russe

acceptée sur proposition du jury:

Dr W.A. Cooper, directeur de thèse
Prof. M. Deville rapporteur
Prof. A. Jaun, rapporteur
Prof. V.D. Shafranov, rapporteur
Dr L. Villard, rapporteur

Lausanne, EPFL
2004

Abstract

We investigate low-frequency electromagnetic wave propagation and absorption properties in 2D and 3D plasma configurations. For these purposes, we have developed a new full-wave 3D code LEMan that determines a global solution of the wave equation in bounded stellarator plasmas excited with an external antenna. No assumption on the wavelength compared to the plasma size is made, all the effects of the 3D geometry and finite plasma extent are included. The equation is formulated in terms of electromagnetic potentials in order to avoid numerical pollution effects. The code utilises linear and Hermite cubic finite element discretisation in the radial direction and Fourier series in the poloidal and toroidal variables. The full cold plasma model including finite electron inertia and, thus, mode conversion effects is implemented. The code uses Boozer magnetic coordinates and has an interface to the TERPSICHORE code. Special care is taken to treat the magnetic axis and to ensure the unicity of the numerical solution. The discretisation, interpolation and numerical derivation methods specifically adapted for our problem avoid the energy sink in the origin and provide a very good local and global energy conservation. A special algorithm has been developed to analytically expand the wave equation coefficients in the full 3D stellarator geometry. The code has been specifically optimised for vector computing platform, reaching close to maximum average performances on the NEC SX5 machine.

The code has been applied in 1D, 2D, and 3D geometries. No unphysical solutions have been observed. LEMan successfully recovers all the fundamental properties of the Alfvén spectrum (gaps, eigenmodes). Benchmarks have been made against the 2D LION code and JET experimental measurements, showing a good agreement between the results.

Version abrégée

Dans ce travail, on étudie la propagation des ondes électromagnétiques aux basses fréquences et les propriétés de l'absorption dans des configurations de plasmas à deux et trois dimensions. Dans ce but, on a développé un nouveau code global 3D, LEMan, qui résout l'équation d'ondes dans un plasma de taille finie avec une excitation par une antenne extérieure. La formulation du problème ne dépend pas de la longueur d'onde, tous les effets de la géométrie 3D, de l'inhomogénéité et de la taille finie du plasma sont retenus. La formulation de l'équation utilise les potentiels électromagnétiques pour éviter les effets de la pollution numérique du spectre. Le code utilise des éléments finis linéaires ou cubiques pour la discrétisation radiale et des séries de Fourier dans des variables toroïdale et poloïdale. Le modèle du plasma froid est implémenté en retenant les effets de l'inertie finie des électrons et, donc, la conversion de modes. Le code utilise les coordonnées magnétiques de Boozer. La transformation de l'équilibre magnétique dans les coordonnées de Boozer est calculée par le code TERPSICHORE. On attache une importance particulière au traitement de l'axe magnétique pour garantir l'unicité de la solution. La méthode de discrétisation, d'interpolation et de dérivation numérique est adaptée au problème pour éviter des pertes d'énergie non physiques sur l'axe et pour assurer une bonne conservation locale et globale de l'énergie. Un algorithme spécial a été implémenté pour le développement analytique des coefficients de l'équation d'onde dans une géométrie complètement 3D d'un stellarateur. Le code a été optimisé pour des calculs sur une plateforme vectorielle, il atteint une performance moyenne proche du maximum possible sur l'ordinateur NEC SX5.

Le code a été appliqué dans des géométries 1D, 2D et 3D. Aucune solution non physique n'a été observée, donc le spectre est non pollué. LEMan reproduit toutes les propriétés fondamentales du spectre d'Alfvén ("gaps", modes globaux). Des comparaisons ont été faites avec succès avec le code 2D LION, ainsi qu'avec des mesures expérimentales de JET qui démontrent un bon accord entre les résultats.

Contents

1	Introduction	1
2	Physical model	7
2.1	Plasma equilibrium	8
2.2	Coordinate system	10
2.3	Equilibrium calculations	13
2.4	Wave equations	15
2.5	Cold plasma approximation	19
2.6	Waves in cold plasma	23
3	Numerical implementation	27
3.1	Discretisation and Finite Element Method	28
3.2	Radial basis functions	32
3.3	Fourier harmonics	34
3.4	Vector projections	35
3.5	Expansion of the wave equation	36
3.6	Matrix construction	39
3.7	Construction optimisation	41
3.8	Boundary and gauge conditions	42
3.9	Unicity on the axis	43
3.10	Antenna	46
3.11	Diagnostics and power balance	48

3.12	Unicity check	52
3.13	CPU time and memory requirements	55
4	Results	59
4.1	1D cylindrical geometry	61
4.1.1	Cylindrical vacuum waveguide	61
4.1.2	Radial convergence and finite elements	64
4.1.3	Homogeneous cylindrical plasma column	70
4.1.4	Non-homogeneous plasma cylinder with current	75
4.2	2D geometry	81
4.2.1	Continuum, gaps and Toroidicity-induced Alfvén eigenmodes	82
4.2.2	Comparison with experimental data	86
4.2.3	Comparison with the LION code	88
4.2.4	Quasi-electrostatic wave	89
4.2.5	Quasi-electrostatic wave eigenmodes	95
4.2.6	Ion-cyclotron range of frequencies	98
4.2.7	Mirror	109
4.3	3D geometry	112
4.3.1	Helix	112
4.3.2	Quasi-axisymmetric device	117
4.3.3	Large Helical Device	119
5	Conclusions	125
A	Numerical pollution	129
B	Derivation of transformation matrices \widehat{TU}, \widehat{TL}	133

Chapter 1

Introduction

"The stone age did not end because we ran out of stones, and the oil age will not end because we run out of oil."

– Don Huberts, CEO Shell Hydrogen.

"Yes, my friends, I believe that water will one day be employed as fuel... Water will be the coal of the future."

– Jules Verne, Mysterious Island, 1874.

The search for new energy sources will be one of the greatest challenges of this century. The global world energy demand is ever growing not only due to the increase of the world population, but also due to the increase in the consumption per person in the industrialised and, most importantly, in the rapidly developing countries. In 1990, an average person in an industrialised country consumed about 5 tonnes of petrol equivalent of energy per year, which is about 10 times more than in developing countries. As the industry develops in these countries and the standards of living increase, the energy consumption, which is directly related to these factors, will inevitably grow. According to an estimate by the International Energy Agency (IEA), the projected primary energy demand growth rate is slower than during past 30 years (2.1% per year), but it will still represent an increase of almost two thirds by the year 2030 (about 1.7% per year). Diminishing drinking water resources will be another serious concern of this century. Purifying waste waters will

further add to the energy demand. Combined with the predicted population growth, the global energy consumption might increase by a factor of two or three by the year 2050, depending on the scenario of evolution.

Again according to the IEA, the share of fossil fuels will dominate in the global energy production, accounting for more than 90% of the increase in energy use to 2030. Fossil fuels can be only an intermediate solution to satisfy the energy needs of society. The natural resources of these fuels are limited. The already discovered oil reserves are estimated to last for several decades, natural gas and coal will last longer. However, the main concern is not there, but in the serious environmental impacts associated with the combustion of fossils. Emissions of the oxides of sulphur and nitrogen result in acid pollution, provoking asthma and other respiratory diseases. While these substances can, in principle, be filtered before the release to the atmosphere, the combustion of oil, gas and coal inevitably produces carbon dioxide. The quantity of CO₂ released by fossil powerplants and cars is feared to be already now sufficient to produce a greenhouse effect and raise the average temperature and sea level, affecting the global climate. IEA analysis shows that the rate of energy savings and the decline in CO₂ emissions relative to GDP has slowed down since 1990. In fact, the impact of the oil crisis in the 1970s and the resulting energy policies did more to control the increase in energy demand and reduce the associated CO₂ emissions than the energy and climate policies implemented in the 1990s. IEA studies on the basis of present policies predict a growth of global CO₂ emissions by about 1.8% per year from now until 2030. This represents an increase of 70% in 30 years.

It is therefore clear that oil, gas and coal cannot be a long term solution, and have to be replaced by clean sources of energy. Renewable sources, unfortunately, are unlikely to completely substitute fossil fuels. One of the major renewable forms of energy, the hydroelectric power, is not far from the limit of its development. Flooding of large areas of land and the ensuing population resettlements make hydroelectricity less attractive. Other renewable sources, like wind, solar, geothermal, tidal, biomass, etc, can be very promising for a part of energy production, particularly on a small, house-hold scale, or for remote areas. However, their potential is presently thought to be insufficient to totally

replace fossil fuels on a large, industrial or urban scale, at least in the foreseeable future.

The only non-fossil alternative presently available that can satisfy the energy requirements is nuclear powerplants. Fission can produce large amounts of energy without emissions of greenhouse gases. Unfortunately, no long-term solution has been found to the issue of the radioactive waste. This waste can remain radioactive for as long as 100,000 years and can represent a serious problem for future generations, so many countries are increasingly reluctant to build new fission plants.

Another potentially attractive alternative is the controlled thermonuclear fusion concept. It is based on fusing two light nuclei into a heavier one, similar to the processes that take place in the Sun. The reaction that would require the least (but still a huge!) effort is the fusion of deuterium and tritium that produces helium and neutron. The fuel is virtually unlimited: deuterium can be extracted from water; tritium (very rare because it is unstable) can be manufactured by bombarding the naturally occurring element lithium with neutrons from the fusion reactor itself. A fusion reactor would be inherently safe because at any moment it would contain a quantity of fuel sufficient for only a few seconds of operation. The radioactive materials produced by the exposure to the neutron flux will decay almost completely within 100 years and can be recycled.

The idea of magnetic fusion is based on the confinement by a magnetic field of a deuterium and tritium plasma heated to the temperatures of the order of ~ 10 keV sufficiently long for the reaction to produce enough energy. There are two major types of configurations adopted as possible candidates for the thermonuclear reactor. Both use a closed toroidal topology of the magnetic field. The first one, called tokamak, is based on a toroidally symmetric geometry. A pure toroidal field generated by external coils cannot confine the plasma because of particle drifts in the inhomogeneous magnetic field, so the field has to be helically twisted. Helicity is obtained by adding a poloidal component to the toroidal field. In tokamaks, this poloidal component is due to the toroidal current induced in the plasma. In the configurations of the second type, called stellarators, the poloidal field is created by external coils. While tokamak configurations have two-

dimensional symmetry, stellarators are fully three dimensional. The axial symmetry of tokamaks considerably simplifies many physical aspects and is an attractive advantage of this concept. Tokamaks have been heavily studied, and a very big progress in the confinement time and other major fusion parameters has been achieved in the past four decades.

A large-scale study of stellarators has been delayed by about 20 years with respect to tokamaks. Despite less resources invested in the stellarator program, a considerable progress has still been made. The main advantage of stellarators is due to the external generation of the confining magnetic field. Stellarators decrease the risk of the disruptive discharge termination at high plasma density and pressure. They can also allow for a steady-state operation because the need for the externally driven current is eliminated or significantly reduced. Plasma control is simplified with respect to tokamaks since it does not rely on the current drive in the plasma.

The extra dimension of stellarators, on the one hand, makes possible a large diversity of configurations and provides a large potential of optimisation. On the other hand, it greatly reduces the possibilities of analytical solutions to many physical problems and considerably complicates the numerical applications, requiring 3D codes.

One of the important aspects of fusion research is plasma heating. Electron cyclotron resonance heating (ECRH) and neutral beam injection (NBI) are two possible methods successfully applied in stellarators. However, both methods are thought to have some disadvantages. High β (plasma to magnetic pressure ratio) values in stellarators require very high level of ECRH power due to the scaling of the stellarator confinement with density n and magnetic field B . Reactor-relevant low ion collisionality regime studies require low n at high ion temperature T_i , i.e. the combination of parameters where NBI heating is not optimal. High densities also is a problem for NBI because deposition occurs before beam reaches axis. The third possible candidate is ion-cyclotron heating (ICH), successfully applied in some tokamaks and stellarators [1–3]. Another method, a proposed Alfvén wave heating, is based on exciting resonances in the plasma at even lower frequencies than the IC range.

Excitation of a plasma in the low-frequency ion-cyclotron and Alfvén domains results in oscillations with wavelengths comparable to the size of the plasma. The traditional ray-tracing methods applied for ECH frequencies (at least three orders of magnitude higher) can usually not be used for ICRH studies. Plasma geometry has a very important effect on the electromagnetic (E/M) wave propagation at large wavelengths, so a global numerical solution of a full 3D problem is required for a realistic stellarator geometry.

Apart from the heating purposes, the knowledge about low-frequency plasma oscillations can be used for diagnostics of the important parameters such as plasma density and rotational transform profile (the so-called magnetohydrodynamic spectroscopy), as it is done, for example, on the JET tokamak [4]. Another source of considerable interest for the low-frequency plasma spectrum is explained by a possible destabilisation of shear Alfvén waves [5–7] and global Alfvén modes [8] by the ions from the NBI, from ICRH heating systems or by the fusion born α -particles. Instabilities driven by fast ions can result in rapid losses of fusion α -particles whose confinement is crucial for the performance of future reactors. The destabilisation of global Alfvén modes has been experimentally observed on most large tokamaks (DIII-D, TFTR, JET, JT-60U) and on the W7-AS stellarator (see Ref. [9] and references therein). The importance of a good understanding of the low-frequency spectrum explains the interest of these studies for stellarators [5, 6, 10–12].

In this work, we will present a new code for the E/M wave propagation based on a global solution of the wave equation. The code solves the linearised set of Maxwell’s equations in a fully 3D stellarator geometry, taking into account all the geometrical effects of the finite plasma size and the interaction between the incident and the reflected waves. The wave-particle interaction is described by a relatively simple cold plasma model, that, however, retains the finite electron inertia and, therefore, mode conversion effects. We will show some results of calculations performed with the newly developed code in the Alfvén and IC frequency ranges, discuss the effect of geometry on the oscillation spectrum and validate the applicability of the code in 3D configurations.

There exist many 2D codes solving the global wave propagation problem in tokamaks in different plasma models. The list includes, but is not limited to, LION [13], NOVA-K [14],

PENN [15], TORIC [16], CASTOR-K [17], KIN-2D [18]. 3D configurations pose a major problem for the numerical application due to the complexity of the geometry and the resulting very large size of the problem, and the number of available tools is much smaller. There exist several full-wave codes calculating E/M waves in 3D geometry excited by an external antenna using different plasma models and different numerical methods. The AORSA3D project [19, 20] implements a kinetic plasma model with all-orders expansion in Larmor radius, solves the wave equation in terms of fields on a Cartesian grid and uses 3D Fourier series for the field representation. The size of the resulting numerical problem is huge, so the code runs on high-performance massively parallel computers. A 3D extension of the TASK/WM code [21] also uses field formulation of the wave equation and discretises the problem with Fourier expansions in the poloidal and toroidal angles and finite differences radially. Similarly, the STELION code [22] utilises a spectral approach for the perturbed electric field representation in the angular variables in non-orthogonal flux coordinates and finite differences in the radial direction.

Full 3D solutions require very intensive and numerically expensive calculations. The aim of the present work is to develop a smaller-scale full-wave code that, on the one hand, would run using much more modest computational resources, providing a solution on the timescale of minutes or, at most, hours; and, on the other hand, that could serve as a solid base for future extensions of the plasma model and coupling to other codes (for example, to the 3D particle drift orbit code VENUS that uses a similar formulation for the equilibrium and perturbed fields [23]).

Chapter 2

Physical model

In the present work, we will be calculating electromagnetic fields in magnetically confined plasmas. These fields are a result of a complicated superposition of many different sources — quasi-stationary fields from the external coil currents confining the plasma, fields generated by the currents in the plasma itself, either as a response to the confining magnetic field or otherwise driven currents, fields from the heating antennae etc. The general approach to simplify this problem consists of decomposing it into two major steps. First, static or slowly varying fields are considered. The steady state of the plasma is determined by the balance between the plasma pressure and the forces due to these fields. This defines the plasma equilibrium, which is a zero-order (in time series) solution of the magnetohydrodynamic (MHD) equations. The equilibrium contains the information about the geometry of the magnetic field, plasma shape and properties like density and temperature. This serves as a basis for the higher-order calculations, like the wave-propagation problem.

The fields of a wave propagating in plasma are calculated as a perturbation of the equilibrium state, as a second step of the problem. Decomposing the variables into a steady-state part and a small fast oscillating part simplifies the equations and allows for simple linearisation. This method is valid for small amplitude perturbations, when the background equilibrium can be considered not to be affected by these oscillations and the non-linear effects are small.

In this chapter, we will first briefly introduce a 3D toroidal stellarator equilibrium and the associated coordinate system used for perturbation calculations. Then, we will derive the main equation governing small-amplitude oscillations, which is the core of the numerical code presented here. We will also describe the plasma-wave interaction model implemented in the code, its underlying physics and limitations. In the last section of this chapter we will discuss the wave propagation in a uniform plasma and the most important types of solutions possible in the plasma model chosen.

2.1 Plasma equilibrium

An equilibrium in a magnetised plasma is a result of the balance between the plasma pressure and the forces from the magnetic fields and currents in the plasma. In the ideal MHD model, this balance is a solution to a static equation relating the current in the plasma and the pressure gradient,

$$\vec{j} \times \vec{B}_0 = \nabla p, \quad (2.1)$$

combined with Gauss' and Ampere's laws,

$$\nabla \cdot \vec{B}_0 = 0, \quad (2.2)$$

$$\nabla \times \vec{B}_0 = \mu_0 \vec{j}, \quad (2.3)$$

where \vec{j} is the plasma current, \vec{B}_0 is the equilibrium magnetic field and p is the plasma pressure. We consider the solutions with a single magnetic axis and nested magnetic surfaces. It is obvious from these equations that the plasma pressure gradient is perpendicular to the magnetic field, so that the pressure does not change along the field line and the magnetic surface is also a surface of constant pressure. Similarly, there is no current across the magnetic surface. If we assign a value s , called a flux label, to each magnetic surface, it then follows:

$$\vec{B}_0 \cdot \nabla s = 0. \quad (2.4)$$

s serves as a radial coordinate and is usually chosen to vary between 0 on the magnetic axis and 1 on the boundary of the plasma.

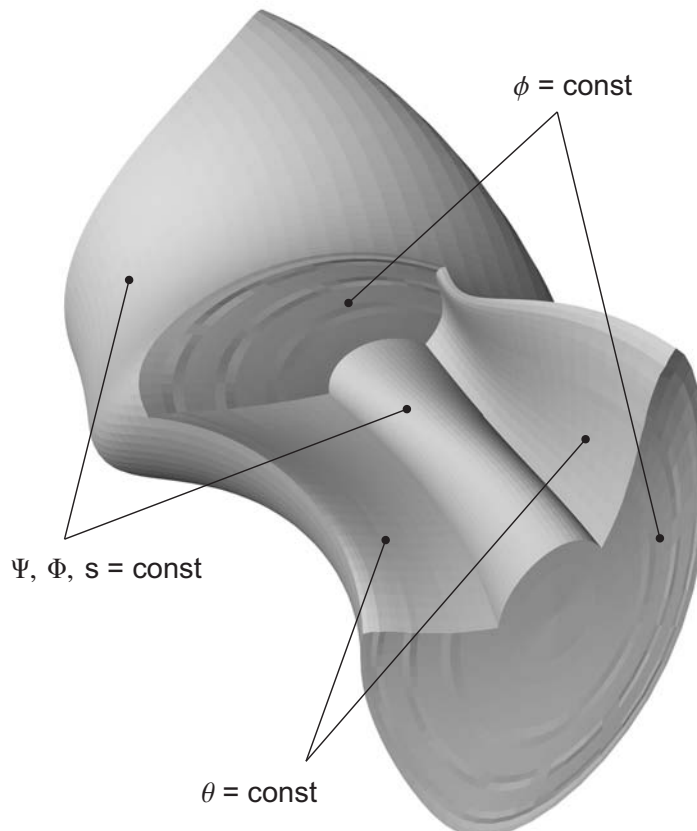


Figure 2.1. *An example of a 3D stellarator geometry (one of the 10 toroidal periods of the LHD device), surfaces of constant coordinates (s, θ, ϕ) .*

While the choice of a flux label as one of the coordinates seems rather obvious in a general 3D toroidal geometry, it is not so evident for the two remaining coordinates. There exist many possibilities, one being simply the geometrical angles. However, such a choice is not optimal. In the next section, we will introduce another type of coordinate frame, the flux coordinates [24].

2.2 Coordinate system

As follows from the equation (2.4), the magnetic field is everywhere perpendicular to the ∇s , and in this case \vec{B}_0 can be expressed in the Clebsch representation as a vector product of two gradients:

$$\vec{B}_0 = \nabla\psi \times \nabla\alpha, \quad (2.5)$$

where ψ is a function of s only, and α is a scalar function of all three variables (s, θ, ϕ) given by

$$\alpha(s, \theta, \phi) = a(s)(\theta + \lambda(s, \theta, \phi)) - \phi, \quad (2.6)$$

with $\lambda(s, \theta, \phi)$ — scalar periodic in θ and ϕ function. Here and in what follows, θ and ϕ are *not* geometrical angles, but some coordinates in the "poloidal" and "toroidal" directions. After expansion of the equation (2.5), we obtain

$$\vec{B}_0 = \nabla\psi \times \nabla(a\theta - \phi) + \nabla\psi \times \nabla(a\lambda),$$

or, taking advantage of the fact that ψ and a depend only on s ,

$$\vec{B}_0 = \nabla\phi \times \nabla\psi + a\nabla\psi \times \nabla\theta + \nabla\psi \times \nabla(a\lambda).$$

This expression describes the magnetic field in a general toroidal geometry with flux surfaces, using a very general set of coordinates (s, θ, ϕ) . The actual choice of coordinates and the corresponding representation of \vec{B}_0 depends on the problem at hand and has to be made by imposing some restrictions on the variables. We will now introduce the coordinate frame used in the present work, the Boozer magnetic coordinates [25–28]. Originally, they have been derived for the guiding center drift equations, separating the fast streaming of particles along the field lines from the slow perpendicular drift, but are now used in a wider range of applications.

A certain liberty in choosing the poloidal angle coordinate θ allows us to add to it an arbitrary periodic function $\tilde{\theta}$:

$$\theta' = \theta + \tilde{\theta}(s, \theta, \phi).$$

The new resulting coordinate will still satisfy the requirements for the function α . It means that the poloidal variable θ can be chosen to eliminate the function $\lambda(s, \theta, \phi)$ in the equation (2.6). This restricts the choice of the poloidal coordinate and results in a simpler expression for the magnetic field:

$$\vec{B}_0 = \nabla\phi \times \nabla\psi + a\nabla\psi \times \nabla\theta. \quad (2.7)$$

It can be easily verified that the functions $\nabla\psi$ and $a\nabla\psi$ have a simple physical meaning. A poloidal flux of the magnetic field on a surface labelled s is defined as a flux through a surface σ_P stretched between the magnetic axis and a contour of constant θ on the surface s ,

$$\Psi_P(s) = \int_{\sigma_P(s)} \vec{d}\sigma \cdot \vec{B}_0.$$

Substituting (2.7) and replacing $\vec{d}\sigma$ by its contravariant representation, we have

$$\Psi_P(s) = \int_{\sigma_P(s)} ds d\phi \sqrt{g} \nabla\theta \cdot \nabla\phi \times \nabla s \frac{d\psi}{ds},$$

where $\sqrt{g} = (\nabla s \times \nabla\theta \cdot \nabla\phi)^{-1}$ is the transformation jacobian. Therefore,

$$\Psi_P(s) = \int_0^{2\pi} d\phi \int_0^s ds' \frac{d\psi(s')}{ds'} = 2\pi\psi(s). \quad (2.8)$$

So, ψ appearing in the expression (2.7) is a measure of the poloidal magnetic flux and is called a flux function.

Analogously, the toroidal magnetic flux is defined as a flux through a surface crossing the magnetic axis and stretched on a contour of constant ϕ on the surface s .

$$\Psi_T(s) = \int_{\sigma_T(s)} \vec{d}\sigma \cdot \vec{B}_0.$$

In much the same way, we expand this relation:

$$\Psi_T(s) = \int_{\sigma_T(s)} ds d\theta \sqrt{g} \nabla\phi \cdot \nabla s \times \nabla\theta a(s) \frac{d\psi}{ds} = 2\pi \int_0^s ds' a(s') \frac{d\psi(s')}{ds'}. \quad (2.9)$$

A comparison between (2.8) and (2.9) gives a physical meaning to the function $a(s)$: $a(s) = d\Psi_T(s)/d\Psi_P(s) \equiv 1/\iota(s)$, the inverse of the rotational transform. In tokamaks, it is referred to as the safety factor q . So, the expression for the magnetic field in flux coordinates finally takes form

$$\vec{B}_0 = \nabla\phi \times \nabla\psi + \nabla\Phi \times \nabla\theta, \quad (2.10)$$

where $\Phi(s) = \Psi_T(s)/(2\pi)$ is the toroidal flux function.

It should be mentioned that in flux coordinates the magnetic field lines are straight. Indeed, the local pitch ι is defined by the ratio $d\theta/d\phi$, where the increments are taken along the field line:

$$\left. \frac{d\theta}{d\phi} \right|_{\vec{B}_0} = \frac{\vec{B}_0 \cdot \nabla\theta}{\vec{B}_0 \cdot \nabla\phi} = \frac{d\psi \nabla\phi \times \nabla s \cdot \nabla\theta}{d\Phi \nabla s \times \nabla\theta \cdot \nabla\phi} = \frac{1}{q(s)} \equiv \iota(s).$$

This value does not vary on the magnetic surface, therefore the field lines are indeed straight for the representation (2.10). It is an important property of the coordinate system, and it helps to simplify some relations. For example, $\vec{B}_0 \cdot \nabla$ operator plays an important role in the Alfvén wave dispersion relation, and such a choice of the coordinate system helps to perform the calculations.

Flux coordinates are not unique and at this point our coordinate system is not yet completely defined. We chose the poloidal variable θ in such a way that allows for the flux form (2.10) for the magnetic field representation, but the toroidal coordinate still leaves us one degree of freedom. This liberty can be used to obtain some additional desired properties of the coordinate system. Again, there exist many choices. For example, Hamada coordinates [29] use this freedom to make the jacobian constant on a magnetic surface. This has some advantages, but we chose to use Boozer coordinates [28] in which the toroidal and poloidal covariant components of the magnetic field are flux functions.

Without going into further details, we give the final expressions for the magnetic field in this system:

$$\begin{aligned}
\vec{B}_0 &= \nabla\phi \times \nabla\psi(s) + \nabla\Phi(s) \times \nabla\theta, \quad (\text{contravariant}) \\
\vec{B}_0 &= B_s \nabla s + J(s) \nabla\theta - I(s) \nabla\phi, \quad (\text{covariant}) \\
B_0^2 &= (\psi' J - \Phi' I) / \sqrt{g},
\end{aligned} \tag{2.11}$$

where $J(s)$ and $I(s)$ stand for the toroidal and poloidal current fluxes correspondingly.

In this work, we define the radial variable s as a normalised toroidal magnetic flux $s = \Phi(s)/\Phi_{edge}$, i.e. in the same way as it is defined in the equilibrium codes used here. With this choice, it scales approximately as the enclosed volume near the magnetic axis, so the jacobian of the transformation is not zero on the axis. More information about flux coordinates can be found in the review [30].

2.3 Equilibrium calculations

Wave propagation, as well as many other processes like transport, instabilities and turbulence, is a deviation from a static or slowly evolving MHD equilibrium state. Therefore, plasma equilibrium is a basis for any confinement study.

The MHD equilibrium equations (2.1)–(2.3) can be resolved analytically in 1D geometry, and, in some cases, in 2D axisymmetric toroidal configurations [31]. A solution to a general 3D stellarator equilibrium, however, can only be found numerically.

Numerous codes exist for equilibrium calculations. The non-linear nature of the equations arising from (2.1)–(2.3) requires iterative methods in most cases. We will briefly explain the procedure we follow here to obtain the underlying equilibrium, but a detailed study of equilibrium calculations is beyond the scope of this thesis.

The equilibrium solution is obtained in two steps. First, we use an ideal MHD 3D code VMEC (**V**ariational **M**oment **E**quilibrium **C**ode) [32–36] which is a standard tool for the

stellarator geometry. The code is based on minimising the plasma energy integral

$$W = \int \left(\frac{B_0^2}{2\mu_0} + \frac{p}{\gamma - 1} \right) dV,$$

where γ is the adiabatic index. During the variation of W , the flux coordinates are treated as independent variables, whereas the real space coordinates \vec{r} are considered to be dependent. The cylindrical coordinate system (R, ϕ, Z) is used for projections, where R is the major radius, ϕ is the geometrical toroidal angle and Z is the height above the midplane. (R, ϕ, Z) are decomposed into finite Fourier series using independent VMEC coordinates (s, u, v) :

$$\begin{aligned} R(s, u, v) &= \sum_{m,n} R_{mn}(s) \cos(mu - nNv), \\ \phi &= v, \\ Z(s, u, v) &= \sum_{m,n} Z_{mn}(s) \sin(mu - nNv), \end{aligned} \tag{2.12}$$

where N is the number of toroidal periods of the configuration. The radial label s is proportional to the toroidal magnetic flux enclosed ($0 \leq s \leq 1$). While the toroidal VMEC variable v is simply equal to the geometrical toroidal angle, the choice of poloidal variable u is based on the desired convergence properties of the code. In VMEC, the role of u is to minimise the number of modes in the expansion (2.12) and to accelerate the convergence of the Fourier series. As pointed out in [32], this requirement for the poloidal variable is, in general, incompatible with the straight field line coordinates.

Once the initial numerical equilibrium is obtained with VMEC, it is used as an input to the TERPSICHORE code. TERPSICHORE is a 3D global ideal MHD stability code [37–40], but we only use a part of it that does the mapping of the VMEC equilibrium to the Boozer coordinates (2.11). TERPSICHORE recalculates the equilibrium using the same radial variable s and the new angles θ and ϕ that are different from the VMEC variables u and v . The magnetic field, current and magnetic fluxes and the metric elements of the Boozer coordinate frame are obtained on an equidistant in (s, θ, ϕ) 3D grid to be later used to calculate the coefficients of the wave equation.

2.4 Wave equations

Now that we have described the geometry of the equilibrium state of the plasma, the second step to the field calculations can be addressed. The pure stationary state of the plasma described above does not exist in a real experiment. It can either be unstable and develop instabilities that change or even completely destroy the equilibrium, or even in a stable configuration it can both evolve slowly with time and be subject to numerous faster fluctuations. Some of these fluctuations are undesirable and can be a nuisance in a fusion device, but some are useful and can serve for example for diagnostics of the plasma parameters or for the plasma heating needs. To predict the plasma response to these oscillations, we have to be able to calculate the perturbed fields in plasma, i.e. the wave propagation.

The general approach to the wave propagation problem is to solve a set of linearised Maxwell's equations in the plasma. All fields are expressed as a sum of a static or a slowly evolving part (equilibrium) and a small fast oscillating part (perturbation). In the present work, we solve the linear problem. This means that all quadratic and higher orders of the perturbation terms are neglected, which is justified for small-amplitude oscillations.

In a real experiment, waves in a plasma can be excited by a number of ways. The plasma itself is a source of various perturbations, but a description of these effects requires taking into account finite temperature effects. Here, we use a simpler wave-plasma interaction model that does not include energy exchanges between the plasma and the propagating wave apart from some artificial absorption that we will discuss later. Another source for the perturbations can be an antenna. In the present work, we consider waves launched into the plasma by stationary oscillating currents in an external antenna, either for heating or for active diagnostic purposes.

There are two major approaches to resolve the propagation problem. The first one is based on the assumption that the characteristic variation time and length scales of the plasma are much larger than that of the wave in question (the classical Wentzel-Kramers-Brillouin (WKB) approximation). In this approach, the wave launched in the

plasma is assumed to propagate along a ray trajectory that can be calculated from the ray equations of geometrical optics using the local dispersion relation. The methods working in this approximation are usually called *ray-tracing*, or *eikonal* methods [41].

Whereas the first condition (time scale relation) is usually easily satisfied for static or slowly evolving plasmas, the second one strongly depends on the wave frequency range. For the typical fusion device parameters, the plasma can be considered homogeneous over one wavelength for the oscillations in high frequency range, GHz and higher. This is the reason why ray-tracing methods are usually applied to the electron-cyclotron heating schemes.

In the low frequency domain, such as the ion-cyclotron (IC) and Alfvén range of frequencies (kHz – MHz), the wavelength becomes comparable or even larger than the characteristic length scale of the plasma. Therefore, the inhomogeneity of the medium over a wavelength cannot be neglected and the WKB approximation is no longer applicable. At these frequencies, a *global* solution is required, which takes into account the finite spatial extent of the plasma, all the effects of absorption of the incident wave, reflection from the walls, etc. The methods based on a global solution of the set of Maxwell’s equations in the inhomogeneous plasma together with the boundary conditions are also called a *full-wave* approach to the propagation problem. A global solution, in principle, is not limited to low frequencies only. However, it is hard to apply this method for high frequencies because of the size of the numerical problem. The full-wave method should allow for at least several mesh points per wavelength, so with rising frequencies the resulting matrix size rapidly increases, making the global solution very expensive to solve. Thus, this approach is usually applied up to the IC range of frequencies.

To solve the global wave propagation problem, we start with the standard set of time-dependent Maxwell’s equations

$$\left\{ \begin{array}{ll} \nabla \times \vec{E} = -\frac{1}{c} \frac{\partial \vec{B}}{\partial t}, & \nabla \cdot \vec{D} = 4\pi\rho_{ant}, \\ \nabla \times \vec{B} = \frac{1}{c} \frac{\partial \vec{D}}{\partial t} + \frac{4\pi}{c} \vec{j}_{ant}, & \nabla \cdot \vec{B} = 0, \\ & \vec{D} = \vec{E} + \frac{4\pi\omega}{c} \vec{j} \equiv \hat{\epsilon} \cdot \vec{E}, \end{array} \right. \quad (2.13)$$

where \vec{j}_{ant} is the imposed current distribution in the antenna. ρ_{ant} is the antenna volume charge density which is zero for a divergence-free antenna but is kept here for generality. The equations are valid both in plasma and in vacuum, the only difference being the value of the dielectric tensor $\hat{\epsilon}$. The $\hat{\epsilon}$ value in the vacuum is obviously unity, its value in the plasma depends on the plasma model chosen and is discussed in the next section. This description is very convenient since it allows for exactly the same treatment of the plasma and vacuum regions by simply substituting the correct value of $\hat{\epsilon}$ in each point of space.

For an antenna current excitation that is periodic in time, the most natural way to solve Maxwell's equations (2.13) is to Fourier-transform all the time-dependent functions and look for the solutions as harmonic oscillations with complex amplitude:

$$F(\vec{r}, t) = \hat{F}(\vec{r})e^{-i\omega t}. \quad (2.14)$$

As usual, only the real part of $F(\vec{r}, t)$ corresponds to a physical value, the imaginary part contains the information about the phase. Substituting the fields and currents in Eq.(2.13) with (2.14) and defining a vacuum wave vector $k_0 = \omega/c$ we have the time-independent equations for complex amplitudes:

$$\left\{ \begin{array}{l} \nabla \times \vec{E} = ik_0 \vec{B}, \\ \nabla \times \vec{B} = -ik_0 \hat{\epsilon} \cdot \vec{E} + \frac{4\pi}{c} \vec{j}_{ant}, \\ \nabla \cdot (\hat{\epsilon} \cdot \vec{E}) = 4\pi \rho_{ant}, \\ \nabla \cdot \vec{B} = 0, \end{array} \right. \quad (2.15)$$

where fields and currents have only spatial dependence (here and henceforth, we omit the " ^ " symbol from field variables, for ease of notation.). A combination of equations (2.15) yields the wave equation in a classical form in terms of the electric field, i.e. a *field formulation*:

$$\nabla \times \nabla \times \vec{E} - k_0^2 \hat{\epsilon} \cdot \vec{E} = ik_0 \frac{4\pi}{c} \vec{j}_{ant}. \quad (2.16)$$

A solution of this equation together with the appropriate boundary conditions can give a distribution of the wave fields in the plasma. However, this is not the form of the wave equation we use here. It has been shown that a discretisation of the equation (2.16) applying standard finite element method introduces spurious unphysical solutions that are very hard to "filter" from the approximation to the true physical solution, sometimes even at an arbitrarily fine mesh [15, 42–46]. This effect of the so called *numerical pollution*, discussed in more detail in the Appendix, is well known and has been addressed in many studies. Various methods to fight these unphysical solutions have been proposed: finite hybrid elements [47], penalty method [48], discrete singular convolution [49], etc. We have implemented here a scheme that uses finite elements in one direction, but is pollution-free due to the choice of the equation formulation. A similar method has already been successfully applied for the wave propagation problem in toroidal axisymmetric systems [15, 50].

This approach consists of reformulating the equation (2.16) by introducing the electromagnetic potentials $(\vec{A}, \tilde{\phi})$ (we will use "tilde" for the electrostatic potential to distinguish it from the toroidal angle). Any divergence-free field can be represented as a curl of a vector:

$$\vec{B} = \nabla \times \vec{A}. \quad (2.17)$$

Then, comparing this expression for \vec{B} with the first equation in (2.15), we obtain

$$\vec{E} = -\nabla \tilde{\phi} + ik_0 \vec{A}, \quad (2.18)$$

where $\tilde{\phi}$ is the electrostatic potential. As follows from the definition of the magnetic vector potential (2.17), a gradient of an arbitrary function can be added to \vec{A} without changing the value of \vec{B} . It means that \vec{A} can always be redefined to satisfy the Coulomb gauge condition:

$$\nabla \cdot \vec{A} = 0. \quad (2.19)$$

Maxwell's equations (2.15) rewritten in terms of potentials are:

$$\begin{aligned} \nabla \times \vec{B} &= ik_0 \hat{\epsilon} \cdot \nabla \tilde{\phi} + k_0^2 \hat{\epsilon} \cdot \vec{A} + \frac{4\pi}{c} \vec{j}_{ant} = \nabla \times \nabla \times \vec{A}, \\ \nabla \cdot (\hat{\epsilon} \cdot \vec{E}) &= -\nabla \cdot (\hat{\epsilon} \cdot \nabla \tilde{\phi}) + ik_0 \nabla \cdot (\hat{\epsilon} \cdot \vec{A}) = 4\pi \rho_{ant}. \end{aligned} \quad (2.20)$$

Combining this with the Coulomb gauge (2.19), we finally obtain the wave equation in a *potential formulation*:

$$\begin{cases} \nabla^2 \vec{A} + k_0^2 \hat{\epsilon} \cdot \vec{A} + ik_0 \hat{\epsilon} \cdot \nabla \tilde{\phi} = -\frac{4\pi}{c} \vec{j}_{ant}, \\ \nabla \cdot (\hat{\epsilon} \cdot \nabla \tilde{\phi}) - ik_0 \nabla \cdot (\hat{\epsilon} \cdot \vec{A}) = -4\pi \rho_{ant}. \end{cases} \quad (2.21)$$

It can be easily verified that the gauge condition follows from the equations (2.21) provided the currents in the right-hand side satisfy the charge continuity equation $-i\omega\rho_{ant} + \nabla \cdot \vec{j}_{ant} = 0$. Indeed, a combination of the divergence of the first equation with the second one yields the Laplace equation for $\nabla \cdot \vec{A}$: $\nabla^2(\nabla \cdot \vec{A}) = 0$. So, if the Coulomb gauge is imposed on the boundary, it will be automatically satisfied everywhere inside the calculation domain. In practice, the numerical solution is never **exactly** divergence-free and this discrepancy can be a good measure of the self-consistence and the convergence of the results. More details about the role of the gauge can be found in the section 11 of chapter 3.

Now that we have established the wave equations to be solved, we have to define the dielectric tensor $\hat{\epsilon}$ in plasma, that is to choose the wave-plasma interaction model.

2.5 Cold plasma approximation

Wave interaction with plasma is a very complex process. Depending on the prospective domain of application, different approximation models have to be chosen, always a trade-off between the simplicity of the numerical implementation and the accuracy of the physical description. The model that was used for the equilibrium calculations in section 2.1 represents the plasma as a single ideally conducting fluid. This model ignores the separate identities of the ions and electrons. It does not describe the plasma as an ensemble of moving particles, but only operates with average quantities in velocity space, such as pressure, mass density, flow velocity. It means that the phenomena that can be handled by this model are limited to low frequencies, when the oscillations are much slower than the characteristic frequencies of particle motion effects like the cyclotron rotation around

the magnetic field lines. While totally sufficient for the equilibrium description for our purposes, the MHD model is not applicable to the wave propagation problem considered here since we are interested not only in the very low frequencies, but also in the ICF range.

In this thesis, we use a *cold plasma model* for the wave-plasma interaction description. It is a relatively simple model, allowing for an easy numerical application, but still retaining the aspects of the plasma dynamics important to us. This model presumes a collisionless plasma without a thermal motion of the particles. Any small fluctuation from the unperturbed state induces an electric field and, according to Maxwell's equations, a perturbed component of the magnetic field, that, in turn, affects the motion of particles. This motion, again, generates perturbed fields, that have to be consistent with the original fluctuation. This process can be expressed in an easy mathematical form. Despite being simple, this model can describe quite many phenomena in the plasma, retains important resonances and in many cases can be unexpectedly close to the experiment. Let us briefly repeat the classical formulation of the cold plasma model [41] with a minor modification.

In order to be able to solve the wave equation in a plasma, we need to know the reaction of the plasma to the applied fields. This reaction can be expressed through the dielectric tensor, so we need to calculate $\hat{\epsilon}$. By definition,

$$\hat{\epsilon} \cdot \vec{E} \equiv \vec{E} + \frac{4\pi i}{\omega} \vec{j}, \quad (2.22)$$

where \vec{j} is the plasma current. This current can be calculated in terms of the plasma particle velocities as the total charge carried by the particles per time unit:

$$\vec{j} = \sum_k n_k Z_k e \vec{v}_k, \quad (2.23)$$

where n_k is the number of particles k per unit volume, Z_k is the charge of the species k (positive for ions and negative for electrons), e is the elementary charge and \vec{v}_k is the particle macroscopic velocity.

The particles have no thermal motion at all and in the classical cold plasma model

are only subject to the forces due to \vec{E} and \vec{B} :

$$m_k \frac{d\vec{v}_k}{dt} = Z_k e \left(\vec{E} + \frac{\vec{v}_k}{c} \times \vec{B} \right). \quad (2.24)$$

As it can be seen from this equation, this model has no losses and the energy of the system wave-particle is conserved. The solution of this system, as it will be clear a bit further, can give rise to singularities in the dielectric tensor coefficients. These singularities, although not physical, obviously complicate the implementation of a numerical application. A possible way to work around this problem based on a viable physical argument behind it is to add a "friction" to this model. Indeed, the singularities are avoided if an ad hoc friction force is added to the equation (2.24):

$$m_k \frac{d\vec{v}_k}{dt} = Z_k e \left(\vec{E} + \frac{\vec{v}_k}{c} \times \vec{B} \right) - \nu_k m_k \vec{v}_k. \quad (2.25)$$

ν_k here is an artificial parameter that in some sense can be considered as a "collision frequency". We will see later that this parameter helps to resolve numerically the wave problem, but fortunately does not have a dramatic influence on the results.

Since a stationary-state problem is considered, all perturbed quantities behave as $e^{-i\omega t}$ and the time derivative becomes simply a multiplication by $-i\omega$. We neglect the second order term in the Lorentz force, so only the equilibrium component \vec{B}_0 of the magnetic field remains and the linearised equation takes the form

$$-i\omega m_k \vec{v}_k = Z_k e \left(\vec{E} + \frac{\vec{v}_k}{c} \times \vec{B}_0 \right) - \nu_k m_k \vec{v}_k. \quad (2.26)$$

To obtain the expression for the dielectric tensor, the particle velocities \vec{v}_k have to be calculated as functions of the perturbed electric field. Without loss of generality, we choose a local orthogonal coordinate system such that the z axis is directed along \vec{B}_0 . Projecting the equation (2.26), we have:

$$\begin{cases} -i\omega m_k v_{kx} = Z_k e \left(E_x + \frac{1}{c} v_{ky} B_0 \right) - \nu_k m_k v_{kx}, \\ -i\omega m_k v_{ky} = Z_k e \left(E_y - \frac{1}{c} v_{kx} B_0 \right) - \nu_k m_k v_{ky}, \\ -i\omega m_k v_{kz} = Z_k e E_z - \nu_k m_k v_{kz}. \end{cases} \quad (2.27)$$

We denote $\omega_k^* = \omega + i\nu_k = \omega(1 + i\nu_k^0)$ and solve this system for \vec{v}_k components:

$$\begin{aligned} v_{kx} &= \frac{1}{1 - \Omega_k^2/\omega_k^{*2}} \frac{iZ_k e}{m_k \omega_k^*} \left(E_x + i \frac{\Omega_k}{\omega_k^*} E_y \right), \\ v_{ky} &= \frac{1}{1 - \Omega_k^2/\omega_k^{*2}} \frac{iZ_k e}{m_k \omega_k^*} \left(E_y - i \frac{\Omega_k}{\omega_k^*} E_x \right), \\ v_{kz} &= \frac{iZ_k e}{m_k \omega_k^*} E_z. \end{aligned} \quad (2.28)$$

Substituting these relations in the expression for the plasma current and then into the definition of $\hat{\epsilon}$ (2.22), the (almost) classical expression for the local value of the dielectric tensor is obtained:

$$\hat{\epsilon} = \begin{pmatrix} S & -iD & 0 \\ iD & S & 0 \\ 0 & 0 & P \end{pmatrix}, \quad \begin{aligned} S &= 1 - \sum_k \frac{\Pi_k^2}{\omega/\omega_k^* (\omega_k^{*2} - \Omega_k^2)}, \\ D &= \sum_k \frac{\Omega_k}{\omega} \frac{\Pi_k^2}{\omega_k^{*2} - \Omega_k^2}, \\ P &= 1 - \sum_k \frac{\Pi_k^2}{\omega \omega_k^*}, \end{aligned} \quad (2.29)$$

where $\Pi_k^2 = 4\pi n_k Z_k^2 e^2 / m_k$ and $\Omega_k = Z_k e B_0 / m_k c$ are the plasma and cyclotron frequencies for the species k . As noted before, the introduction of an imaginary part in the frequency ω_k^* removes the singularity in the $\hat{\epsilon}$ components S and D at the gyrofrequency of the particle species. This imaginary part plays a role of "resistivity" in an otherwise dissipation-free cold plasma model.

The model is fairly simple, but it retains the inertial effects of not only ions, but also electrons. Inclusion of a finite electron mass and, therefore, of a parallel component of the perturbed electric field allows for the description of mode conversion effects, only possible with a non-zero electron inertia. As opposed to a simpler model with no parallel electric field, the singularity in the wavefields at the Alfvén resonance positions is resolved by a conversion to a short wavelength oscillations.

The cold plasma model is derived neglecting the temperature effects. Therefore, its applicability is limited to a situation when the thermal speed of the particles is small compared to the wave phase velocity so that there is no resonant interaction between the propagating wave and the plasma particles. This approximation breaks down at a

resonance, where the wave vector, by definition, goes to infinity and the wave phase velocity approaches zero. More sophisticated models that take into account finite thermal and Larmor radius effects have to be used then. The dielectric tensor then takes a much more complicated form. In this *hot* (or *kinetic*) *plasma model*, it is no longer an algebraic multiplication matrix, but a differential operator, and its values are defined non-locally. Coupled with a general 3D geometry, this problem would become really hard to resolve. The hot plasma model is beyond the scope of this thesis, a more detailed description of the kinetic dielectric tensor can be found, for example, in the excellent review paper [51].

2.6 Waves in cold plasma

Before attacking the full wave problem, it is very useful to analyse first the solutions of the wave equation in an unbounded homogeneous plasma, without considering the effects of geometry. This analysis can give a qualitative idea of the possible oscillation spectrum in a plasma in the frame of the physical model selected, that, moreover, can be very close to the full global solution in finite plasmas in case of short wavelengths.

In a homogeneous medium, the solution of the linear equation (2.16) can be found as a superposition of plane waves:

$$\vec{E}(\vec{r}, t) = \hat{E} e^{\vec{k} \cdot \vec{r} - i\omega t}. \quad (2.30)$$

The homogeneous counterpart of the differential equation (2.16) is then rewritten as a simple algebraic equation

$$\vec{k} \times (\vec{k} \times \vec{E}) + \frac{\omega^2}{c^2} \hat{\epsilon} \cdot \vec{E} = 0. \quad (2.31)$$

(again, we omit the " ^ " symbol from the amplitudes for clarity.)

The usual choice is to replace \vec{k} with the vector $\vec{n} = \vec{k}c/\omega$, whose direction is the same as that of \vec{k} and the magnitude is equal to the refractive index. Now, again, without loss of generality, we direct the z axis of the coordinate system along the equilibrium magnetic field \vec{B}_0 and choose x such that \vec{n} lies in the xz plane.

Decomposing \vec{n} into the parallel and the perpendicular to \vec{B}_0 components n_{\parallel} , n_{\perp} , the equation (2.31) is then obtained in the well known matrix form:

$$\begin{pmatrix} S - n_{\parallel}^2 & -iD & n_{\parallel}n_{\perp} \\ iD & S - n^2 & 0 \\ n_{\parallel}n_{\perp} & 0 & P - n_{\perp}^2 \end{pmatrix} \begin{pmatrix} E_x \\ E_y \\ E_z \end{pmatrix} = 0. \quad (2.32)$$

A non-trivial solution of this equation can exist only if the determinant of the matrix is zero, which results in the equation relating the components of \vec{n} and, through the coefficients S , D and P , ω :

$$D^2 (n_{\perp}^2 - P) + (n_{\perp}^2 + n_{\parallel}^2 - S) (n_{\parallel}^2 P + (n_{\perp}^2 - P) S) = 0. \quad (2.33)$$

A general solution of this dispersion relation for ω is not possible, but it can be found in some important limits. Let us first consider waves at very low frequencies $\omega \ll \Omega_i, \Pi_i$ in a one-ion-species plasma. Retaining only the leading terms in m_e/m_i and ω/Ω_i ratios, we obtain the approximated expressions for S , D and P coefficients:

$$\begin{aligned} S &= 1 - \frac{\Pi_i^2}{\omega^2 - \Omega_i^2} - \frac{\Pi_e^2}{\omega^2 - \Omega_e^2} \approx \left(\frac{c}{c_A}\right)^2 \frac{1}{1 - (\omega/\Omega_i)^2}, \\ D &= \frac{\Omega_i}{\omega} \frac{\Pi_i^2}{\omega^2 - \Omega_i^2} - \frac{\Omega_e}{\omega} \frac{\Pi_e^2}{\omega^2 - \Omega_e^2} \approx \frac{\Omega_i}{\omega} \frac{\Pi_i^2}{\Omega_i^2} \left(-1 - \frac{\omega^2}{\Omega_i^2}\right) + \frac{\Omega_e}{\omega} \frac{\Pi_e^2}{\Omega_e^2} \left(1 + \frac{\omega^2}{\Omega_e^2}\right) \approx -\frac{\omega}{\Omega_i} \left(\frac{c}{c_A}\right)^2, \\ P &= 1 - \frac{\Pi_i^2}{\omega^2} - \frac{\Pi_e^2}{\omega^2} \approx -\frac{\Pi_e^2}{\omega^2}, \end{aligned}$$

where we replaced Π_i/Ω_i with c/c_A , $c_A = B_0/\sqrt{4\pi \sum n_k m_k}$ is the Alfvén speed (here, we also neglect the small imaginary part ν introduced in the previous section). Therefore, for low frequencies, the first term in Eq.(2.33) is negligible and the dispersion relation takes a particularly simple form:

$$(n_{\perp}^2 + n_{\parallel}^2 - S) (n_{\parallel}^2 P + (n_{\perp}^2 - P) S) = 0. \quad (2.34)$$

Nullifying the first bracket yields the solution for the *fast magnetosonic wave*, also called *fast*, or *compressional Alfvén wave*:

$$\omega^2 = c_A^2 k^2. \quad (2.35)$$

The second bracket defines the *slow*, or *shear Alfvén wave*:

$$\omega^2 = \frac{c_A^2 k_{\parallel}^2}{1 + \frac{k_{\perp}^2 c^2}{\Pi_e^2}}. \quad (2.36)$$

This wave has $B_{\parallel} = 0$ and usually propagates from the point of Alfvén resonance (discussed later) towards the plasma edge, so it is sometimes also called a *quasi-electrostatic surface wave*, or *quasi-electrostatic wave*. Note that this mode can only be obtained in the model retaining the finite electron mass. In the limit $m_e \rightarrow 0$ we recover the classical expression for the Alfvén wave known from the ideal MHD theory:

$$\omega^2 = c_A^2 k_{\parallel}^2. \quad (2.37)$$

The fast magnetosonic wave (2.35) and the slow (or shear) Alfvén wave (2.37) are the two fundamental modes present in the cold plasma model. The fast/slow terminology refers to the values of the phase velocity of the two waves. The compressional/shear notation classifies the waves according to the directions of the associated flows. The first wave has a non-zero component of the flow velocity in the direction of propagation and is therefore a compressional mode, whereas the second wave has a flow of zero divergence and so is a shear (or torsional) mode. Note that in the cold plasma model with zero plasma pressure the thing that resists the compression of the wave is not the plasma, but the magnetic field.

As ω approaches Ω_i , the solution for the two branches can be found in the approximation $m_e \rightarrow 0$ [51]:

$$\begin{aligned} \omega^2 &= c_A^2 k^2 \left(1 + \frac{k_{\parallel}^2}{k^2} \right), \\ \omega^2 &= \Omega_i^2 \left[1 - \left(\frac{\Pi_i^2}{k_{\parallel}^2 c} \right)^2 \left(1 + \frac{k_{\parallel}^2}{k^2} \right) \right]. \end{aligned} \quad (2.38)$$

The first branch, the fast wave, is similar to the low frequency expression (2.35) and is not much affected by the cyclotron resonance; it can propagate both below and above Ω_i . The Alfvén wave solution, on the other hand, is very different from the dispersion

relation (2.37). The frequency of this wave always remains below Ω_i . This wave at ω near Ω_i is sometimes called *ion cyclotron wave*. A more complete description of low frequency waves in plasma can be found in a very detailed review [51].

These solutions are valid for a uniform unbounded plasma, therefore they do not describe the global modes. In plasmas of finite spatial extent, the interaction between the incident and the reflected waves can result in global oscillations of the system. These oscillations strongly depend on the plasma geometry and can only be obtained by a full-wave approach. In the next chapter, we describe the numerical scheme used here to discretise the global wave equation.

Chapter 3

Numerical implementation

Resolution of the wave equations in a general three-dimensional geometry is impossible by analytical means. While analytical solutions are available for very simple geometries, a realistic stellarator configuration requires a numerical analysis. In the previous chapter, all the main equations describing the wave propagation and the plasma model have been laid down. This chapter deals essentially with the numerical formulation and the methods we used to discretise and resolve these equations.

First, we present the discretisation method applied to transform the continuous problem into a discrete set of algebraic equations. A finite element method combined with Fourier decomposition is introduced.

Then, we will discuss the coordinate system used for the vector projections. A scalar representation of the full-wave equation in a general 3D stellarator geometry is a challenge in itself even without a plasma. Expansion of the equation in terms of known quantities and projections to the coordinate system leads to a huge number of terms, all of which should be programmed in the code. A special effort has been made to ensure that all the terms are correctly represented. Some technical details of the numerical implementation and of the coding are presented in this chapter.

In a configuration of finite extent, the wave equations have to be coupled with the appropriate boundary conditions. In a geometry with a magnetic axis such as a stellarator with nested magnetic surfaces, the treatment of the axis region is an important issue as

well. Boundary, gauge conditions and unicity on the axis with some numerical results are discussed here, as well as the antenna design.

Finally, the numerical solution obtained has to be verified in many ways. The obvious checks to make are the energy conservation law and the numerical convergence. Different measures of convergence and the diagnostics implemented in the code are presented in the last part of this chapter.

We conclude the description of the numerical part with a brief discussion of the computational resources required for the code and their scaling with the size of the problem.

3.1 Discretisation and Finite Element Method

We are now going to discretise the wave equation in the potential formulation (2.21) derived in the previous chapter. To do so, we will use a Finite Element Method (FEM) in the radial direction combined with a Fourier decomposition in the two remaining variables.

The FEM is a numerical technique to obtain approximate solutions to a large variety of engineering problems expressed as algebraic, differential or integral equations [52]. When the geometry of the configuration studied is of complex shape that does not allow for analytical solutions, an approximate numerical solution to the problem can be found by dividing the calculation domain into small elements of regular shape. Decreasing the size of these "finite elements" (and, of course, increasing their number) the exact shape of the configuration can be approached. The development of the FEM is often attributed to Clough and coworkers in the 1960s in the aero-space industry, who applied it to analyse aircraft structures. Even though the use of the FEM was originally limited to solid state body mechanics problems, with the fast computer progress it rapidly expanded to many other applications and has become the defacto standard for solving problems in such fields as fluid mechanics, acoustics, heat transfer and many more. It has also been successfully applied and validated in plasma physics.

When discretised with finite elements, a continuous physical problem together with the boundary conditions is first transformed into a set of linear equations with unknown nodal

values. This is done by decomposing the sought function into a sum of basis interpolation functions with unknown coefficients. This linear system is represented by a large matrix that can be solved by standard numerical routines. The nodal values obtained and the interpolation functions for the elements completely define the behavior of the approximate solution within the elements. These values can then be used to recover the approximated solution everywhere inside the finite elements.

Since the number of finite elements N can be very large and the matrix size increases quadratically with the number of basis functions, the matrix problem in a general case could be expensive to solve. A very important property of the FEM is that for a specific choice of basis functions, namely when they are localised on a few finite elements only, the matrix becomes diagonally banded. This largely reduces the size of the problem.

Various approaches can be used to transform the continuous form of the problem into its finite element discrete analogue. If the physical formulation takes a form of a differential equation, as in our case, then the most popular method to apply is the Galerkin method.

The Galerkin method is based on construction and minimisation of a residual of the equation by multiplying its terms by test functions, integrating over the calculation domain and equating to zero. Applied to the equation (2.21), it results in the following integral form:

$$\left\{ \begin{array}{l} \int_{\Omega} dV \left[-(\nabla \times \vec{F}^*) \cdot (\nabla \times \vec{A}) - (\nabla \cdot \vec{F}^*)(\nabla \cdot \vec{A}) + k_0^2 \vec{F}^* \cdot (\hat{\epsilon} \cdot \vec{A}) + ik_0 \vec{F}^* \cdot (\hat{\epsilon} \cdot \nabla \tilde{\phi}) \right] \\ \quad + \int_{\delta\Omega} d\vec{S} \cdot \left[\vec{F}^* \times (\nabla \times \vec{A}) + \vec{F}^* (\nabla \cdot \vec{A}) \right] = -\frac{4\pi}{c} \int_{\Omega} dV \vec{F}^* \cdot \vec{j}_{ant} \\ \int_{\Omega} dV \left[\nabla G^* \cdot (\hat{\epsilon} \cdot \nabla \tilde{\phi}) - ik_0 \nabla G^* \cdot (\hat{\epsilon} \cdot \vec{A}) \right] + \int_{\delta\Omega} d\vec{S} \cdot \left[ik_0 G^* \hat{\epsilon} \cdot \vec{A} - G^* \hat{\epsilon} \cdot \nabla \tilde{\phi} \right] \\ \quad = -4\pi \int_{\Omega} dV G^* \rho_{ant}. \end{array} \right. \quad (3.1)$$

Here, \vec{F}^* and G^* are the complex conjugates of the test functions that are chosen from the same functional space as \vec{A} and $\tilde{\phi}$. To obtain the equation (3.1), an integration by parts of the terms with second-order derivatives ∇^2 and $\nabla \cdot (\hat{\epsilon} \cdot \nabla \tilde{\phi})$ has been done, so only the first-order partial derivatives of \vec{A} and $\tilde{\phi}$ remain. The integration in the plasma

is performed on the magnetic surfaces and in the vacuum — on the pseudo-surfaces.

We now have to choose a set of interpolating functions to discretise the equation (3.1) with. In the standard FEM, the 3D calculation domain is divided into a number of small 3D elements of regular topology. In the present work, we use a modified version of this method by combining the standard FEM with a Fourier decomposition. Instead of taking 3D elements, we only apply standard finite elements in one, radial, direction and use a spectral representation in the two remaining directions, the poloidal and toroidal angles. The numerical approximation to the unknown functions is then sought in the form

$$f(s, \theta, \phi) = \sum_{e,a,l_{mn}} f^{eal_{mn}} \psi_{ea}(s) e^{i(m\theta+n\phi)}, \quad (3.2)$$

where $\psi_{ea}(s)$ are the localised radial basis functions (e being the radial interval index, and a — the local index of the basis function on the element e , a takes values of 1 or 2 for the linear FE and 1, 2, 3 or 4 for the cubic FE, as will be shown later), θ and ϕ are Boozer angles, l_{mn} labels the Fourier harmonics (m, n) and, the last but not the least, $f^{eal_{mn}}$ are the unknown coefficients to be determined.

In some sense, this approach is equal to a standard 3D FEM on a grid with large hollow toroidal-shaped cells formed by two neighbouring magnetic surfaces with a set of interpolating functions localised radially and exponential ($e^{i(m\theta+n\phi)}$) in the toroidal and poloidal directions.

Such a representation of the solution can be particularly efficient for the Alfvén range of perturbation frequencies. It has been shown previously [53] that the location of the dispersion relation solution for Alfvén resonance coincides with magnetic surfaces, at least for axisymmetric configurations. This results in a rapid variation of the wavefields across the magnetic surfaces and relatively small gradients in the poloidal and toroidal directions. Such situation is the best case for the representation (3.2). While finite elements in the radial direction can easily describe rapid change of the solution, the number of Fourier modes in θ and ϕ required for the approximation can be relatively small, making the resulting matrix smaller.

While very advantageous in the Alfvén domain, this discretisation method can somewhat lose in efficiency for higher frequencies. In a tokamak configuration, for example, the ion cyclotron resonance can cross many surfaces, which results in a strong poloidal variation of the equation coefficients and makes it harder to represent the solution with Fourier harmonics. However, we could still converge the results for the ICRF scenario with a reasonable number of modes (25-50), as will be shown in chapter 4.

Another reason for the spectral decomposition is the simplicity of the k_{\parallel} calculation. The value of the parallel wave vector is not used directly for $\hat{\epsilon}$ calculation in the cold plasma model, but it is required for more sophisticated descriptions of the plasma. Unlike in a 1D cylindrical geometry where k_{\parallel} is simply an algebraic expression, in a 2D or a 3D geometry it becomes a differential operator:

$$ik_{\parallel} = \nabla_{\parallel} = \frac{1}{B_0} \vec{B}_0 \cdot \nabla = \frac{1}{B_0} \left(\vec{B}_0 \cdot \nabla \phi \frac{\partial}{\partial \phi} + \vec{B}_0 \cdot \nabla \theta \frac{\partial}{\partial \theta} \right) \quad (3.3)$$

A representation of the wavefields using exponentials in poloidal and toroidal directions gives an easy access to the values of the partial derivatives $\partial/\partial\theta$ and $\partial/\partial\phi$, making the evaluation of k_{\parallel} much easier.

Note that in a kinetic plasma description with no assumption on the smallness of the ion gyroorbit size (the so-called "all-order" model) partial derivatives in all three directions are required. The AORSA 3D code (All-Orders Spectral Algorithm) that implements this model uses Fourier representation of the wave fields in all three coordinates which reduces the derivatives to algebraic operations [19, 20]. This method allows the solution of the wave equation without any restriction on the wavelength relative to the ion Larmor radius and with no limit on the retained cyclotron harmonic number. In a spectral representation, however, all modes can be coupled, which produces a very large dense matrix, as opposed to the finite element method. Inversion of such matrices requires computational resources of a totally different scale, tera-scale calculations. For example, one AORSA 3D run with $34 \times 34 \times 64$ Fourier modes requires 788 GB of memory and about 358 minutes on 1936 processors on the Seaborg computer of the National Energy Research Scientific Computing Center (the most powerful computer in the United States

available for unclassified research, a total of 6656 processors, peak performance of 10 teraflops, 7.8 terabytes of memory, data as of May 2003) [54].

3.2 Radial basis functions

Now a few more words about the interpolating functions in the radial direction. We have used two different sets of functions — polynomials of the first and third orders. In the first case, the basis functions are piecewise linear, also called "hat" functions (Figure 3.1a), in the second case they are piecewise cubic polynomials of special form, called Hermite cubics (Figure 3.1b).

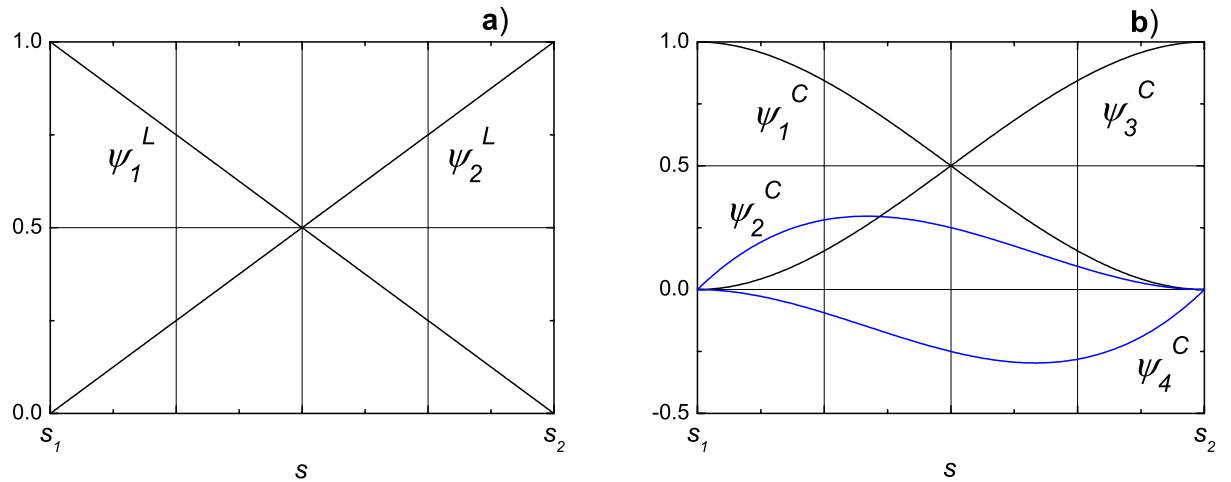


Figure 3.1. **a)** "Hat" basis functions for the linear FEM on one radial interval $[s_1, s_2]$, **b)** Hermite cubics interpolating functions. Absolute values of ψ_2^C and ψ_4^C scale with the size of the interval.

The functions $\psi_{ea}^{L,C}(s)$ have non-zero values on the mesh element e and are zero outside this element. Due to this, all the integral products $\int_0^1 \psi_{ea} \psi_{e'a'} ds$ arising from the volume integrals in Eq.(3.1) vanish if $e \neq e'$. This makes it possible to choose the indexing of the variables in such a way that the global matrix of the equation is diagonally banded (three diagonals for the linear FE and six diagonals for cubics).

The notation ψ_{ea} for finite elements is usually called *local representation* [52]. In this representation, the number of interpolating functions is larger than the actual number of independent coefficients, and a *location matrix* is used to put each contribution into the correct place in the global matrix. Introducing a local variable ξ varying from -1 to 1 on each radial element, the basis interpolation functions for the linear FEM in the local representation are given by the following expressions:

$$\begin{cases} \psi_{e1}^L = \frac{1}{2}(1 + \xi), \\ \psi_{e2}^L = \frac{1}{2}(1 - \xi) \end{cases} \quad (3.4)$$

and for Hermite cubics

$$\begin{cases} \psi_{e1}^C = \frac{1}{4}(\xi^3 - 3\xi + 2), \\ \psi_{e2}^C = \frac{1}{8}(\xi^3 - \xi^2 - \xi + 1)(s_2 - s_1), \\ \psi_{e3}^C = \frac{1}{4}(-\xi^3 + 3\xi + 2), \\ \psi_{e4}^C = \frac{1}{8}(\xi^3 + \xi^2 - \xi - 1)(s_2 - s_1), \\ \xi = \frac{2s - s_1 - s_2}{s_2 - s_1}. \end{cases} \quad (3.5)$$

Therefore, for Hermite cubic polynomials, we have the following values on the edges of each radial element:

$$\begin{aligned} \psi_{e1}^C|_{s_1} &= \psi_{e3}^C|_{s_2} = 1, \\ \psi_{e2}^C|_{s_1} &= \psi_{e4}^C|_{s_2} = 0, \\ \frac{d}{ds}\psi_{e1}^C|_{s_1} &= \frac{d}{ds}\psi_{e3}^C|_{s_2} = 0, \\ \frac{d}{ds}\psi_{e2}^C|_{s_1} &= \frac{d}{ds}\psi_{e4}^C|_{s_2} = 1. \end{aligned}$$

This choice of Hermite cubic basis functions is very convenient because it explicitly separates the value of the approximated solution from of the value of its derivative so that the coefficients at the functions ψ_{e2}^C and ψ_{e4}^C are exactly equal to the radial derivative of the discretised solution on the nodes.

3.3 Fourier harmonics

The summation over the Fourier modes in the discretisation (3.2) is done over the index l that labels all the mode couples (m, n) considered for perturbations. There is no strict rule as for the choice of the particular modes to be included in the calculations. The most intuitive "rule of thumb" is to surround the modes present in the antenna excitation with enough harmonics to account for the strongest couplings. So, for an (almost) axisymmetric geometry we would include more poloidal modes on both sides of the antenna, for a mirror configuration more harmonics in the toroidal direction are coupled and should be considered. A first indication of a reasonable selection of the perturbation mode table is that the wave amplitudes on the edge of the table are negligible in comparison with the maximum amplitude, usually located near the antenna strongest harmonic.

M	-7	-6	-5	-4	-3	-2	-1	0	1	2	3	4	5	6	7	8	9	10	N
-	-	-	-	-	-	-	-	-	-	-	-	-	-	-	-	-	-	-	-420
-	-	0	0	0	-	-	-	-	-	-	-	-	-	-	-	-	-	-	-360
-	0	0	*	0	0	-	-	-	-	-	-	-	-	-	-	-	-	-	-300
-	-	0	0	*	0	0	0	-	-	-	-	-	-	-	-	-	-	-	-240
-	-	-	0	*	*	*	0	0	0	0	-	-	-	-	-	-	-	-	-180
-	-	-	0	0	*	*	*	0	*	0	-	-	-	-	-	-	-	-	-120
-	-	-	0	0	0	*	*	*	*	0	0	-	-	-	-	-	-	-	-60
-	-	-	0	*	0	*	*	*	*	*	0	-	-	-	-	-	-	-	0
-	-	-	0	0	0	0	*	*	A	*	0	0	-	-	-	-	-	-	60
-	-	-	-	-	-	0	0	0	*	*	*	0	0	-	-	-	-	-	120
-	-	-	-	-	-	-	0	0	0	*	*	*	0	0	-	-	-	-	180
-	-	-	-	-	-	-	-	0	0	*	*	0	0	0	-	-	-	-	240
-	-	-	-	-	-	-	-	-	0	0	0	*	0	0	-	-	-	-	300
-	-	-	-	-	-	-	-	-	-	-	-	0	0	0	0	0	-	-	360
-	-	-	-	-	-	-	-	-	-	-	-	-	0	0	0	0	-	-	420
-	-	-	-	-	-	-	-	-	-	-	-	-	-	-	-	-	-	-	480

Figure 3.2. *Example of perturbation harmonic table: structure of couplings in a helical configuration. The toroidal mode numbers are multiples of 60 because of high periodicity $N = 60$ (and large aspect ratio). '-' means that the mode is not included in the calculations, '0' — included modes with the amplitude less than 10^{-4} of the maximum, '*' — bigger amplitudes, 'A' — antenna mode.*

In LEMan, the modes to be included in the calculation are specified in an external formatted file in a form of a table. After the run, the code analyses the perturbation amplitudes and plots a trace of the initial table with an indication of small and large amplitudes. An example of the amplitude trace is shown in Figure 3.2.

This calculation is done for an equilibrium with dominating helical terms, so the main couplings are of helical nature. For simplicity, the antenna has only one Fourier mode. In consequence, most of the large amplitudes are located near the diagonal passing through the antenna excitation mode, so in this case it is more efficient to distribute the included modes along this diagonal. Of course, this visualisation is only an indication of the consistency of the numerical results. More accurate quantitative estimates of convergence are discussed later in the section 3.11.

3.4 Vector projections

To be able to apply the discretisation method described in the previous section, a set of basis vectors for \vec{A} and $\nabla\tilde{\phi}$ projections has to be chosen. Two obvious options are the covariant and contravariant representations:

$$\begin{aligned}\vec{A} &= A_s \nabla s + A_\theta \nabla \theta + A_\phi \nabla \phi, \\ \vec{A} &= A^s \frac{\partial s}{\partial \vec{r}} + A^\theta \frac{\partial \theta}{\partial \vec{r}} + A^\phi \frac{\partial \phi}{\partial \vec{r}}.\end{aligned}\tag{3.6}$$

However, neither of these two projections is convenient for us. First, only one of the two operators $\nabla \times \vec{A}$ and $\nabla \cdot \vec{A}$ present in Eq.(3.1) can be expressed in a simple form with one of the two representations (3.6):

$$\begin{aligned}\nabla \times \vec{A} &= \frac{1}{\sqrt{g}} \epsilon_{ijk} \frac{\partial A_j}{\partial u_i} \vec{e}_k, \\ \nabla \cdot \vec{A} &= \frac{1}{\sqrt{g}} \frac{\partial}{\partial u_i} (\sqrt{g} A^i),\end{aligned}\tag{3.7}$$

where the standard convention for the covariant and contravariant components and for summation over repeating indices is used, \sqrt{g} is the Jacobian in curvilinear coordinates and ϵ_{ijk} is the completely antisymmetric pseudotensor (Levi-Civita symbol).

If we choose a covariant basis for \vec{A} then the curl operator takes a simple form (3.7), but the divergence becomes more complicated, and vice versa. Another thing to consider is the boundary conditions which are not evident to impose for the covariant or contravariant representations.

In this work, we have chosen the so-called "physical" representation for the \vec{A} components. In this case, the basis is formed by the normal, binormal and parallel directions to the magnetic field line:

$$\vec{A} = A_n \vec{e}_n + A_b \vec{e}_b + A_{\parallel} \vec{e}_{\parallel} = A_n \frac{\nabla s}{|\nabla s|} + A_b \frac{\vec{B} \times \nabla s}{B |\nabla s|} + A_{\parallel} \frac{\vec{B}}{B}. \quad (3.8)$$

The first advantage of the physical basis is the form of the boundary conditions, which become trivial. The dielectric tensor $\hat{\epsilon}$ is also very simple in this case. The expression (2.29) can be applied directly because the unit basis vectors $(\vec{e}_n, \vec{e}_b, \vec{e}_{\parallel})$ are orthogonal and \vec{e}_{\parallel} is directed along the magnetic field. The physical representation locally separates the response of the plasma along the magnetic field line from the one in perpendicular direction, which, in some situations, can simplify the analysis of the results. For example, in a scenario with a local Alfvén resonance in the plasma the short wavelength oscillations of the converted wave are best seen if the parallel component of \vec{A} is separated from the other components. A covariant or contravariant representations mix all three physical components, so the picture would be less clear in this case.

3.5 Expansion of the wave equation

Of course, choosing A_n , A_b and A_{\parallel} as the projections we lose the simplicity of the curl or divergence operators that a covariant or contravariant representations could provide. However, this is not of a big concern to us because the expansion of the analytical expressions involved in the equation (3.1) is done in an automated way. This is probably the

only possible way to proceed in a general 3D geometry due to a huge number of terms that the expanded version of Eq.(3.1) gives rise to. We believe the technique developed here to be of particular interest for any 3D application involving simple, but very long, repetitive and tedious calculations, so let us describe it in more detail.

In order to write down the expansion of the Galerkin form (3.1) in terms of trivial mathematical operations ready to be coded on a computer, we need to express the differential operators, scalar and vector products in terms of scalars. Since the curl and divergence operators are known for covariant and contravariant representations but not for the physical components of \vec{A} , we introduce two transformation matrices to pass from one representation to the other:

$$\begin{pmatrix} A^s(s, \theta, \phi) \\ A^\theta(s, \theta, \phi) \\ A^\phi(s, \theta, \phi) \end{pmatrix} = \widehat{TU}(s, \theta, \phi) \begin{pmatrix} A_n(s, \theta, \phi) \\ A_b(s, \theta, \phi) \\ A_{\parallel}(s, \theta, \phi) \end{pmatrix}. \quad (3.9)$$

and

$$\begin{pmatrix} A_s(s, \theta, \phi) \\ A_\theta(s, \theta, \phi) \\ A_\phi(s, \theta, \phi) \end{pmatrix} = \widehat{TL}(s, \theta, \phi) \begin{pmatrix} A_n(s, \theta, \phi) \\ A_b(s, \theta, \phi) \\ A_{\parallel}(s, \theta, \phi) \end{pmatrix}, \quad (3.10)$$

where (A^s, A^θ, A^ϕ) and (A_s, A_θ, A_ϕ) are the covariant and contravariant components of \vec{A} . Matrices $\widehat{TU}(s, \theta, \phi)$ and $\widehat{TL}(s, \theta, \phi)$ define the geometry of the configuration; they are calculated from the equilibrium quantities obtained from TERPSICHORE — $B(s, \theta, \phi)$, $I(s)$, $J(s)$, $\psi(s)$, $\Phi(s)$ and the metric elements $g_{ij}(s, \theta, \phi)$. The derivation of the matrix elements in the Boozer coordinate frame is presented in the Appendix.

Using matrices \widehat{TU} , \widehat{TL} we can now develop the expressions for the physical projections of differential operators (3.7):

$$\begin{aligned} (\nabla \times \vec{A})_l^{ph} &= \frac{1}{\sqrt{g}} \epsilon_{ijk} \frac{\partial (\widehat{TL}_{jp} A_p^{ph})}{\partial u_i} \widehat{TL}_{kl}, \\ \nabla \cdot \vec{A} &= \frac{1}{\sqrt{g}} \frac{\partial}{\partial u_i} (\sqrt{g} \widehat{TU}_{ik} A_k^{ph}). \end{aligned} \quad (3.11)$$

To construct the global matrix of the Galerkin form, these operators should be expanded into long sums. We see that the curl operator alone contains 36 basic terms. When multiplied by its counterpart with a test function ($\nabla \times \vec{F}^*$) this number squares. Together with the other operators in the equation (3.1) this results in thousands of terms! These terms are very simple, but their sheer number makes it practically impossible to perform the analytical expansion by hand. Although hard, it is still feasible in a two-dimensional configuration, but a 3D geometry with no symmetry to profit from requires a different approach.

In the present work, we use a symbolic manipulation software, Mathematica [55], to automate the development of the sums. This package is designed, among other things, for handling complex symbolic calculations involving very large number of terms. The operators in the equation (3.1) can be programmed into a Mathematica script in a symbol form. The computer then makes a complete expansion of the equation and combines the coefficients of the terms $F_i^* A_j$. This development is done analytically. The script then generates a Fortran code for these analytical expressions. The code can be directly inserted into the main program and used to evaluate numerically the global matrix coefficients.

The first and evident advantage of this method is an economy of time. Writing the script for Mathematica is much faster than expanding the equations by hand. Also, possible misprints are avoided, which is very important for such a large number of terms. Another advantage lies in the flexibility of the approach. For example, if we wanted to change the variables (as, in fact, is done and described in the section 3.9 on page 45), or include a certain symmetry in the geometry, the traditional procedure would require a very long and meticulous recalculation of the terms. With the method described above it only takes a few minutes to change the script and generate a new Fortran code to be inserted in the main module. This allows for much easier implementation of different models and numerical schemes in 3D geometry. This flexibility was particularly important at the stage of developing and testing the LEMan code.

3.6 Matrix construction

After all the coefficients in the equation (3.1) are obtained analytically, we apply the discretisation (3.2) both to the variables $\vec{A}, \tilde{\phi}$ and to the test functions \vec{F}, G :

$$\begin{aligned} A_j(s, \theta, \phi) &= \sum_{r,m,n} A_j^{rmn} \psi_r(s) e^{i(m\theta+n\phi)}, & \tilde{\phi}(s, \theta, \phi) &= \sum_{r,m,n} \tilde{\phi}^{rmn} \psi_r(s) e^{i(m\theta+n\phi)}, \\ F_j(s, \theta, \phi) &= \sum_{r',m',n'} F_j^{r'm'n'} \psi_{r'}(s) e^{i(m'\theta+n'\phi)}, & G(s, \theta, \phi) &= \sum_{r',m',n'} G^{r'm'n'} \psi_{r'}(s) e^{i(m'\theta+n'\phi)}, \end{aligned} \quad (3.12)$$

where j stands for one of the components (n, b, \parallel) and r is the combined from (e, a) global radial index.

The discretised form of the Galerkin principle is then written as

$$\begin{aligned} \sum_{\substack{rmnk \\ i=0..3}} A_k^{rmn} C_{ik}^A(s, \theta, \phi) \frac{\partial}{\partial u_i} (\psi_r(s) e^{i(m\theta+n\phi)}) & \cdot \\ \sum_{\substack{r'm'n'k' \\ j=0..3}} F_{k'}^{r'm'n'*} C_{jk'}^F(s, \theta, \phi) \frac{\partial}{\partial u_j} (\psi_{r'}(s) e^{-i(m'\theta+n'\phi)}) & = \text{RHS}, \end{aligned} \quad (3.13)$$

where $u_1 = s, u_2 = \theta, u_3 = \phi$, while the label $\frac{\partial}{\partial u_0}$ implies that no derivative is performed. For ease of notation, we define here the index $k = 1..4$ that runs over all components of \vec{A} and $\tilde{\phi}$ such that $A_{1,2,3} \equiv A_{n,b,\parallel}$ and $A_4 \equiv \tilde{\phi}$.

As can be seen from this expression, we do not completely expand the equation in the analytical form and do not open the last sums to multiply the coefficients $C_{ik}^A C_{jk'}^F$. Otherwise, even though the analytical development of the coefficients is done automatically, the number of terms in the completely expanded form is so large that it noticeably slows down the calculations. It turns out to be faster to do the last step of the development numerically. This reduces the number of terms to be evaluated by a factor of the square root of the number of coefficients.

The continuous wave equation (3.1) should be satisfied with any arbitrary test functions \vec{F}, G . In consequence, its discretised analogue (3.13) should hold for any set of coefficients $F_j^{r'm'n'}, G^{r'm'n'}$. This is only possible if the amplitudes $A_j^{rmn}, \tilde{\phi}^{rmn}$ are a solution of an equation that can be cast in a simple matrix form

$$\hat{M} \cdot A = J, \quad (3.14)$$

where A is a vector composed of all the sought amplitudes $\{A_j^{r mn}, \tilde{\phi}^{r mn}\}$ and the right hand side J is the antenna contribution. The final expression for the elements of the matrix \hat{M} as volume integrals is given by:

$$M_{rr'kk'}^{mm'nn'} = \int_{\Omega} dV \left[\sum_{i,j=0}^3 C_{ijkk'}(s, \theta, \phi) \frac{\partial}{\partial u_i} (\psi_r(s) e^{i(m\theta+n\phi)}) \frac{\partial}{\partial u_j} (\psi_{r'}(s) e^{-i(m'\theta+n'\phi)}) \right], \quad (3.15)$$

where we use the same notation for k and the derivatives as in (3.13).

The structure of the matrix \hat{M} depends on the indexing of the variables that can be chosen in a way that minimises the storage and the matrix inversion time. To do so, the amplitudes that are coupled the most should be grouped in the matrix as close as possible to each other. The innermost index runs over the \vec{A} components n, b, \parallel and $\tilde{\phi}$. These groups of 4 unknowns are combined into larger blocks of different Fourier modes. The resulting blocks with the size $4N_{mn}$ by $4N_{mn}$ (N_{mn} — total number of the perturbed harmonics) are, in a general 3D geometry, dense because of the coupling between different harmonics through the equilibrium. In each block, all the variables have the same radial finite element index. Finally, these blocks are combined into the global matrix \hat{M} . The outermost index, therefore, labels the radial variable dependence.

This indexing has a very important advantage of making the global matrix block-diagonal. Indeed, in the case of localised finite elements (3.4) or (3.5), the radial integral in Eq.(3.15) can only contribute to the matrix element if the kernels of corresponding FE interpolation functions ψ_r, ψ_r' are not located too far away and overlap. For linear FE, the matrix is block tridiagonal, for Hermite cubics the number of non-null diagonal blocks increases to six. All the off-diagonal elements of the matrix M are filled with zeros and are not stored, which largely reduces the memory requirements.

After the global matrix is constructed as described, the explicit boundary conditions are imposed on the last radial element, and unicity on the axis, without changing the block-diagonal property of the matrix. An example of the matrix structure for cubic FE is illustrated in Figure 3.3. The number of harmonics and radial elements for this case is very low for the sake of simplicity.

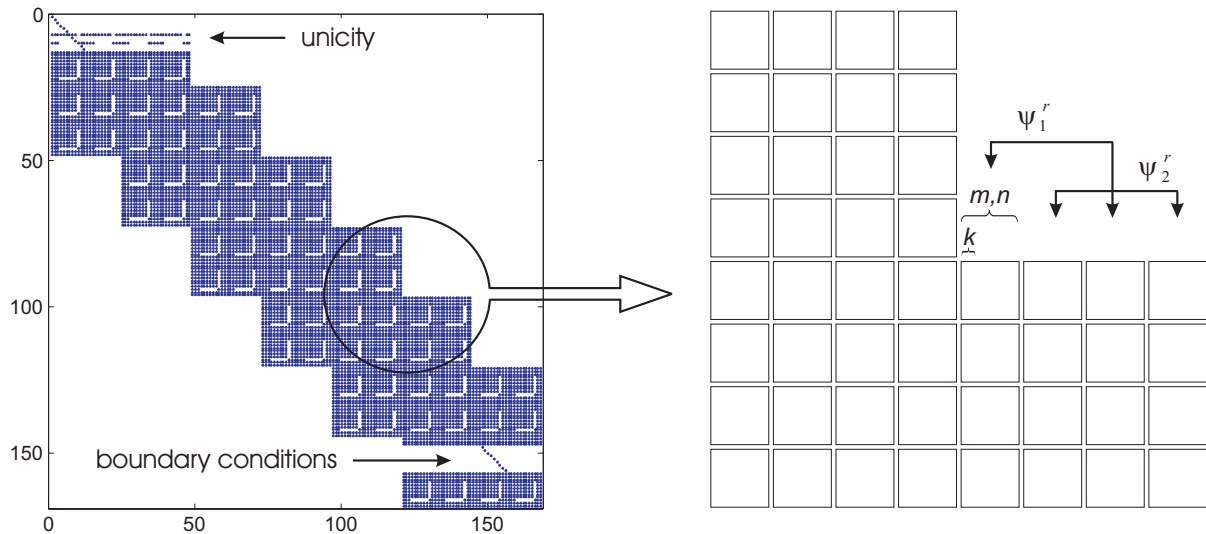


Figure 3.3. *Global matrix structure for Hermite cubic finite elements. Number of radial elements $N_s = 6$, total number of harmonics $N_{mn} = 3$.*

3.7 Construction optimisation

The construction of the global matrix, i.e. the evaluation of the volume integrals can potentially be the most time-consuming part of the calculations. While the direct computation of the integrals (3.15) is reasonably fast for simple 1D or even 2D configurations, the time of calculations becomes crucial for realistic 3D plasmas. Fortunately, there is a way to considerably accelerate it, taking advantage of the Fourier decomposition used for the discretisation.

The coefficients $C_{ijkk'}(s, \theta, \phi)$ store the information about the equilibrium quantities (metric elements, magnetic field) and the dielectric tensor, but do not depend on the perturbation modes for the cold plasma model. This fact is used to optimise the evaluation of the volume integrals. Instead of calculating the integrals (3.15) directly in real space, the equilibrium coefficients $C_{ijkk'}(s, \theta, \phi)$ are first Fourier-transformed in the poloidal and toroidal angles and only then combined with contributions from the perturbations. This

limits the number of 3D integrals to be evaluated by the number of equilibrium Fourier modes, which is usually much smaller than the number of all possible combinations of the perturbed mode pairs $(m, n), (m', n')$.

The integrals (3.15) are thus reduced to 1D radial integrals of the sums of Fourier coefficients. The numerical quadrature of these integrals is done with the Gaussian method. Only one equilibrium Fourier mode contributes to the sum for each given combination (m, n, m', n') . Fast Fourier Transform in both angles is implemented in order to speed up the evaluation of the equilibrium Fourier amplitudes. The FFT technique is very efficient, its runtime scales as $N \log N$, where N is the number of harmonics. This scaling is much slower than the solution of the matrix equation (3.14), which makes the time required for the Fourier discretisation a negligible fraction of the total runtime for typical 3D configurations.

This method is faster by orders of magnitude than the direct evaluation of the volume integrals in real space for each perturbation mode. For comparison, for a simple 3D test configuration a run for one antenna frequency takes only 90 seconds instead of 10 hours for the algorithm with real-space integral evaluation.

3.8 Boundary and gauge conditions

An explicit separation of the normal, binormal and parallel components of \vec{A} makes the boundary conditions particularly simple: all the tangential components of \vec{A} and $\nabla\tilde{\phi}$ should vanish on the conducting shell surrounding the plasma

$$A_b = 0, \quad A_{\parallel} = 0, \quad \tilde{\phi} = 0. \quad (3.16)$$

This condition can be easily imposed in the equation matrix by forcing the corresponding edge values to 0.

The Coulomb gauge condition is more subtle. It cannot be imposed directly on the whole calculation domain, but, as it was shown above, it should be sufficient to impose it on the boundary only. It can be done on the external boundary by eliminating the

surface term $\int_{\delta\Omega} d\vec{S} \cdot \vec{F}^*(\nabla \cdot \vec{A})$ in the integral form (3.1), as usual for the Neumann-type conditions. The situation with the axis is more complicated. In some sense, it plays a role of an internal boundary for the FEM. Unfortunately, it is not possible to impose $\nabla \cdot \vec{A} = 0$ in the same way because all the surface terms vanish on the axis anyway. However, the numerical scheme together with the special treatment of the axis to assure the unicity of the solution described in the next section seems to naturally produce a divergence-free solution. As it will be shown later, the contribution of the $\nabla \cdot \vec{A}$ terms in the equation (2.21) is small compared to the main terms and it converges with increasing size of radial grid and the number of Fourier modes.

3.9 Unicity on the axis

\vec{A} and $\tilde{\phi}$ have to be uniquely defined on the magnetic axis. It means that projections of \vec{A} on a basis that does not become singular on the axis should not depend on the poloidal angle θ . Such a basis can be for example a Cartesian grid, or, more conveniently, cylindrical coordinates (R, φ, Z) (R — major radius from the axis of symmetry, φ — geometrical toroidal angle, Z — height above the midplane):

$$\begin{aligned} A_R &= \vec{A} \cdot \vec{e}_R = A_n \vec{e}_R \cdot \vec{e}_n + A_b \vec{e}_R \cdot \vec{e}_b + A_{\parallel} \vec{e}_R \cdot \vec{e}_{\parallel}, \\ A_{\varphi} &= \vec{A} \cdot \vec{e}_{\varphi} = A_n \vec{e}_{\varphi} \cdot \vec{e}_n + A_b \vec{e}_{\varphi} \cdot \vec{e}_b + A_{\parallel} \vec{e}_{\varphi} \cdot \vec{e}_{\parallel}, \\ A_Z &= \vec{A} \cdot \vec{e}_Z = A_n \vec{e}_Z \cdot \vec{e}_n + A_b \vec{e}_Z \cdot \vec{e}_b + A_{\parallel} \vec{e}_Z \cdot \vec{e}_{\parallel}. \end{aligned}$$

or in matrix form using a transformation matrix \hat{T} :

$$\begin{pmatrix} A_R(\phi) \\ A_{\varphi}(\phi) \\ A_Z(\phi) \end{pmatrix} = \hat{T}(\theta, \phi) \begin{pmatrix} A_n(\theta, \phi) \\ A_b(\theta, \phi) \\ A_{\parallel}(\theta, \phi) \end{pmatrix}, \quad s = 0. \quad (3.17)$$

In the geometry of a cylinder with circular cross-section, the unicity condition takes a very simple form and can be shown to be related to the gauge condition $\nabla \cdot \vec{A} = 0$ on the axis. In a cylinder, Boozer angles θ and ϕ become simply the geometrical angles and

relation (3.17) can be explicitly written as

$$\begin{cases} A_R = A_n \cos \theta - A_b \sin \theta, \\ A_\varphi = A_n \sin \theta + A_b \cos \theta, \\ A_Z = A_\parallel. \end{cases} \quad (3.18)$$

Here, we omit the ϕ -dependence of \vec{A} for clarity. Using Fourier decomposition of the components A_n, A_b

$$\begin{aligned} A_n &= \sum_m A_n^m e^{im\theta}, \\ A_b &= \sum_m A_b^m e^{im\theta}, \end{aligned}$$

substituting it in equations (3.18) and remembering that the resulting components A_R, A_φ and A_Z should not depend on θ , we obtain the relation between the Fourier amplitudes on the axis:

$$\begin{cases} iA_n^1 - A_b^1 = 0 \\ iA_n^{-1} + A_b^{-1} = 0 \\ A_{n,b}^m = 0 \quad \forall m \neq \pm 1 \end{cases} \quad (3.19)$$

and for the scalars A_\parallel and $\tilde{\phi}$

$$A_\parallel^m, \tilde{\phi}^m = 0 \quad \forall m \neq 0. \quad (3.20)$$

As a remark, we note that these Fourier amplitudes appear in exactly the same combination in the expression for divergence of the vector potential on the axis in cylindrical geometry. Writing the divergence in cylindrical coordinates, we have

$$\nabla \cdot \vec{A} = \frac{\partial A_n}{\partial r} + \frac{1}{r} (A_n + imA_b) + ik_z A_z.$$

If the unicity (3.19) is not satisfied, the second term in this expression has a singularity on the axis.

For higher-order interpolating functions, it is possible to require the unicity of the electric and magnetic fields \vec{E} and \vec{B} as well. This is achieved if the partial derivatives $\partial/\partial R, \partial/\partial Z$ of the cylindrical components of \vec{A} do not depend on θ either. In this case,

unicity condition involves derivatives of the equilibrium quantities on the axis. Unfortunately, numerical equilibrium data is usually less precise and not smooth enough near the axis, so derivatives do not generally behave very well. This could be resolved by using an asymptotic analytical solution for the equilibrium as done, with some assumptions, in 2D geometry in the PENN code [15], but for a general 3D configuration it is not easy.

Another problem with imposing the unicity condition in the form (3.17) resides in the spectral representation of \vec{A} and $\tilde{\phi}$. While it is quite evident how to impose the relation (3.17) in real space when 2D or 3D finite elements are used, it becomes less simple in Fourier space. In real space on a grid with N_θ angular mesh points, equation (3.17) yields $N_\theta - 1$ equations on the axis values for each component, leaving one degree of liberty for the actual value. In Fourier space, both \vec{A} components and the transformation matrix \hat{T} coefficients have to be Fourier-decomposed. $\hat{T} \cdot \vec{A}$ becomes a double sum in Fourier index with the total number of terms equal to the number of perturbed harmonics plus the number of modes needed to describe the equilibrium. Equation (3.17) then leads to more constraints on the amplitudes on the axis than the actual number of variables, and it is not always clear which of those equations have to be neglected.

This analysis and the resulting relation between the axial perturbation amplitudes can be easily obtained in a circular cross-section cylindrical geometry, as shown above. However, even for still cylindrical, but a non-circular shaped configuration the relation becomes much less evident, involving many mode numbers. In a general 3D geometry with a non-planar axis the unicity condition is much more complicated.

Because of these reasons, we have used a different method to treat the axis, similar to the implementation in TERPSICHORE. Instead of imposing something on \vec{A} and $\tilde{\phi}$, we define new variables multiplying the normal and binormal components by the radial label s :

$$\begin{aligned}\xi_n(s, \theta, \phi) &= sA_n(s, \theta, \phi), \\ \xi_b(s, \theta, \phi) &= sA_b(s, \theta, \phi).\end{aligned}\tag{3.21}$$

Imposing axis values on the new variables ξ_n and ξ_b now becomes trivial:

$$\xi_{n,b} |_{s=0} = 0.\tag{3.22}$$

For the scalars A_{\parallel} and $\tilde{\phi}$ the unicity condition remains in the very simple form (3.20) for any toroidal mode number n .

In this case, the relation between the values A_n , A_b on the axis is not imposed directly, but is adjusted in a consistent way by the equation. The unicity of the resulting solution can then be verified a posteriori. An analysis of the numerical solutions obtained with this method in section 3.12 confirms the validity of such approach.

3.10 Antenna

We are studying the problem of propagation of waves launched into plasma by a prescribed antenna. In the cold plasma model, with no thermal motion of particles and therefore no associated thermal energy, the antenna excitation is the only generator of perturbations. In the present work, we concentrate our interest on the response of the plasma to an external source, on the structure of the perturbed wavefields in different scenarios at different frequencies. At this stage, we did not aim at implementing a realistic antenna design. In principle, specifying an antenna of a realistic shape in the code is a straightforward procedure. However, to simplify the analysis of the results and to minimise the number of excited modes, the calculations here were done for a model antenna with a relatively simple, but still physically relevant geometry. This is a reasonable simplification, and an extension to a realistic design is not complicated.

The antenna here is prescribed by specifying the current density in the right-hand side of the non-homogeneous equation (2.21) in an explicitly divergence-free form using an antenna potential $\sigma(s, \theta, \phi)$:

$$\vec{j}_{ant} = \nabla s \times \nabla \sigma(s, \theta, \phi). \quad (3.23)$$

The shape of the antenna is defined by the function σ . In LEMan, it is specified in real space as a function of all three coordinates, which gives a relative freedom in choosing the antenna geometry. We have implemented two types of antenna: a simple helical antenna with one or several poloidal and toroidal harmonics, and an antenna localised in

the poloidal direction. Two types of localised antenna were used for tokamak simulations — the low-field side and the high-field side antennae.

The helical antenna was used for most of the 1D and 3D calculations; it is described by the following expression for σ :

$$\sigma(s, \theta, \phi) = \sum_{m_a n_a} \sigma_s^{m_a n_a}(s) e^{i(m_a \theta + n_a \phi)},$$

where the amplitudes $\sigma_s^{m_a n_a}$ that specify the radial extension of the antenna are usually chosen as polynomials of second or fourth order between two surfaces s_1, s_2 . Radially, the antenna is located in the vacuum, or, in a fixed-boundary equilibrium, inside the plasma.

The second type, the poloidally localised antenna that was mostly used for calculations in the ion-cyclotron range of frequencies is specified as

$$\sigma(s, \theta, \phi) = \sigma_s(s) \sigma_\theta(\theta) e^{i n_a \phi},$$

where the radial extension is defined in the same way as for the helical antenna, and $\sigma_\theta(\theta)$ is a polynomial in an interval of θ 's corresponding to either the internal high-field side or the external low-field side and zero outside this interval. This model of the antenna is very similar to the one implemented in the LION [13, 56] code with an extension to 3D geometry.

To substitute the antenna current density into the wave equation (3.1), it has to be projected onto the local magnetic basis:

$$\vec{j} = j_n \frac{\nabla s}{|\nabla s|} + j_b \frac{\vec{B} \times \nabla s}{B |\nabla s|} + j_{\parallel} \frac{\vec{B}}{B}.$$

(we will omit the subscript *ant* for ease of notation). Developing the expression (3.23), we first obtain the contravariant components of \vec{j} :

$$\vec{j} = \frac{\partial \sigma}{\partial \theta} \nabla s \times \nabla \theta + \frac{\partial \sigma}{\partial \phi} \nabla s \times \nabla \phi,$$

hence the components are

$$\begin{cases} j^s = & 0, \\ j^\theta = & -\frac{1}{\sqrt{g}} \frac{\partial \sigma}{\partial \phi}, \\ j^\phi = & \frac{1}{\sqrt{g}} \frac{\partial \sigma}{\partial \theta}. \end{cases}$$

Using the transformation matrices \widehat{TU} , \widehat{TL} defined in Eqs.(3.9) – (3.10) and substituting σ , we find the final expressions for the physical components of the antenna currents implemented in the code:

$$\begin{cases} j_n = 0, \\ j_b = \frac{1}{\sqrt{g}} \left(\frac{\partial \sigma}{\partial \theta} \widehat{TL}_{32} - \frac{\partial \sigma}{\partial \phi} \widehat{TL}_{22} \right), \\ j_{\parallel} = \frac{1}{\sqrt{g}} \left(\frac{\partial \sigma}{\partial \theta} \widehat{TL}_{33} - \frac{\partial \sigma}{\partial \phi} \widehat{TL}_{23} \right). \end{cases} \quad (3.24)$$

3.11 Diagnostics and power balance

Diagnostic calculations are a very important part of the LEMan code. By diagnostics we mean all the quantities derived from the direct solution $\vec{A}, \tilde{\phi}$. These include the perturbed magnetic and electric fields, Poynting vector, absorbed power, antenna coupling etc. These quantities are not only interesting as such, but they can also provide a lot of information about the self-consistency of the solution and provide a measure of the accuracy of the numerical approximation.

One of the properties of the numerical scheme to be fulfilled is the uniqueness of the solution on the magnetic axis. It is important to be verified because an incorrect treatment of the axis region can lead to unphysical energy sinks at the origin of the coordinate system. The uniqueness can be checked by calculating the cylindrical projections of the vector potential and E/M fields on the axis; more details and some numerical results are presented in the section 3.12.

Another simple verification of the solution is provided by the value of the parallel component of the perturbed electric field. As pointed out in [15] in the plasma model with finite electron mass, a non-trivial cancellation has to occur between the terms in $E_{\parallel} = -\nabla \phi_{\parallel} + ik_0 A_{\parallel}$ to account for the fast relaxation of the electrons along the magnetic field lines. Indeed, at low perturbation frequencies, the parallel component of the electric field is much smaller than the normal and binormal components apart from the points of resonance.

The most rigorous quantitative verification is provided by the energy conservation law.

Not only the total energy coupled in the antenna should be equal to the energy absorbed in the plasma, but a similar relation should hold locally for each magnetic surface.

Energy conservation with a correction involving terms with $\nabla \cdot \vec{A}$ can be directly obtained from the Galerkin form of the wave equation (3.1) by setting $\vec{F} = \vec{A}$ and $G = \tilde{\phi}$. Substituting the definitions (2.17), (2.18) into the integral form (3.1) and simplifying, we obtain:

$$\begin{aligned} & \int_{\Omega} dV \left[-|B|^2 + \vec{E}^* \cdot (\hat{\epsilon} \cdot \vec{E}) - |\nabla \cdot \vec{A}|^2 \right] + \\ & \int_{\delta\Omega} d\vec{S} \left[\frac{i}{k_0} \vec{E}^* \times \vec{B} + \frac{i}{k_0} \nabla \tilde{\phi}^* \times \vec{B} + \tilde{\phi}^* \hat{\epsilon} \cdot \vec{E} + \vec{A}^* (\nabla \cdot \vec{A}) \right] \\ & = -\frac{4\pi i}{ck_0} \int_{\Omega} dV \left(\vec{E}^* \cdot \vec{j}_{ant} + \nabla \tilde{\phi}^* \cdot \vec{j}_{ant} \right). \end{aligned} \quad (3.25)$$

Application of Gauss' theorem to the underlined terms yields

$$\int_{\delta\Omega} d\vec{S} \left[\frac{i}{k_0} \nabla \tilde{\phi}^* \times \vec{B} + \tilde{\phi}^* \hat{\epsilon} \cdot \vec{E} \right] = \int_{\Omega} dV \left[-\frac{i}{k_0} \nabla \tilde{\phi}^* \cdot (\nabla \times \vec{B}) + \underbrace{\tilde{\phi}^* \nabla (\hat{\epsilon} \cdot \vec{E})}_{\text{underbraced}} + \nabla \tilde{\phi}^* \cdot (\hat{\epsilon} \cdot \vec{E}) \right].$$

Using the second equation in (2.21), we find that the underbraced term is equal to zero for $\rho_{ext} = 0$. The two remaining terms can be simplified expressing \vec{E} and \vec{B} back in terms of the potentials:

$$[\dots] = -\frac{i}{k_0} \nabla \tilde{\phi}^* \cdot \left[\nabla (\nabla \cdot \vec{A}) - \nabla^2 \vec{A} - k_0^2 \epsilon \cdot \vec{A} - ik_0 \hat{\epsilon} \cdot \nabla \tilde{\phi} \right] = \dots$$

using the first equation in (2.21)

$$\dots = -\frac{i}{k_0} \nabla \tilde{\phi}^* \cdot \left[\nabla (\nabla \cdot \vec{A}) + \frac{4\pi}{c} \vec{j}_{ant} \right].$$

Finally, combining this with the equation (3.25), we obtain the power balance with $\nabla \cdot \vec{A}$ corrections:

$$\begin{aligned} & \int_{\Omega} dV \left[-\frac{\omega}{8\pi} (|B|^2 - \vec{E}^* \cdot (\hat{\epsilon} \cdot \vec{E})) + \frac{i}{2} \vec{E}^* \cdot \vec{j}_{ant} \right] + \int_{\delta\Omega} d\vec{S} \frac{ic}{8\pi} \vec{E}^* \times \vec{B} \\ & = \int_{\Omega} dV \left[\frac{\omega}{8\pi} |\nabla \cdot \vec{A}|^2 + \frac{ic}{8\pi} \nabla \tilde{\phi}^* \cdot \nabla (\nabla \cdot \vec{A}) \right] - \int_{\delta\Omega} d\vec{S} \frac{\omega}{8\pi} \vec{A}^* \cdot (\nabla \cdot \vec{A}). \end{aligned} \quad (3.26)$$

The first line of this equation describes the physical energy balance in an arbitrary volume Ω . The right-hand side amounts to the non-physical terms containing the divergence of \vec{A} . Note that the left-hand side can be directly derived from the wave equation in the field formulation (2.16). We could not use this equation in the derivation of Eq.(3.26) because the field and potential formulations are equivalent only if the Coulomb gauge is satisfied exactly, which, strictly speaking, is not necessarily the case for a numerical solution.

The physical power balance is therefore given by a simple relation of three integrals:

$$\begin{aligned}
P_{pla}(s) &= P_{ant}(s) + iS_{Poynt}(s), \\
P_{pla}(s) &= \frac{\omega}{8\pi} \int_{\Omega(s' < s)} dV' \left[|B|^2 - \vec{E}^* \cdot (\hat{\epsilon} \cdot \vec{E}) \right], \\
P_{ant}(s) &= \frac{i}{2} \int_{\Omega(s' < s)} dV' \left[\vec{E}^* \cdot \vec{j}_{ant} \right], \\
S_{Poynt}(s) &= \frac{c}{8\pi} \int_{\delta\Omega(s)} d\vec{S} \left[\vec{E}^* \times \vec{B} \right].
\end{aligned} \tag{3.27}$$

$P_{pla}(s)$ has a simple physical meaning of the total power absorbed in the plasma between the magnetic axis and the magnetic flux surface labeled s , $P_{ant}(s)$ is the power coupled in the antenna inside this surface and iS_{Poynt} is the inward power flux through this surface ($\frac{c}{8\pi} \vec{E}^* \times \vec{B}$ is the Poynting vector of an electromagnetic wave represented in complex notation). The real part of these variables corresponds to the reactive power, the imaginary part is the resistive power. It is worth recalling that in the cold plasma model the absorption in plasma is due to the small imaginary part introduced in the dielectric tensor¹. For simplicity, we do not separate here the contributions of the plasma and the vacuum regions. The power integrals are defined in exactly the same way in the plasma and vacuum; only the value of the dielectric tensor changes.

¹As a remark, the introduction of the "resistivity" in the cold plasma dielectric tensor should be done in a manner that respects causality. When done correctly, the cumulative integral of the resistive power $\Im(P_{pla}(s))$ is a monotonic function, which in itself provides a supplementary check of the self-consistency of the model.

It follows from the equation (3.26) that the discretisation method applied here is energy-conserving apart from the terms containing divergence of \vec{A} . As it was discussed previously in section 2.4, the *true* solution to the continuous problem is exactly divergence-free if the boundary conditions are imposed correctly. On the contrary, the *numerical* solution of the discretised problem can only converge to $\nabla \cdot \vec{A} = 0$, but the value of the divergence remains finite (in some sense, this is the price we pay for the fact that the potential formulation is pollution-free, but unlike in the polluted scheme of the field formulation, here we can quantitatively estimate the negative effect).

The value of $\nabla \cdot \vec{A}$ and its contribution to the power balance can thus be used as an estimate for the self-consistence and convergence of the numerical results. Another two values used here for the convergence evaluation are the relative averaged local and global power balances:

$$\begin{aligned}
\delta_d &= \int_{\Omega} |\nabla \cdot \vec{A}| dV V^{1/3} / \int_{\Omega} |\vec{A}| dV, \\
\delta_l &= \int_0^1 |P_{pla}(s) - P_{ant}(s) - iS_{Poynt}(s)| ds / P_{pla}(1), \\
\delta_g &= (P_{pla}(1) - P_{ant}(1)) / P_{pla}(1).
\end{aligned} \tag{3.28}$$

As an example of power balance, the three measures δ_d , δ_l and δ_g were calculated for a 2D configuration (a large aspect ratio torus with an elliptical cross-section of the plasma) in the Alfvén range of frequencies (Figure 3.4).

These results are obtained using Hermite cubics for the radial discretisation with a uniform grid. The mesh size less than ~ 30 nodes does not allow to resolve the short wavelength oscillations near the Alfvén resonant surface. With increasing N_s , δ_d and δ_g values rapidly converge up to the radial mesh size of ~ 100 points and then do not improve much because of the finite number of Fourier modes N_m and the imperfections of the underlying numerical equilibrium. The plot on the right shows an exponential convergence with the Fourier mode number up to $N_m \sim 13$ and then, again, finite limit due to the equilibrium imprecision and fixed N_s .

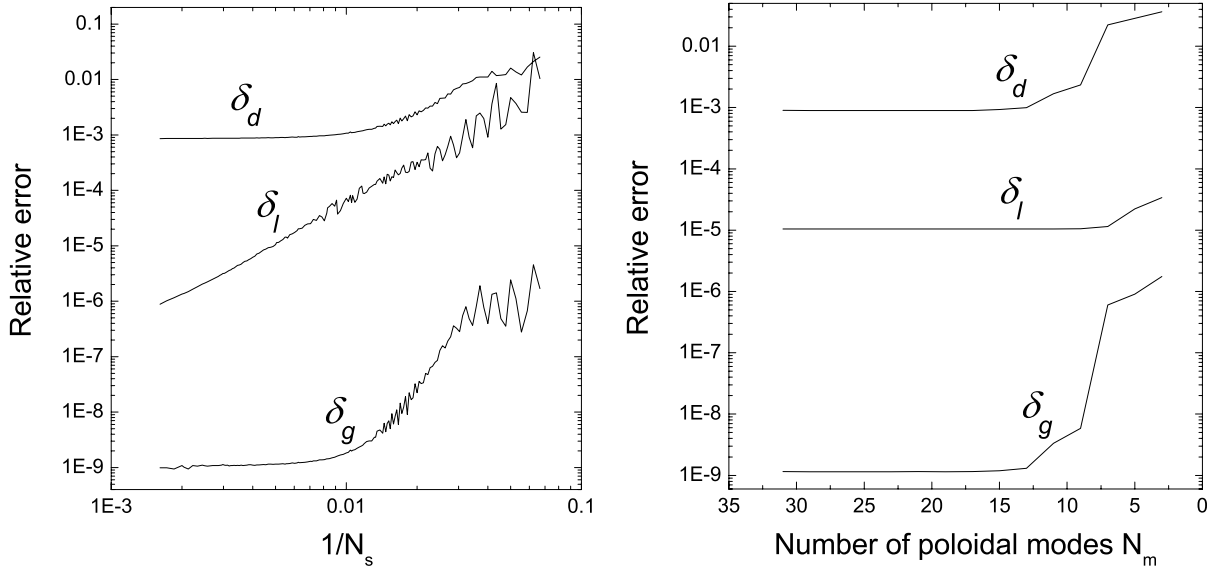


Figure 3.4. *Relative error of the power balance and precision of the Coulomb gauge. **Left:** Convergence with the radial mesh size N_s , the number of poloidal Fourier harmonics fixed ($N_m = 21$). **Right:** Convergence with the number of Fourier modes N_m , the radial mesh size fixed ($N_s = 200$).*

Among δ_l , δ_g and δ_d , the direct measure of the gauge error δ_d has the largest value here, but the effective contribution of $\nabla \cdot \vec{A}$ to the power integrals is much lower, as indicated by the values of δ_l and δ_g .

More examples of the power balance and convergence results for different configurations are discussed in the chapter 4.

3.12 Unicity check

As was mentioned before, we do not explicitly impose the unicity condition on all the components of the vector potential in the equation matrix. Therefore, it is necessary to verify that the resulting solution, indeed, has unique values on the axis. This can be done by evaluating the projections of \vec{A} on a cylindrical basis ($\vec{e}_R, \vec{e}_\varphi, \vec{e}_Z$).

We first express the cylindrical basis in terms of the contravariant basis vectors of

Boozer coordinates:

$$\begin{pmatrix} \vec{e}_R \\ \vec{e}_\varphi \\ \vec{e}_Z \end{pmatrix} = \begin{pmatrix} \nabla R \\ \nabla \varphi \\ \nabla Z \end{pmatrix} = \begin{pmatrix} \partial_s R & \partial_\theta R & \partial_\phi R \\ \partial_s \varphi & \partial_\theta \varphi & \partial_\phi \varphi \\ \partial_s Z & \partial_\theta Z & \partial_\phi Z \end{pmatrix} \cdot \begin{pmatrix} \nabla s \\ \nabla \theta \\ \nabla \phi \end{pmatrix} \equiv \hat{T}^{R\varphi Z} \cdot \begin{pmatrix} \nabla s \\ \nabla \theta \\ \nabla \phi \end{pmatrix}.$$

Now, to get an expression for $(\vec{e}_R, \vec{e}_\varphi, \vec{e}_Z)$ in terms of the normal, binormal and parallel directions, we use the \widehat{TU} transformation matrix from the physical basis $(\vec{e}_n, \vec{e}_b, \vec{e}_\parallel)$ to contravariant basis defined in the section 3.5 on page 37:

$$\begin{pmatrix} \vec{e}_R \\ \vec{e}_\varphi \\ \vec{e}_Z \end{pmatrix} = \hat{T}^{R\varphi Z} \cdot \widehat{TU} \cdot \begin{pmatrix} \vec{e}_n \\ \vec{e}_b \\ \vec{e}_\parallel \end{pmatrix}. \quad (3.29)$$

The resulting matrix $\hat{T}^{R\varphi Z} \cdot \widehat{TU}$ is used to transform the physical projections of \vec{A} on the cylindrical basis.

Calculation of this transformation matrix is quite delicate near the magnetic axis. Some of the coefficients ($\hat{T}_{11}^{R\varphi Z}$ and $\hat{T}_{31}^{R\varphi Z}$ for example) are singular at the origin of the system. In a zero-order approximation, R and Z are proportional to the minor radius $r \sim \sqrt{s}$, so their radial derivative diverges as $\sim 1/\sqrt{s}$. Ideally, this singular behaviour should cancel with the axis asymptotics of the \widehat{TU} elements, but this is hard to obtain numerically unless special care is taken to treat the singularities. It is very important to use an appropriate scheme to calculate these elements, especially when interpolation is involved.

In order to obtain the correct approximations of the derivatives near the axis, we single out the zero-order asymptotics with singular behaviour:

$$\begin{aligned} R(s, \theta, \phi) &= \sqrt{s} R_1(s, \theta, \phi), \\ Z(s, \theta, \phi) &= \sqrt{s} Z_1(s, \theta, \phi). \end{aligned}$$

The asymptotics can then be derived analytically, so the numerical derivation of the remaining slow-changing parts R_1 and Z_1 is straightforward.

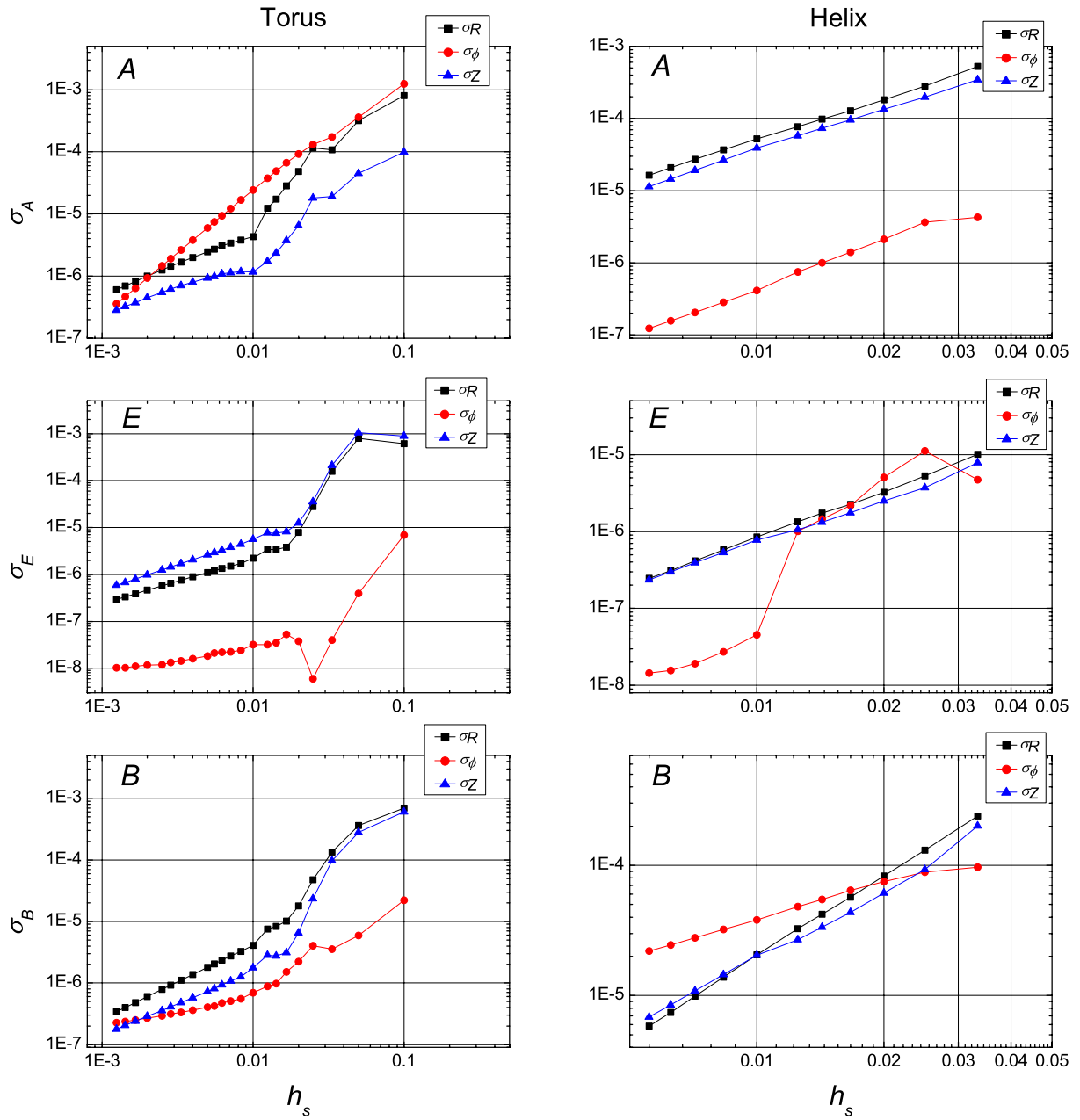


Figure 3.5. Unicity of the perturbed vector potential \vec{A} , the electric field \vec{E} and the magnetic field \vec{B} on the axis — convergence with the radial mesh size. Toroidal plane $\phi=0$.

The values involved in the calculation of the transformation matrix (3.29) come from the numerical equilibrium code and, unfortunately, are unavailable directly on the magnetic axis. To obtain (A_R, A_φ, A_Z) at $s = 0$, we use linear extrapolation using the values on the first two surfaces.

The unicity of the numerical solution can now be verified using the calculated values of $A_{R,\varphi,Z}(s = 0, \theta, \phi)$. We define a measure of the unicity error as a normalised variance

$$\sigma_k^2 = \frac{1}{\langle A_k A_k^* \rangle_{|s,\theta}} \frac{1}{2\pi} \int_0^{2\pi} |A_k - \langle A_k \rangle_{|\theta}|^2 d\theta \Big|_{s=0},$$

where k is any of the (R, φ, Z) components, $*$ stands for the complex conjugate and the notation $\langle \rangle_{|\theta}$ and $\langle \rangle_{|s,\theta}$ means averaging over θ and over the toroidal plane $\phi = const$ respectively.

Calculation results confirm the validity of the method used to assure the unicity on the axis. In Figure 3.5 the relative error is shown for different components of the vector potential and the perturbed fields as a function of the radial mesh step. The calculations are presented for two geometries: an axisymmetric torus with an aspect ratio $R/a = 3$ (left) and a 3D helix-like configuration with a large aspect ratio and a non-planar axis (right); the oscillation frequency is in the Alfvén continuum range. Note that only the grid for perturbation calculations is varied, but the equilibrium grid remains the same for this convergence study.

3.13 CPU time and memory requirements

Computational resources requirements is a very important factor to take into account for 3D calculations. The choice of the discretisation method usually depends not only on physical or mathematical considerations, but also on the computer resources available. For example, for our problem, a Fourier discretisation in all three directions could, potentially, be more advantageous, foreseeing the possible future extension of the plasma model to

the kinetic description. However, a full spectral representation produces very large dense matrices. In 3D geometry, this would require the use of a massively parallel computer with performance and memory size of a totally different level.

In the present work, the matrix size is reduced by using localised basis functions in the radial direction. This choice makes the matrix diagonally banded, and results in a linear scaling of the memory and CPU time needed for the matrix inversion with the radial mesh size. As for the spectral decomposition in the two remaining directions, the interpolating functions (exponentials) are non-zero on the whole calculation domain, so the coupling is not limited to the neighbouring elements only, and the matrix size and the CPU time scale quadratically with the number of modes in each direction. The matrix inversion is done by the standard LU factorization using subroutines from the NAG (Numerical Algorithms Group) library.

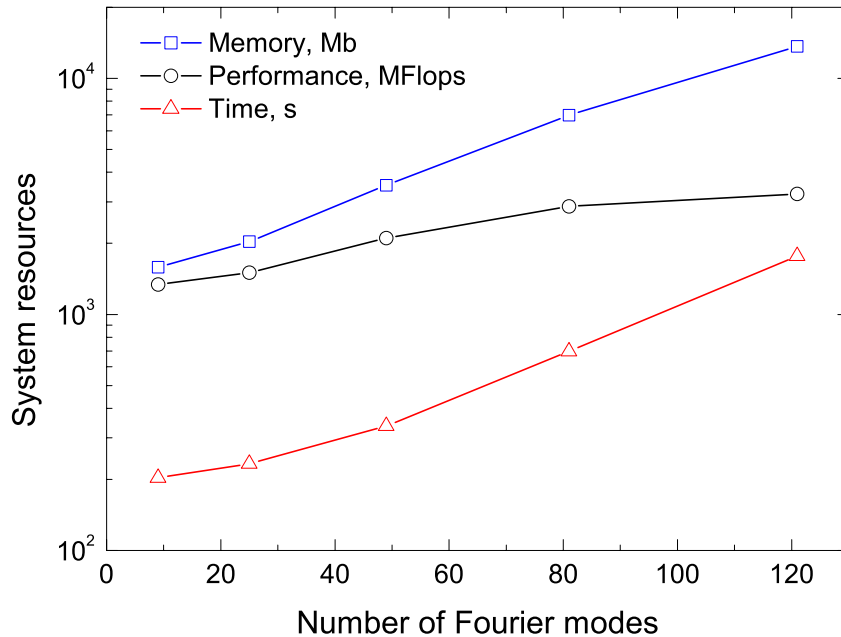


Figure 3.6. *System resources and performance scaling with the total number of perturbation harmonics for a typical 3D configuration. $N_s = 140$, Hermite cubics, one antenna frequency.*

An example of the resources required and the computational performance for a typical 3D stellarator geometry are shown in Figure 3.6 as a function of the total number of harmonics.

A considerable effort has been made to optimise the code for the vector processor architecture of the NEC SX5 computer, the main platform used for 3D calculations. Due to efficient loop structure, the degree of vectorisation reaches the values of 99.0–99.6%.

For a large number of harmonics, matrix inversion is the most time-consuming subroutine, the fast Fourier transform of the equilibrium and optimised matrix construction having slower scalings. The larger the size of the numerical problem, the closer is the scaling of the CPU time and memory to the maximum rate of N_{mn}^2 , where N_{mn} is the total number of Fourier harmonics, toroidal and poloidal modes combined. The performance of the code also increases with N_{mn} to reach, for typical 3D runs, 3.0–3.7 Gflops on a single NEC SX5 vector processor, which is not far from the maximum possible.

A typical run in the Alfvén range of frequencies for a fully 3D configuration is situated near the right side of Figure 3.6; it usually takes approximately 1000–3000 seconds (one antenna frequency) and requires 10-16 Gb of memory on the SX5 machine. 2D runs are usually one or even two orders of magnitude faster and smaller.

Chapter 4

Results

The numerical scheme applied to the physical model presented in the previous chapters has been implemented in the new code LEMan (**L**ow-frequency **E**lectro**M**agnetic **w**ave propagation). The code is designed to study small-amplitude perturbations of E/M fields in 3D plasmas induced by an external antenna in the Alfvén and ion-cyclotron range of frequencies. In this chapter, we present results of these studies for different configurations and benchmarks against analytical solutions or other numerical simulations, whenever it is possible.

Before applying the newly developed code to a realistic 3D stellarator, we have to be certain that it produces correct results for simpler configurations, where the solution can be found by other means. Also, some effects are intrinsic to the physical model and are not a particular feature of a specific geometry. In such cases, simple geometries are more suitable for presentation because they make the analysis much easier and clearer, including the visualisation of the results. Otherwise, in a 3D configuration, information about the underlying physics of the process can easily be lost behind the effects of complicated geometry. For these reasons, we have tried to keep the geometries as simple as possible, progressing gradually to more complicated configurations, still comparing them to their simpler analogues.

We will try to follow the same order of presentation of the results. In the first section, the code will be tested in the very simple limit of the one-dimensional cylindrical geometry,

with and without plasma. Different modes will be discussed, including eigenmodes of a cylindrical waveguide, Alfvén resonant modes (global and local), fast magnetosonic waves.

The second section is dedicated to the more complicated systems still retaining important symmetries. These include a cylinder with non-circular cross-section, toroidal and mirror geometries. The symmetry breaking even in one direction has very important consequences for the qualitative picture of the mode structure because of the coupling that is absent for a 1D cylinder.

Finally, some results for simplified (helix) and fully 3D (QAS, LHD) configurations are presented. A detailed study is much complicated by the effect of non-symmetric equilibrium terms and the arising coupling between the modes, but even for such 3D geometries some parallels can be drawn with their simple cylindrical analogues.

4.1 1D cylindrical geometry

A simple one-dimensional cylindrical geometry provides a very convenient case for various tests of the newly developed code. The result analysis in a cylinder is simplified by the symmetry in both poloidal and toroidal (or, azimuthal and axial) directions, and, therefore, the absence of coupling between different perturbation harmonics. In many cases, the 1D solution of the wave equation can be found analytically or semi-analytically, which makes possible a direct comparison with the numerical results and provides a good basis for convergence studies.

4.1.1 Cylindrical vacuum waveguide

The first and simplest possible limit to test the validity of the numerical scheme of the newly developed code and to study some of its convergence properties is the vacuum waveguide with a circular cross-section.

The solution of the wave equation in this case is well known and the characteristic modes and their respective frequencies can easily be found analytically [57]. The wavefields of the corresponding homogeneous problem are given by the Bessel functions $J_m(k_r r)$ radially and by harmonic functions in the azimuthal and axial directions. Combined with the boundary conditions, the wave equation specifies a classical eigenvalue problem for the waveguide oscillations.

There exist two distinct types of solutions. These two modes have different polarizations and can be excited separately. The first one, called the *transverse electric wave* (TE), has zero axial component of the perturbed electric field. For the second one, the *transverse magnetic wave* (TM), the magnetic field axial component vanishes everywhere. For given axial and azimuthal wavelengths of the perturbation, the eigenfrequencies of the TE and TM modes are different; they are related through the dispersion relation to the zeros of the Bessel functions $J_m(k_r r)$ for the TM modes and zeros of their radial derivatives for the TE oscillations. The modes are usually labelled $TE/TM_{r m n}$ according to their radial r , azimuthal m and axial n mode numbers. We will restrict the results

shown here to zero axial wave vector component, $n = 0$, and drop the last index for brevity. The solution is identical for positive and negative m , so we will only consider $m \geq 0$ here¹.

The global code presented here is designed to calculate the response of the medium to an external excitation with a prescribed time-dependence (frequency) and spatial structure (axial and azimuthal mode numbers). Therefore, it does not directly obtain the eigenvalues of the problem, but finds the stationary solution of the initial value problem for the same system instead. However, it can be used to search for the eigenfrequencies by performing a scan in frequencies of the external source. This approach requires to define a response function of the system. In a realistic waveguide it could be, for example, the amplitude of oscillations or power losses. In our idealised model, we do not have physical energy losses in the system, but we can simulate it by introducing a small imaginary part $i\nu$ in the frequency. This imaginary part, at the same time, serves to regularize the equations as to avoid the singularity at the eigenfrequency of the system and to allow the numerical resolution. Otherwise, even for a finite excitation at the eigenfrequency, the amplitude of the oscillations goes to infinity in a loss-free system. The response of the system is thus defined as the imaginary part of the power integral P_{pla} in Eq.(3.27), even though here it does not have the same meaning of the absorbed power because no physically relevant mechanism of energy losses is defined. In a scan over frequencies, the response is composed of a set of discrete maxima, corresponding to the eigenmodes of the system. The width of a maxima is proportional to the arbitrary parameter ν , its height is inversely proportional to it. In the limit $\nu \rightarrow 0$ the frequency of the peak is equal to the eigenfrequency of the discretised set of equations.

We have applied this approach to search for the frequencies of the TE and TM modes in a cylindrical waveguide. One natural way to represent a cylinder in a code based on a closed toroidal topology is to increase the aspect ratio to the value where the poloidally

¹Note that for a numerical metric of toroidal geometry with large but finite aspect ratio and small poloidal magnetic field the degeneracy of modes $\pm m$ is removed (in the numerical solution) because the two directions of polarization are no longer equivalent.

(azimuthally) non-symmetric terms in the equilibrium² are negligible. However, to avoid the errors originating from the numerical nature of the underlying equilibrium we use the analytical expressions for the metric coefficients, completely excluding the toroidal terms and the associated coupling. This approach guarantees that the calculation errors are restricted to the finite element discretisation of the wave equation, i.e. the very part of the code that we intend to study the convergence properties of.

For simplicity, we have set the waveguide radius to $a = 4.77$ cm, which makes the eigenfrequencies in GHz to be exactly equal to the roots of the corresponding Bessel functions. A frequency scan of the response of the system in a very wide range of frequencies from 1 Hz with resolution $df/f < 1\%$ is a monotonic function up to the first *TE* or *TM* modes in the gigahertz range. The scans made for different azimuthal modes and different radial grid sizes do not reveal any unphysical solutions even for very low numerical resolutions ($N_s = 5$) and so confirm that the scheme is pollution-free. An example of the frequency scan for an excitation with $m = 3$ and $k_z = 0$ is shown in Figure 4.1.

Every peak on the frequency scan is associated with a corresponding *TE* or *TM* mode, no spurious solutions are present even for very low numerical resolution. Results of several similar scans for other azimuthal mode numbers and two different sets of radial basis functions are summarized in Figure 4.2.

These results are obtained with low numerical resolution (10 radial elements) with linear and cubic interpolating functions. As expected, cubic polynomials provide a much better approximation than the linear "hat" functions. Linear elements describe the solution well for lower order modes, but pushing the scheme to the very low resolution of < 2 nodes per "radial half-wavelength" (higher-order radial modes in Figure 4.2) results in a visible difference in the eigenfrequency. This is only valid for radial modes, the higher-order azimuthal (and axial) modes do not suffer from the same lack of precision due to the harmonic representation of the numerical solution that allows for the exact matching of the analytical azimuthal (and axial) dependence.

²The term "equilibrium" is, of course, meaningless in the absence of plasma, but we still use it here for convenience.

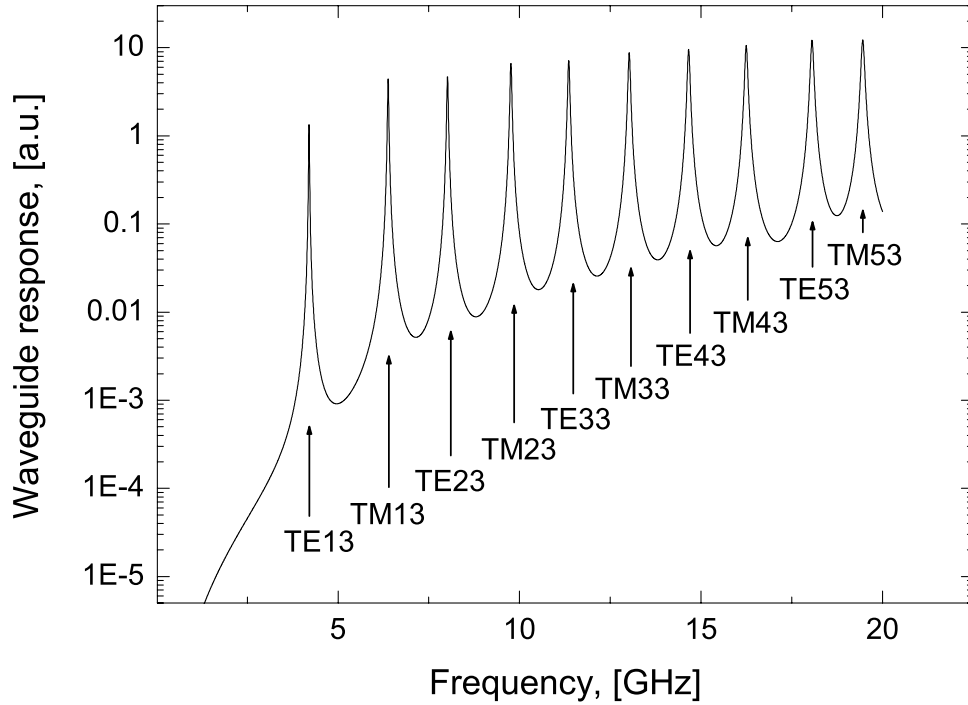


Figure 4.1. *Response as a function of frequency in a cylindrical waveguide, $m = 3$ antenna. Cubic finite elements, $N_s = 10$, $\nu = 5 \cdot 10^{-3}$.*

The convergence of the results for different types of basis functions deserves a closer look, so let us discuss it in more detail.

4.1.2 Radial convergence and finite elements

A 1D cylindrical geometry is a very convenient case to study the convergence properties of the finite elements implemented in the code for several reasons. First, the analytical solution of the propagation problem is well known and allows for a direct comparison. Then, the underlying "equilibrium" metric coefficients involved in the wave equation are easily obtained analytically, so this source of numerical error is eliminated. Finally, simple cylindrical geometry forbids the coupling between the modes and the numerical solution is, in some sense, "completely converged" in the azimuthal and axial directions due to the Fourier representation, so the only errors come from the radial discretisation.

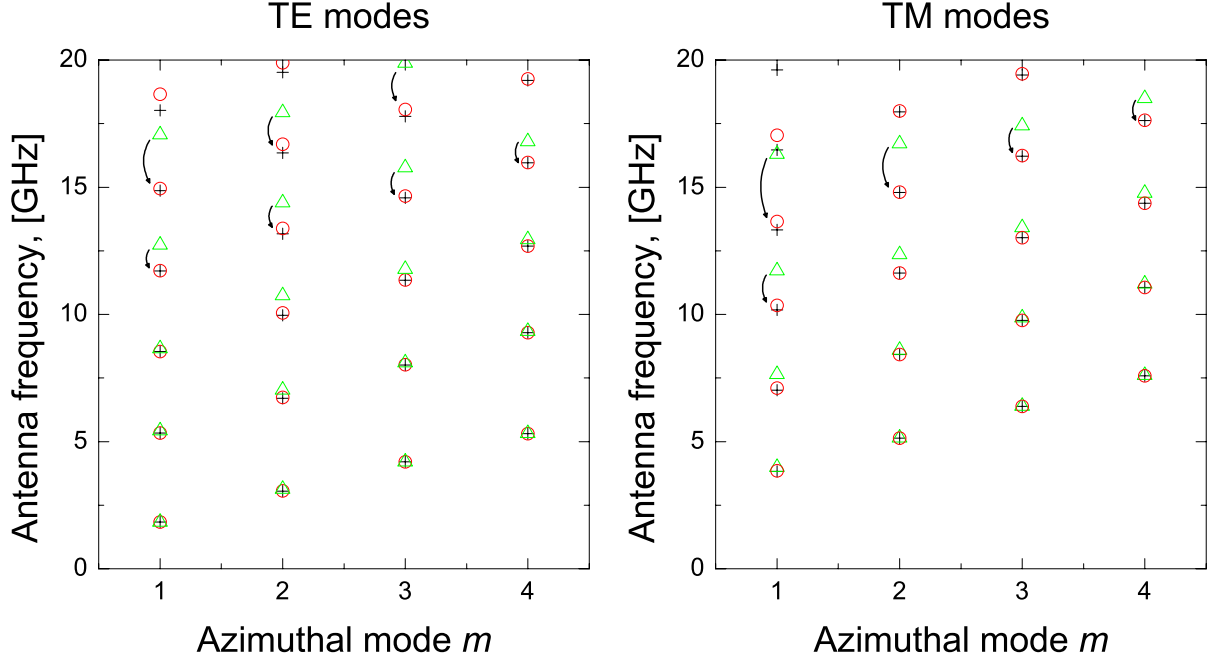


Figure 4.2. *TE and TM modes of a cylindrical vacuum waveguide. Crosses — exact analytical frequencies, circles and triangles — numerical approximations with cubic and linear finite elements correspondingly ($N_s = 10$).*

Here, we define the measure of convergence as a relative error in the eigenfrequency of *TE* and *TM* modes $\delta = (f - f_{exact})/f_{exact}$. Several scans were performed for different number of radial elements using linear "hat" basis functions and Hermite cubics (Figure 4.3).

As expected from the order of approximation, standard linear basis functions result in a quadratic convergence for most of the modes. However, some of the modes, namely TE_{10} , TE_{12} and TM_{11} converge only linearly with radial mesh step h . The reason lies in the type of radial asymptotics of the wavefields of these modes near the axis. These asymptotics can easily be obtained near the axis by projecting the wave equation (2.21) onto a cylindrical basis $(\vec{e}_r, \vec{e}_\theta, \vec{e}_z)$. Looking for the solution in the form $A_k(r, \theta, z) = A_k r^{\alpha_k} e^{i(m\theta + k_z z)}$ and keeping only the leading terms in r^{α_k} , we get the following simple system of equations in the limit $r \rightarrow 0$:

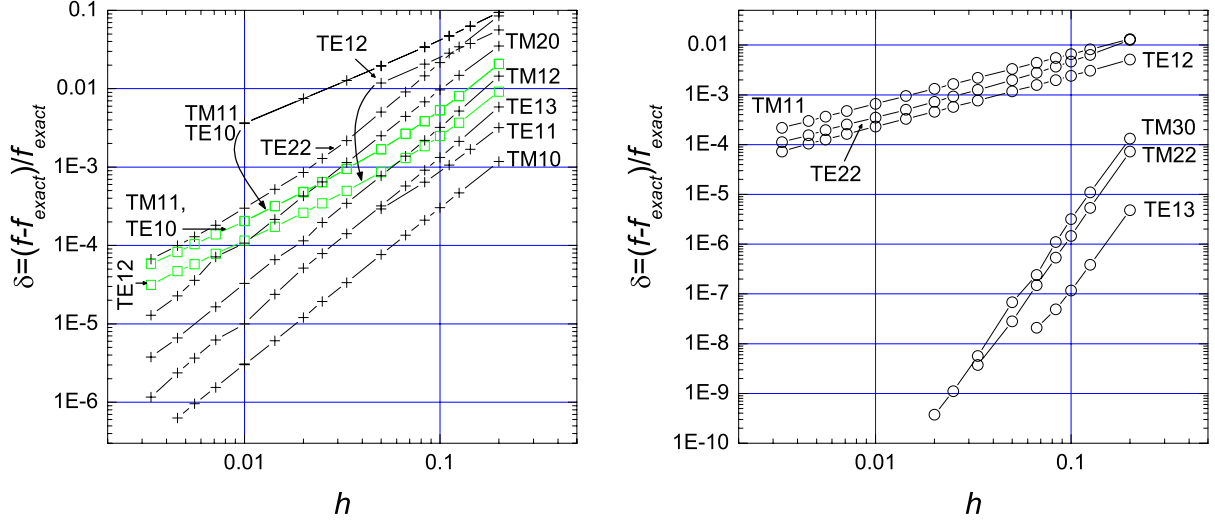


Figure 4.3. *Relative error of the eigenfrequency versus the radial step size (equidistant in s grid). **Left:** linear FE (crosses mark the calculations made with standard "hat" functions, squares — with a modified element near the axis), **Right:** cubic FE.*

$$\begin{cases} (\alpha_r^2 - m^2 - 1) r^{\alpha_r} A_r - 2imr^{\alpha_\theta} A_\theta = 0 \\ (\alpha_\theta^2 - m^2 - 1) r^{\alpha_\theta} A_\theta + 2imr^{\alpha_r} A_r = 0 \\ (\alpha_z^2 - m^2) r^{\alpha_z} A_z = 0 \\ (\alpha_\phi^2 - m^2) r^{\alpha_\phi} \tilde{\phi} = 0 \end{cases}$$

(even though $\tilde{\phi}$ is zero in a vacuum waveguide, we retain it here for generality).

The last two equations immediately yield the asymptotics for the axial component of \vec{A} and the scalar potential: $A_z \sim \tilde{\phi} \sim r^{|m|}$. The first two equations are compatible at $r \rightarrow 0$ only if A_r and A_θ have the same asymptotics: $\alpha_r = \alpha_\theta$. In this case, a non-trivial solution exists if the determinant of the system is zero: $(\alpha^2 - m^2 - 1)^2 - 4m^2 = 0$, so we obtain the leading asymptotics $A_r \sim A_\theta \sim r^{|m|-1}$.

For the transverse magnetic mode, the radial and azimuthal components of \vec{A} are zero and the behaviour of the mode is defined by the axial component A_z . The *TM* modes with slow convergence have the azimuthal number $m = 1$, so, close to the axis, A_z is proportional to the radius r . Now, remembering that the radial variable used in

the code is not r , but s which is proportional to the volume near the axis, the cause of the problem becomes clear. $s \sim r^2$, so, at small s , A_z and $\tilde{\phi}$ behave as \sqrt{s} , therefore the radial derivative d/ds of the exact solution becomes infinite! Naturally, this is very unfortunate for the numerical application. Trying to approximate a function with a singularity by piecewise-constant elements is not an optimal choice, which results in a very slow convergence. Exactly the same happens with the TE_{10} and TE_{12} modes. The wavefields of a TE mode are defined by the radial and azimuthal components of \vec{A} . Hence, for $m = 0, 2$, we obtain the same asymptotics $A_r \sim A_\theta \sim r \sim \sqrt{s}$, with the same negative impact on the convergence properties (Figure 4.3, left).

One of the possible ways to resolve this problem is to use basis functions that can best represent the exact solution. Redefining the functions on only one first radial element indeed helps to greatly improve the convergence. We have replaced one linear basis function with \sqrt{s} for those components and azimuthal harmonics that have this asymptotic as schematically shown in Figure 4.4.

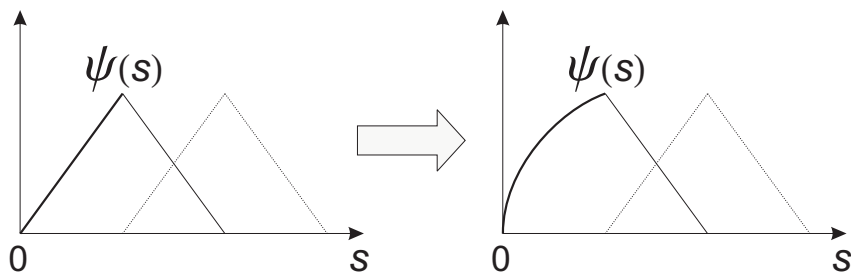


Figure 4.4. *Modification of the standard linear finite elements ("hat" functions) to match the radial behaviour of the exact solution.*

The convergence results with these modified linear FE are shown in Figure 4.3 (left) with square markers. This small modification of the basis functions helps to achieve a nearly quadratic convergence in h , almost as good as for the other modes with no singularities, and even better for some modes at the low resolution. With higher number of mesh points, the relative contribution of the first radial element in the matrix becomes smaller, so the convergence somewhat slows down.

The drawback of this simple method is that it can be easily implemented only in 1D geometry. Unfortunately, for a 2D and, even worse, for a 3D geometry, the coupling of the modes substantially complicates the above considerations. The coupling mixes the asymptotics of different harmonics and components, so choosing the appropriate basis function for each one is hardly possible. In this case, a way to work around this problem could be to include both sets of basis functions (both with singular and constant derivatives near the axis) simultaneously. This way, the numerical solution is "free to choose" from the best match among the basis functions and adapts the coefficients automatically. We have tested this approach as well, and the results were, as expected, very similar to the modified FE described above. This method would work for more complicated geometries, but at the expense of technical complications. Including more than two basis functions on only the first radial element, we lose the very desirable property of the matrix — it is no longer tridiagonal. It is probably still possible to avoid it by introducing new variables and redefining the indexing, further complicating the problem, but, as we will see, there are other ways to obtain the desired precision, and the radial convergence is not the limiting factor, so we do not proceed further in this direction.

An approximation with cubic elements is, in general, much more precise than that with the linear FE. If no special care is taken to treat the axis region, it still suffers from the same problem with singular derivatives in the origin, as can be seen from the Figure 4.3 (right). However, even for these modes, the error values are about an order of magnitude lower than those obtained with the standard linear FE. For all the other modes, the convergence with Hermite cubics is excellent. The relative error in frequency decreases faster than h^5 , reaching the orders of $10^{-7} - 10^{-6}$ at about ten points per wavelength.

Another way to improve convergence of the modes with singular radial derivatives in the origin is simply to use grids with accumulation of points towards the axis. This method is much easier to implement, it does not involve any modification of the code itself, and is applicable in any geometry. As an example, we show the results obtained with several types of radial non-equidistant in s grids with different rates of accumulation towards the origin (Figure 4.5).

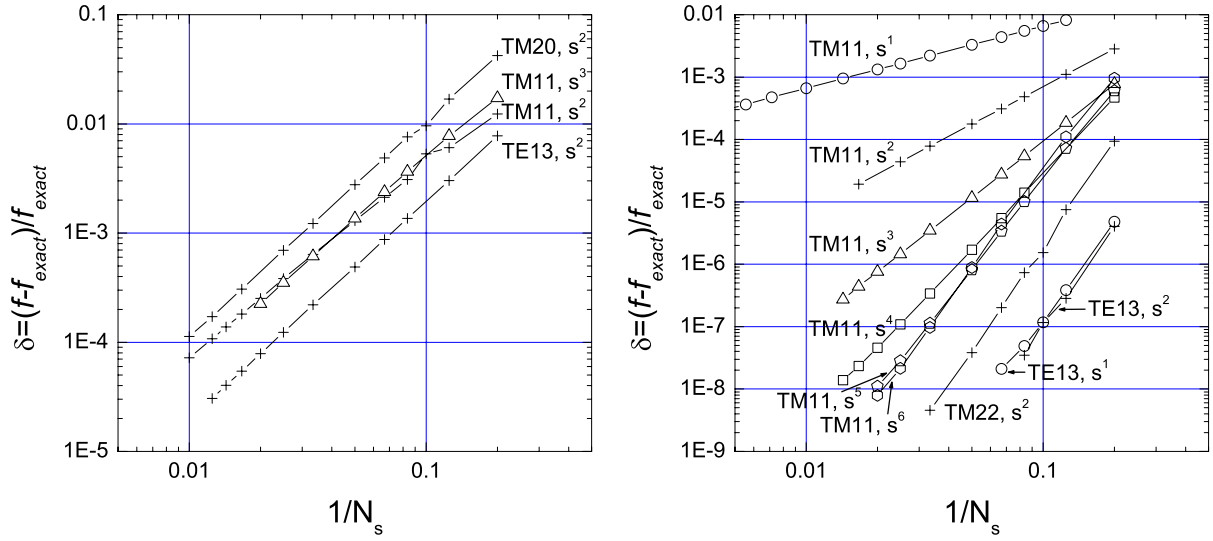


Figure 4.5. *Relative error of the eigenfrequency versus the inverse of the number of radial mesh points for grids with node accumulation near the axis. Left: linear FE, Right: cubic FE. On both plots: crosses – grid with quadratic accumulation of points towards the origin, triangles – cubic accumulation s^3 , squares – accumulation s^4 , pentagons – s^5 , hexagons – s^6 , circles – equidistant (in s) grid.*

For linear FE (with modified first element as explained above), the rate of convergence remains quadratic for any type of radial grid, with accumulation or not, and for any mode (left graph). This is to be expected, because the quadratic rate is the maximum speed of convergence for this order of approximation. It is not defined by the axis region, but by the whole domain of calculations. So, dense grid near the axis can only affect the absolute value of the error, but not the rate.

The situation is different for the cubic basis functions. Increasing the rate of point accumulation near the axis improves the convergence of problematic modes, until it reaches the maximum rate of $\sim 1/N_s^5$, similar to all other modes (Figure 4.5, right). Beyond that, again, the rate is defined by the whole domain, so the axis is no longer the limiting factor. For the modes with no singularities in the origin, the type of grid does not considerably affect the rate of convergence (see modes TE_{13} , TM_{22} on Figure 4.5, right).

Let us briefly summarize the discussion of the convergence results. Cubic elements require more space to store the matrix and more time to resolve it compared to linear FE, but this is more than compensated by a much faster convergence. So, in general, cubic elements are more advantageous since they provide the solution with a required precision using less computational resources than the linear FE. Unless stated otherwise, the results presented in this work are obtained with cubic FE. Special care should be taken to treat the axis region. A modification of basis functions to match the asymptotics of the exact solution or using grids with node accumulation near the origin helps to accelerate the convergence. With the improved radial convergence, the error limit is often imposed by the azimuthal and axial (or, poloidal and toroidal) discretisation, which will be discussed later.

4.1.3 Homogeneous cylindrical plasma column

Introducing plasma in a cylinder as discussed above leads to new types of propagating modes, namely Alfvén and fast magnetosonic waves. Once again, the 1D geometry allows for an analytical (or semi-analytical) solution with a certain simplification of the model, which makes possible a direct comparison and validation of the code.

We will first consider a very simple configuration of a cylindrical currentless plasma column of constant density immersed in a homogeneous magnetic field surrounded by a vacuum region and a conducting shell. A detailed study of the oscillation spectrum of this configuration is presented in Ref. [58]. We will use this paper as a reference and reproduce the analytical results by means of the new global code with a slightly more complicated plasma model.

The equation governing small-amplitude oscillations in a homogeneous plasma column can be obtained analytically by developing the wave equation (2.16) in cylindrical coordinates and combining it with the boundary conditions as shown in [58]. In this study, the derivation is done for a simplified cold plasma model, neglecting the finite-electron mass effects so that $E_{\parallel} = 0$ and assuming $c/c_A \gg 1$. The resulting equation, that we do not

show here, can have a non-trivial solution only if the corresponding dispersion relation is satisfied. For given azimuthal and axial wavenumbers zeros of the dispersion relation indicate the possible oscillation modes and their frequencies. The dispersion relation in this case is expressed as a combination of Bessel functions. Its roots can be obtained analytically only in certain limits (for example, in the ideal MHD limit $\omega/\Omega_i \rightarrow 0$, or for $k_z a \rightarrow 0$). Numerically, the zeros of the analytical dispersion relation can be easily found, that is why this solution can be called "semi-analytical".

Following this approach, it has been shown previously that global modes of this system in the cold plasma approximation are divided into two classes: eigenmodes of the fast magnetosonic wave and of the Alfvén wave. The frequency spectrum of the configuration is presented in Figure 4.6 as a function of the axial wavenumber k_z for the azimuthal modes $m = \pm 1$. k_z here is normalised to the inverse minor radius $1/a$. The plasma parameters are close to the typical values of the TCA experiment [59]: hydrogen plasma density $n = 0.52 \times 10^{19} \text{ m}^{-3}$, plasma radius $a = 0.2 \text{ m}$, radius of the conducting shell $r_w = 0.3 \text{ m}$, background axial magnetic field $B = 1.0 \text{ T}$.

The frequency of the Alfvén modes is limited by the cyclotron frequency of the ions, whereas the fast mode can propagate both below and above Ω_i . At $\omega \ll \Omega_i$ we recover the ideal MHD limit, so the frequencies of the modes with $m \pm 1$ polarizations are nearly identical. For higher frequencies the finite ω/Ω_i corrections start to play a role and the ion gyration direction removes the degeneracy between the two polarizations.

Calculations with the global code reproduce numerically all of these modes with a very good precision (Figure 4.6, square and circle symbols). Finite electron mass does not change considerably the frequency of the modes. For these calculations, we again used the analytical cylindrical metric to avoid the errors due to the equilibrium discretisation. Results obtained with a numerical toroidal equilibrium with large aspect ratio change the eigenfrequency by a value inversely proportional to the aspect ratio.

The modes obtained by the two methods, the analytical solution of the eigenvalue problem and the frequency scan of the plasma response in the global code, are in a one-to-one correspondence. No spurious solutions are introduced, which validates the

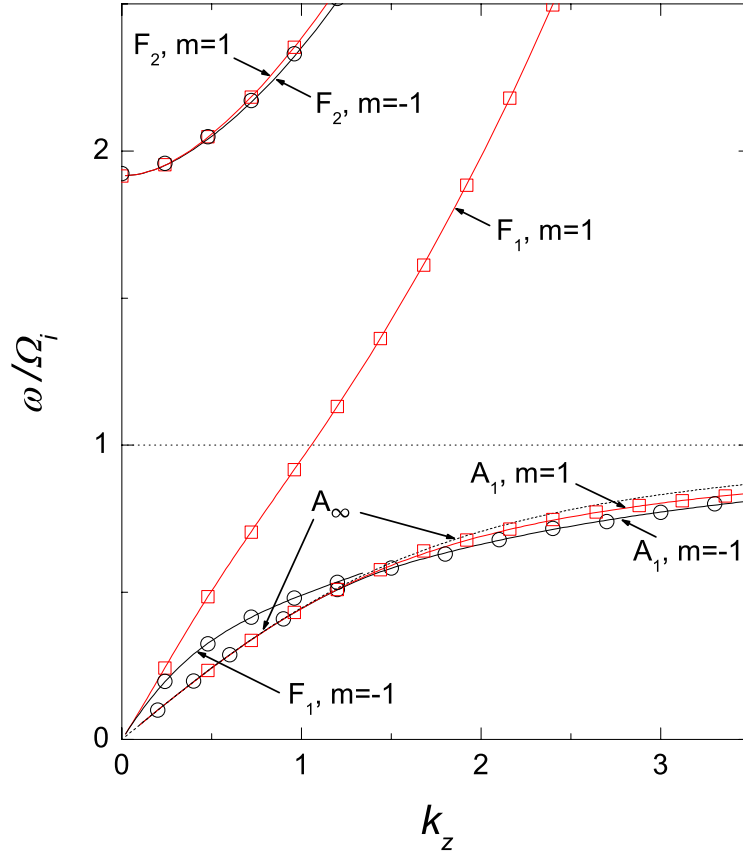


Figure 4.6. *Oscillation spectrum of a currentless plasma cylinder with constant density immersed in a homogeneous axial magnetic field. Solid and dashed lines correspond to analytical results [58], squares ($m = 1$) and circles ($m = -1$) correspond to calculations with the global code. \mathbf{F} and \mathbf{A} denote global eigenmodes of the fast magnetosonic and Alfvén waves. Only the lowest radial modes of the Alfvén wave are shown.*

discretisation scheme now in the presence of a plasma. An illustration is presented in the Figure 4.7 for a set of radial eigenmodes with $m = -1$ and $k_z a = 3$.

On the top graph, the analytical dispersion relation is plotted as a function of the normalised (to Ω_i) frequency. For fixed azimuthal and axial wavenumbers, a zero of the dispersion relation defines the frequency of the global eigenmode and the corresponding radial wavenumber k_r . The roots on the left part of the plot correspond to the different radial eigenmodes of the Alfvén wave. There is an infinite number of them, all lying between the lowest mode at $\omega \approx 0.77 \Omega_i$ and the maximum frequency of $\omega \approx 0.832 \Omega_i$

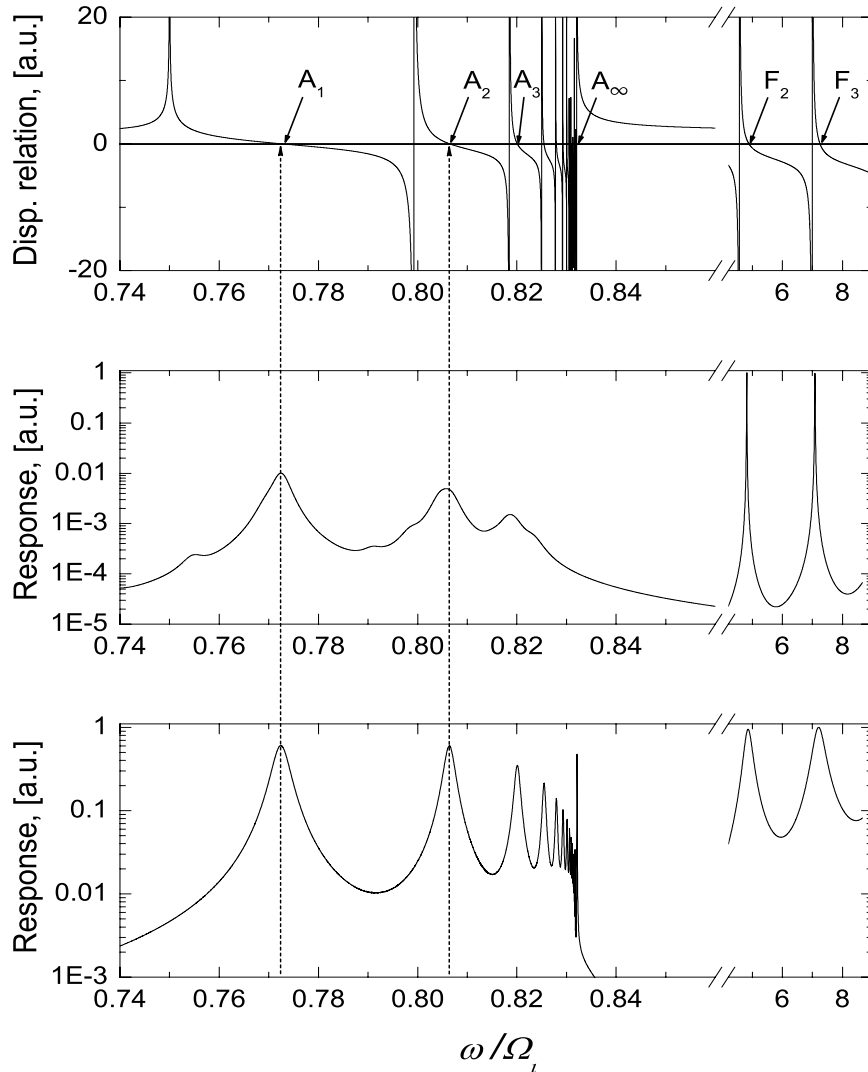


Figure 4.7. **Top:** Analytical dispersion relation as a function of normalised frequency for a homogeneous plasma cylinder, $m = -1$, $k_2 a = 3$. Zeros of this function define the global eigenmodes of the system. **Middle:** Frequency scan of the plasma response (normalised), full cold plasma model with an imaginary part in the frequency ($\nu = 10^{-2}$), **Bottom:** Normalised response obtained with a simplified plasma model without mode conversion to the QES wave.

which represents the accumulation point for the Alfvén wave for the parameters chosen. The roots above the ion cyclotron frequency are the fast wave solutions of the propagation problem.

To obtain the same modes with the global code, we proceed in much the same way as we did for the cylindrical waveguide. Now, the response of the system is defined as the total power absorbed in the plasma, or coupled in the antenna. The dispersion function appears in the denominator of the response of the system to an external excitation, so zeros of the dispersion relation show up as peaks in the plasma response. Frequency scans of the plasma response have been performed for two models of plasma. The first one is the usual full cold plasma description with a small imaginary part in the frequency ($\nu^0 = 10^{-2}$) as introduced in the section 2.5 (henceforth, we will omit the ⁰ superscript for the dimensionless notation of ν). The response (Figure 4.7, middle plot) is clearly peaked at the frequencies of the first three radial Alfvén modes and of the fast wave modes. Other maxima are smoothed out by the rather large value of ν . The additional very small peaks between the main eigenmodes appear due to the conversion to the short-wavelength quasi-electrostatic wave, not present in the model used for the analytical solution. It is possible to obtain a clear response without the mode conversion even with the code with all three components of the electric field. As proposed in [50], the full cold plasma model can be simplified by assuming $\omega \ll \nu$ and modifying the electron contribution in the dielectric tensor parallel term as follows:

$$-\frac{\Pi_e^2}{\omega(\omega + i\nu)} \quad \rightarrow \quad \frac{i\Pi_e^2}{\omega\nu} \quad (4.1)$$

Mathematically, this removes one of the positive solutions of the equation (2.33). This is easy to see if we explicitly write down the coefficients of (2.33):

$$an_{\perp}^4 + bn_{\perp}^2 + c = 0, \quad (4.2)$$

with $a = S$, $b = D^2 - (S + P)(S - n_{\parallel}^2)$ and $c = P((S - n_{\parallel}^2)^2 - D^2)$. Due to the large m_i/m_e ratio, the term P dominates in the coefficients of Eq.(4.2). Substitution (4.1) makes P almost purely imaginary, so P^2 becomes negative. At the Alfvén frequencies, this also turns the determinant of the equation (4.2) to a negative value. Thus, the propagation of the quasi-electrostatic wave is no longer possible in this model. The plasma response obtained for this approximation is shown in the bottom plot of Figure 4.7. All the peaks correspond to the roots of the analytical solution, no spurious modes are introduced.

In the case of a diffuse density profile, or in the presence of an equilibrium current in the cylinder, the oscillation spectrum changes significantly. This situation is discussed in the next section.

4.1.4 Non-homogeneous plasma cylinder with current

Let us now consider a non-homogeneous plasma column with a monotonically decreasing density, surrounded by a vacuum region. The equilibrium magnetic field now has both an axial (externally induced) component and an azimuthal component generated by a plasma current. This configuration is of particular interest because of its similarity to a typical toroidally confined plasma. It can be approximated as a large aspect ratio torus with a circular cross-section. Even though it does not possess the full variety of modes produced by the non-symmetric terms in the equilibrium, it still represents a good starting point.

The main difference of this configuration from the homogeneous plasma discussed above is the presence of the so-called "Alfvén continuum" part in the frequency spectrum. At very low frequencies $\omega \ll \Omega_i$ and in the limit $m_e/m_i \rightarrow 0$ the Alfvén wave solution of the dispersion relation takes the well known ideal MHD form

$$\omega^2 = c_A^2 k_{\parallel}^2. \quad (4.3)$$

This equation defines the Alfvén resonance, where, in the model with $E_{\parallel} = 0$ and zero resistivity, the wavefields have a singularity. In a non-homogeneous cylindrical plasma, c_A and k_{\parallel} are continuous functions of the radial direction. If the condition (4.3) is satisfied somewhere in the plasma, a small change in frequency displaces the radial position of the resonance, but does not qualitatively change the character of the singularity. Unlike the discrete eigenmodes in the previous section, the solution of Eq.(4.3) can be found in a continuous interval of excitation frequencies, this interval thus is known as a "continuum" part of the spectrum.

This description holds for a model with zero electron mass. If, however, finite m_e is taken into account, the Alfvén resonances constitute mode conversion points to generate the quasi-electrostatic wave and formally the spectrum is entirely discrete. In this work,

we will still refer to the Alfvén "continuum" by analogy with the model that assumes $E_{\parallel} = 0$. If the imaginary part in the frequency is large enough to damp the QEW before it reaches another resonance or the plasma edge and forms a standing wave, the plasma response is continuous even in the full cold plasma model. The conversion to the QEW and its eigenmodes are discussed in more detail in the sections 4.2.4, 4.2.5.

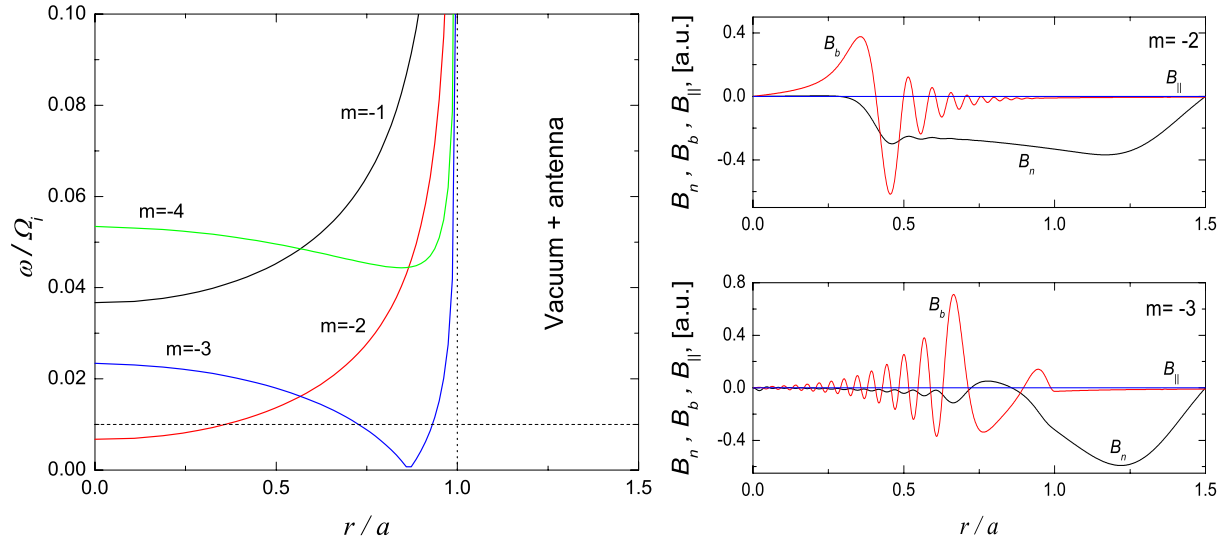


Figure 4.8. **Left:** Alfvén continuum branches in a non-homogeneous plasma cylinder with equilibrium current, $k_z a = 0.13$. **Right:** Normalised perturbed wavefields (real part) at the frequency $\omega/\Omega_i = 0.01$ for two azimuthal modes: $m = -2$ and $m = -3$.

Figure 4.8 (left) shows a typical structure of Alfvén continuum branches in a non-homogeneous plasma cylinder. The frequency of the Alfvén wave (4.3) is plotted versus the radial position of the resonance for different azimuthal harmonics. The plasma parameters used here are the same as described in the previous section, but this time the plasma has a parabolic density profile $n = n_0 (1 - (r/a)^2)$ and a non-zero azimuthal component of the static magnetic field such as to create a monotonic ι profile. For these calculations, we use a numerical equilibrium of toroidal geometry with large aspect ratio ($R/r_w = 10^3$). The ι values are therefore very large, to make the azimuthal magnetic field comparable to the axial component. Here, ι decreases parabolically from 90 on the axis to 58.5 at the plasma-vacuum interface.

In the plasma core, the behaviour of the modes is mainly determined by the parallel wavevector $k_{\parallel} = k_z + \nu m/R$. Near the plasma edge, the Alfvén velocity c_A rapidly increases because of lower density. The Alfvén frequency rises as well (but it is still limited from above by Ω_i !), therefore at higher frequencies the plasma edge is usually an accumulation point for local Alfvén resonances.

On the right of Figure 4.8, the perturbed magnetic field is shown for azimuthal modes $m = -2$ and $m = -3$ at $\omega/\Omega_i = 0.01$. As mentioned above, the Alfvén resonance represents a point of mode conversion to the short wavelength oscillations (QEW) that, in the cold plasma model, propagate in the direction defined by the sign of the radial derivative of $c_A(r)k_{\parallel}(r)$. This propagating wave is gradually damped by the imaginary part ν in the frequency ($\nu = 5 \times 10^{-2}$). As expected for a shear wave, the parallel component of the perturbed \vec{B} is negligible compared to its normal and binormal counterparts.

In the presence of the Alfvén resonance in a plasma described by the model (2.29), the energy is mostly absorbed by the converted QES wave damping. Figure 4.9 (left) shows the cumulative integral of the resistive power as defined in Eq.(3.27), calculated for two different values of ν . The plasma parameters are the same as for the case of

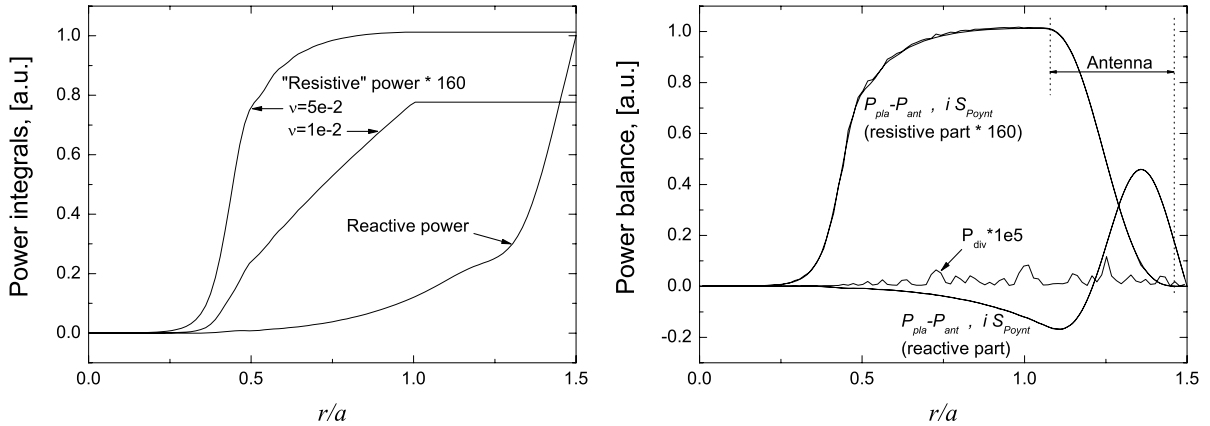


Figure 4.9. **Left:** Cumulative power integral for the case of the Figure 4.8 (right, $m = -2$). **Right:** Power balance on each radial surface for the same case ($\nu = 5 \times 10^{-2}$); P_{div} is the contribution of terms with $\nabla \cdot \vec{A}$ in the equation (3.1).

Figure 4.8, $m = -2$. The Alfvén resonance occurs at the radial position $r/a \approx 0.36$, the converted wave propagates outwards. For a stronger damping parameter ($\nu = 5 \times 10^{-2}$) the wave is absorbed closer to the point of conversion than for $\nu = 1 \times 10^{-2}$.

The power balance (3.27) is used for the self-consistency check of the results (Figure 4.9, right)³. Both the reactive and the resistive parts of the power balance are well satisfied. For the reactive part, the difference between the two functions is almost indistinguishable in this scale (the error is less than 0.15% for any radial surface, $N_s = 100$). The contribution of the term $\vec{F}^*(\nabla \cdot \vec{A})$ in the integral (3.1) (marked P_{div} on the plot) is several orders of magnitude lower than the physical energy integrals P_{pla} , P_{ant} and Poynting flux S_{Poynt} ; the contribution of the $(\nabla \cdot \vec{F}^*)(\nabla \cdot \vec{A})$ is smaller by another two orders. So, the Coulomb gauge is well satisfied and the contribution of the residual terms with $\nabla \cdot \vec{A}$ in the power integrals is negligible.

To conclude the discussion about the power balance and convergence in the presence of plasma, the power integrals are calculated with a different number of radial elements and azimuthal harmonics (Figure 4.10). Even though the geometry is essentially 1D, the equilibrium still has non-symmetric terms due to finite toroidicity ($R/r_w = 10^3$). For high radial precision, the contribution of these toroidal terms in the error (of the power balance, or of the Coulomb gauge) becomes comparable to the error of the radial discretisation. Increasing the number of azimuthal modes N_m included in the calculations helps to decrease the relative error (Figure 4.10, *b* and *c*), but it is still limited by the smoothness of the underlying numerical equilibrium. Similarly, the convergence with N_m , exponential for small N_m , rapidly saturates at larger N_m (plot *d*) because of the finite radial discretisation and equilibrium precision.

The continuum Alfvén modes discussed above are *local* resonances satisfying the local dispersion relation (2.37) at some radial position. There exists another class of solutions,

³Here, we rearranged the terms to group P_{pla} and P_{ant} together, because they are both defined in the integer radial mesh points, whereas the surface integral S_{Poynt} is defined on half-mesh points. The error of the power balance is usually so small that the interpolation from half-mesh to integer mesh can introduce an error comparable or even larger than the actual discrepancy in powers.

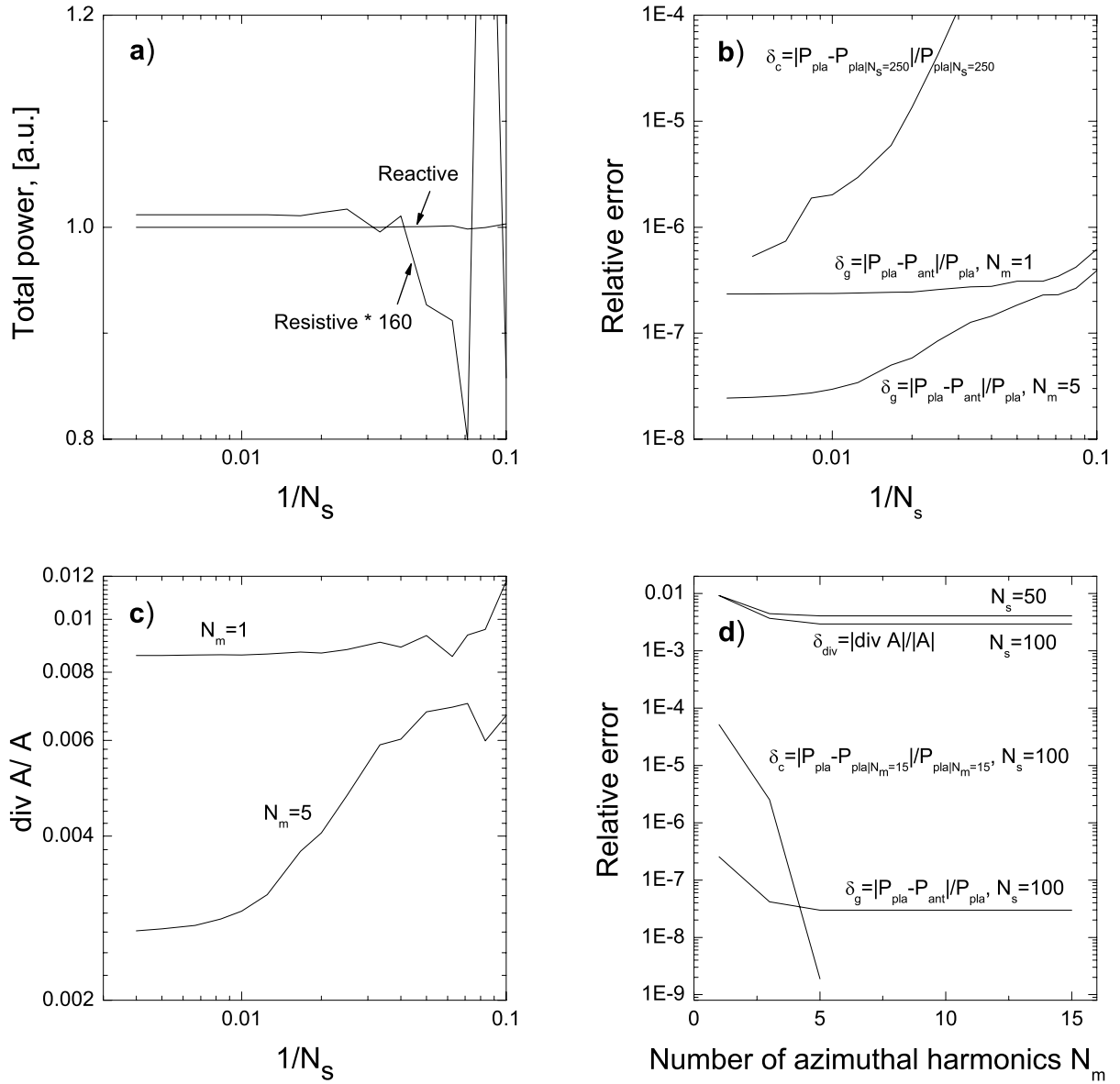


Figure 4.10. *Convergence of power integrals. a) Global power integral P_{pla} as defined in Eq.(3.27) (the resistive part is multiplied by 160) as a function of the radial mesh size; b) Convergence of P_{pla} (δ_c) and power balance discrepancy (δ_g) calculated with two numbers of azimuthal modes, $N_m = 1$ and $N_m = 5$; c) Precision of the Coulomb gauge for calculations with $N_m = 1$ and $N_m = 5$; d) Gauge and global power balance convergence with the number of azimuthal modes.*

global oscillations, that do not satisfy the local resonance condition. In a cylindrical plasma with current, these solutions can exist just below the lower edge of the Alfvén continuum; they are called *global Alfvén eigenmodes* (GAE) [60,61]. The GAE, corresponding to the discrete stable kink modes, can also exist in a tokamak geometry. In this case, they are immersed in the Alfvén continuum and can be seen as a peak in the antenna loading as a function of excitation frequency, as observed in the TCA experiment [59]. LEMan has been successfully tested to reproduce GAEs in a cylinder, but we do not show these results here and proceed directly to the tokamak configuration to discuss the eigenmodes induced by non-symmetric terms in the equilibrium. These eigenmodes, specific to the toroidal geometry, provide a stronger test of the LEMan code because they can only be obtained if the toroidal geometrical effects are correctly implemented in the code.

A very important consequence of the cylindrical symmetry is the decoupling between different azimuthal harmonics. Due to this, two resonances with different m can coexist independently at the same frequency and the same radial position, so the continuum branches can cross, as happens at $r/a \approx 0.38, 0.58$ in Figure 4.8. As soon as the symmetry is broken, this picture qualitatively changes. However, even for more complicated geometries, comparison to this simple cylindrical case still remains very helpful; it can give a rough idea about the possible modes in the system. The effect of non-symmetric terms on the Alfvén continuum structure is discussed in the next chapter.

4.2 2D geometry

In this section, we will present results of LEMan calculations applied to 2D configurations. Most of this section is devoted to the tokamak geometry. A gradual transition from a 1D cylinder to a 2D axisymmetric toroidal configuration can be easily done by reducing the aspect ratio. A tokamak configuration provides an excellent case for tests and benchmarks. Being the mainstream of the magnetic confinement fusion program, a lot of resources have been invested in the tokamak program since the late sixties. Many tokamaks have been built since, including such giants as TFTR in the United States, JT-60 in Japan and JET in Europe. An amazing progress in the confinement time and temperatures has been achieved, increasing the Lawson's criterion parameter by more than three orders of magnitude since the first russian tokamaks.

Tokamak confinement is very well studied both experimentally and numerically. There exist numerous codes for E/M wave propagation in 2D toroidal geometry that can be used for comparisons [13–18]. Axisymmetric tokamak geometry is also significantly simpler than the stellarator configuration. The symmetry in the toroidal direction forbids the coupling between different toroidal modes, which makes this configuration much faster to compute and easier to analyse. All of this makes it a perfect configuration for benchmarking.

We will first discuss in detail the effects of the 2D terms on the Alfvén continuum and introduce the terminology used to describe the Alfvén spectrum. A comparison of the LEMan calculations with experimental JET data and with LION code results is also presented. Then, we discuss the conversion to the quasi-electrostatic wave and its eigenmodes in toroidal geometry. To conclude the discussion of the tokamak configuration, we present some results for the wave propagation in the ion-cyclotron range of frequencies in two-species plasma.

Finally, we discuss the effect of toroidal mode coupling on the example of a mirror configuration that still retains the relative simplicity of the 2D geometry.

4.2.1 Continuum, gaps and Toroidicity-induced Alfvén eigenmodes

Bending a straight cylinder into a finite-aspect ratio torus qualitatively changes the behaviour of the Alfvén resonance branches. Whereas in a cylinder the resonances form a continuum in frequencies, toroidal effects can open gaps in this continuum where no local Alfvén resonances (2.37) are present. Also, new types of global oscillation modes appear due to the poloidal non-symmetry of the equilibrium.

In this section, we will discuss the Alfvén spectrum in tokamak geometry using as an example a torus with aspect ratio $R/a \approx 3$ and slightly elongated cross-section ($\kappa \approx 1.2$); $B_0 = 0.8$ T, $n_0 = 4.0 \times 10^{19}$ m⁻³, ι monotonically decreases from 0.59 on the axis to 0.33 on the plasma boundary. The cylindrical modes of this configuration for frequencies below 80 kHz are plotted in Figure 4.11 (left).

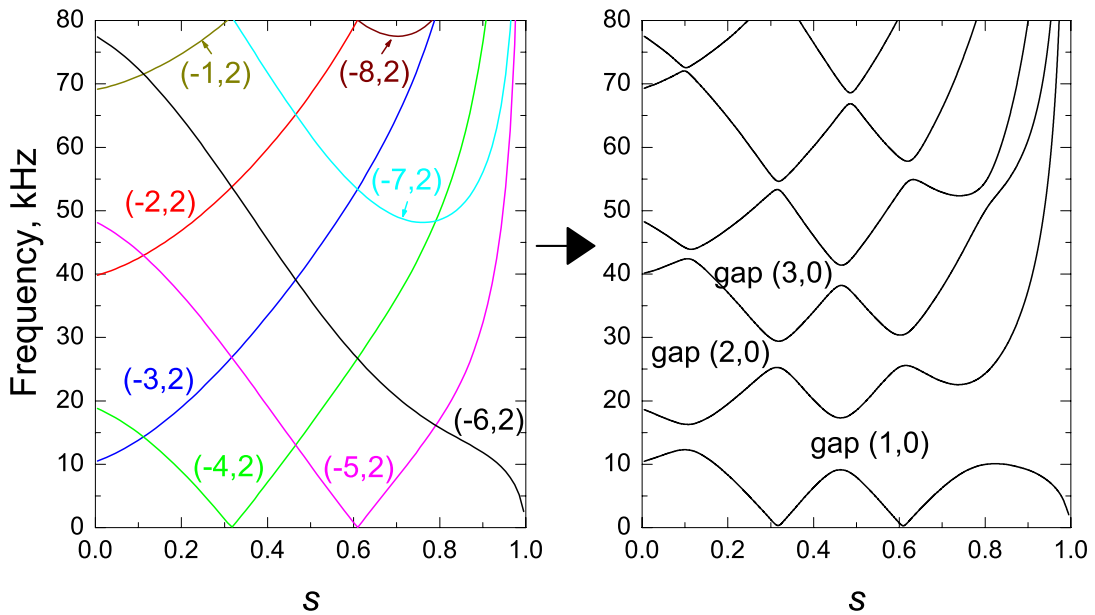


Figure 4.11. **Left:** Alfvén continuum branches calculated with the cylindrical dispersion relation ($k_{\parallel} = (n + \iota m)/R$). **Right:** Frequency versus the radial position of the local Alfvén resonance — continuum structure with gaps formed due to toroidal and higher-order terms in the equilibrium.

Only modes with the toroidal number $n = 2$ are shown. Due to the axial symmetry of the tokamak geometry, different toroidal modes are decoupled, which allows for a separate analysis for each set of modes with the same n . The simple model antenna used here has only one mode $(-3, 2)$ in order to minimise the number of excited harmonics and so to facilitate the interpretation of the results.

In cylindrical approximation, different poloidal modes are independent and the respective Alfvén branches can cross, as it was shown in the previous section. Non-symmetric terms in the equilibrium couple harmonics with different m numbers and remove the degeneracy at the points of intersection so that the branches avoid crossing as shown in Figure 4.11 (right). Each line on the plot corresponds to a mixture of modes; the dominating harmonics, however, are usually still well enough defined by the cylindrical dispersion relation. Mode coupling produces gaps in the continuum where no local Alfvén resonances are present in the plasma in an interval of frequencies⁴. Each gap can be associated with a dominating coupling term in the equilibrium. Thus, the local gaps produced by interaction between $(-4, 2) - (-3, 2)$, $(-5, 2) - (-4, 2)$ and $(-6, 2) - (-5, 2)$ perturbation harmonics are mainly due to the toroidal equilibrium terms; these three local gaps form a global gap denoted $(1,0)$ according to the dominating coupling. Similarly, local gaps produced by $(-5, 2) - (-3, 2)$ and $(-6, 2) - (-4, 2)$ harmonics form a global $(2,0)$ gap due to ellipticity of the configuration; the $(3,0)$ gap if formed by the triangularity of the cross-section, etc. A gap is called *open* if it is not crossed by any continuum branch. It often happens that a local resonance of another mode is present (usually near the plasma edge) at any frequency from the gap interval; the gap is then *closed*. In this terminology, the $(1,0)$ gap in Figure 4.11 is open, and all the higher-order gaps are closed.

The second important difference of the spectrum from the cylindrical case is the presence of the discrete global eigenmodes induced by the non-symmetry of the equilibrium [62]. These modes are different from the global oscillations below the continuum frequencies discussed above (GAE), they can only be obtained in a poloidally non-symmetric

⁴Gaps in the Alfvén spectrum are often compared to the gaps in energy spectrum of electrons between Brillouin zones in a periodic potential in crystals.

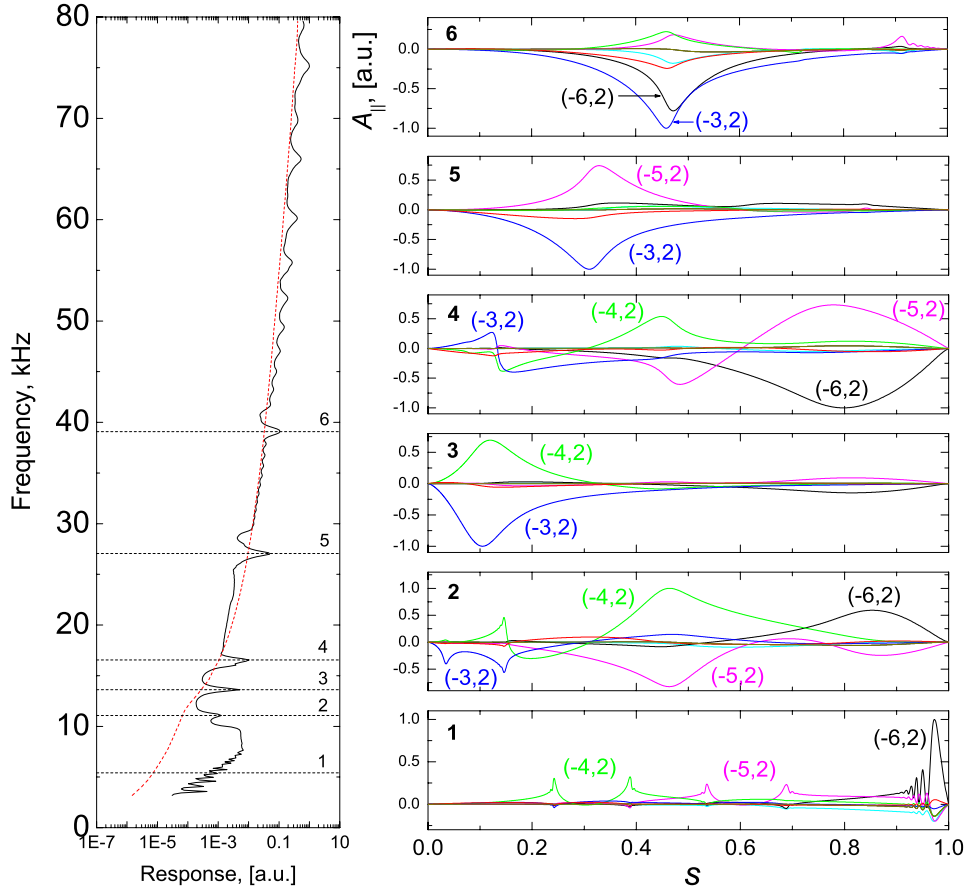


Figure 4.12. **Left:** Frequency scan of a plasma response (normalised) in a toroidal configuration. **Right:** Dominating harmonics in the wavefields (normalised $\Re[A_{\parallel}]$) at different frequencies: 1 – Alfvén continuum, 3 – pure TAE, 2, 4–6 – global eigenmodes + continuum response.

configuration. The frequency of the global modes lies in the gaps of the continuum, it does not satisfy the local Alfvén resonance condition. Since these modes are produced by the interaction of two poloidal mode numbers, the eigenfunctions consist essentially of two harmonics. The wavefields are mainly localised near the center of the gap (radial position of the crossing of the corresponding cylindrical branches).

The global eigenmode solutions can be clearly seen on the frequency scan of the antenna loading. Plasma response in the range 3 – 80 kHz in Figure 4.12 reveals multiple peaks residing inside the gaps opened in the continuum. The peaks denoted "2" – "6" cor-

respond to the global eigenmodes, the smaller peaks below ~ 7 kHz and above ~ 40 kHz are of a different nature and represent eigenmodes of the converted quasi-electrostatic wave that is discussed later in sections 4.2.4, 4.2.5. A plot of the wavefields (Figure 4.12, right) indicate the origin of the peaks.

Peaks "2", "3" and "4" ($f = 11.1, 13.6$ and 16.6 kHz) correspond to the *toroidicity-induced Alfvén eigenmodes* (TAE) residing in the (1,0) gap. These eigenmodes are formed by the interaction between $m = -5, -4$, $m = -4, -3$ and $m = -6, -5$ Fourier harmonics respectively. At $f = 27.1$ kHz ("5") the wavefields are dominated by the $m = -5, -3$ components; it is an *ellipticity-induced Alfvén eigenmode* (EAE) located in the (2, 0) gap. The eigenmode in the (3, 0) gap (peak "6", $f = 39.1$ kHz) is a result of an interaction between $m = -6, -3$ harmonics due to the triangularity of the configuration; so it is a *triangularity-induced Alfvén eigenmode* (TrAE). For each eigenmode, the wavefields have a radially extended structure with the maximum close to the position of intersection of the cylindrical branches. For comparison, plot "1" shows A_{\parallel} in the continuum part of the spectrum ($f = 5.4$ kHz). Wavefields are radially localised near the local Alfvén resonances (2.37), the dominating harmonics are well described by the cylindrical dispersion relation.

Local Alfvén resonances are also present at the eigenfrequencies described above; only the TAE on the plot "3" is a pure global mode in the open gap. When the eigenfrequency of a global mode matches the local Alfvén resonance condition (2.37) at some radial position, the eigenmode can couple to the shear Alfvén wave and additional damping can occur. The eigenmode then tunnels from its region of localisation to the local resonant position; the tunnelling is stronger for low toroidal wavenumbers n [63]. The eigenmode is then partially damped due to the absorption mechanism of the shear wave which has been shown to be much larger than the direct electron Landau damping of the eigenmode for typical fusion plasma parameters. This resonant damping through the shear wave is estimated to be the most effective mechanism of energy absorption of a TAE at small or moderate n . This analysis, of course, require the finite temperature effects to be taken into account. However, in the cold plasma model implemented here, we see the

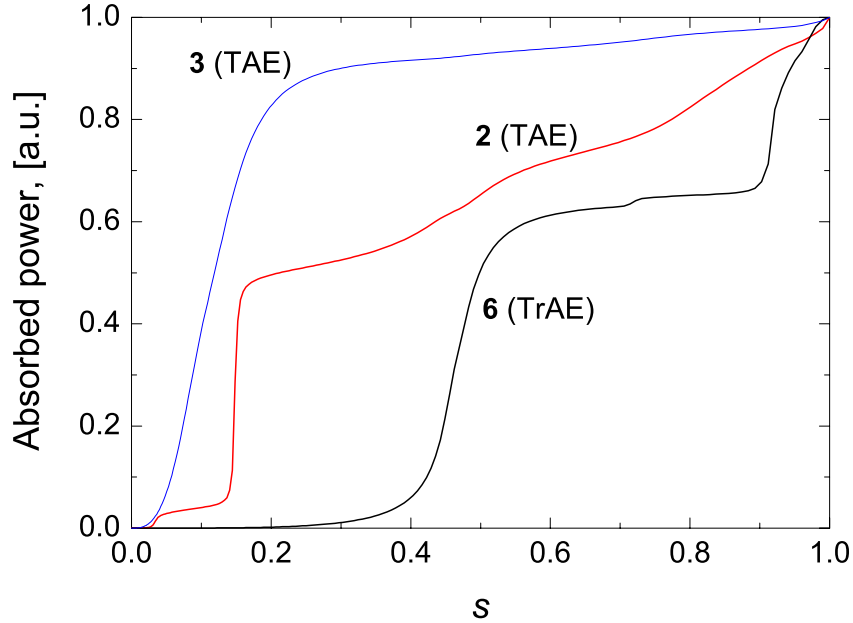


Figure 4.13. *Cumulative integral of absorbed power (normalised to the maximum value for each frequency) as defined in Eq.(3.27) at $f = 11.1$ kHz (2), 13.6 kHz (3), 39.1 kHz (6).*

same effect of the eigenmode damping through interaction with a local Alfvén resonance (Figure 4.13). Even though the wavefields at $f = 11.1$ kHz (curve 2) are dominated by the TAE eigenmode localised near $s \approx 0.45$, the power is mostly absorbed near $s \approx 0.15$, i.e. the radial position of the local Alfvén resonance of the $(-4, 2)$ mode. Similarly, for the TrAE at $f = 39.1$ kHz (curve 6), a considerable part of energy is absorbed near $s \approx 0.9$, i.e. where the local resonance condition is satisfied for $(-5, 2)$ harmonic. For a pure TAE (curve 3), the energy is mainly deposited near the position of localisation of the eigenmode.

4.2.2 Comparison with experimental data

The frequency of the TAE obtained with the LEMan code has been compared to the measurements of the low-frequency activity during the JET discharge #52206 [64]. This experiment has originally been conducted to compare the damping rate of the TAE with the predictions of the kinetic stability 2D code NOVA-K [14]. The cold plasma model

implemented in LEMan cannot be applied to obtain damping rates, but the code can still evaluate the real part of the oscillation frequency. The plasma configuration of this shot has a very low elongation and triangularity which remain approximately constant during the phase of the discharge we are interested in. The ι profile is monotonic and varies from $\approx 1.14 - 1.3$ on the axis to $\approx 0.27 - 0.29$ on the plasma boundary in the time interval $59 \leq t \leq 63$ secs. The magnetic field on the axis decreases from ≈ 1.5 to ≈ 1 T. Two in-vessel antennae are configured to preferentially excite the $n = 1$ toroidal mode.

The dedicated Alfvén eigenmode diagnostic system uses repetitive sweeps of the exciting antenna frequency in the range 20 – 500 kHz. The generated perturbations of the magnetic field are small enough not to disturb the plasma and not to produce any non-linear effects ($\delta B/B_0 < 10^{-5}$) [65, 66]. The TAE frequency measurement results are shown in Figure 4.14 with cross markers. Eigenfrequencies found by performing plasma response scans with LEMan are in a good agreement with these values.

A comparison of the LEMan results to the JET data is a technically complicated and

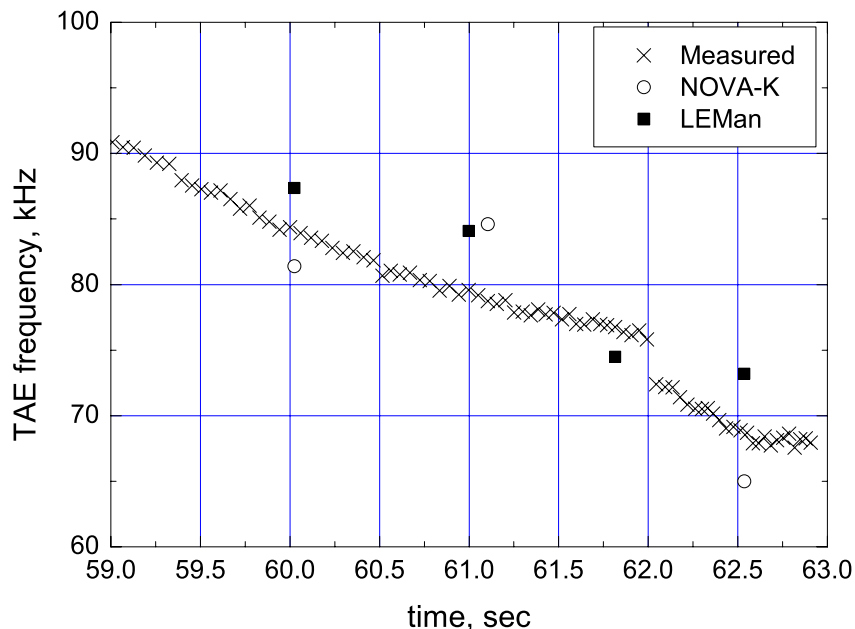


Figure 4.14. Evolution of the TAE frequency for $n = 1$ mode during the Ohmic heating phase of JET discharge #52206.

time-consuming process because of different platforms used for the equilibrium reconstruction. The JET equilibrium data available are fitted using the EFIT [67] and CHEASE [68] 2D codes. This equilibrium for each time-slice has to be Fourier-transformed to provide an input to the spectral 3D equilibrium code VMEC. Moreover, EFIT and CHEASE employ the normalised poloidal flux or its square root as the radial variable for all the flux functions. VMEC, TERPSICHORE and LEMan, on the other hand, use the normalised toroidal flux as the surface label, so all the flux functions (ι , plasma density, etc) have to be recalculated before reconstructing the underlying equilibrium with VMEC. Considering these multiple transformations of the equilibrium data, the agreement between the LEMan results and the experimentally measured frequencies is very good and shows the robustness of the numerical scheme.

4.2.3 Comparison with the LION code

Another test of the newly developed code has been provided by a comparison to the calculations performed with the 2D cold plasma LION code [13]. Both codes use a similar plasma model. LION neglects the finite electron inertia effects and thus the conversion to the quasi-electrostatic wave (2.36), so the wavefields cannot be directly compared. However, the Alfvén resonance radial positions and the eigenfrequencies of the global modes should be approximately the same. In Figure 4.15 (left) the Alfvén continuum spectrum is shown for a simple tokamak configuration with $R/a = 4$ and circular cross-section, $n_0 = 4.0 \times 10^{19} \text{ m}^{-3}$, $B_0 = 0.8 \text{ T}$, toroidal mode $n = 1$.

Alfvén resonance radial positions near the gap edge obtained with the two codes are very close, within few radial mesh intervals. As expected, the perturbed wavefields in the continuum part of the spectrum show a singular behaviour at the resonant magnetic surface in the case of zero electron inertia (LION model), or a conversion to short wavelength oscillations, the QEW, in the case of finite electron mass (LEMan model).

The plasma response frequency scan in the gap region performed with the two codes reveals the presence of a discrete mode, the TAE (Figure 4.15, right). The positions

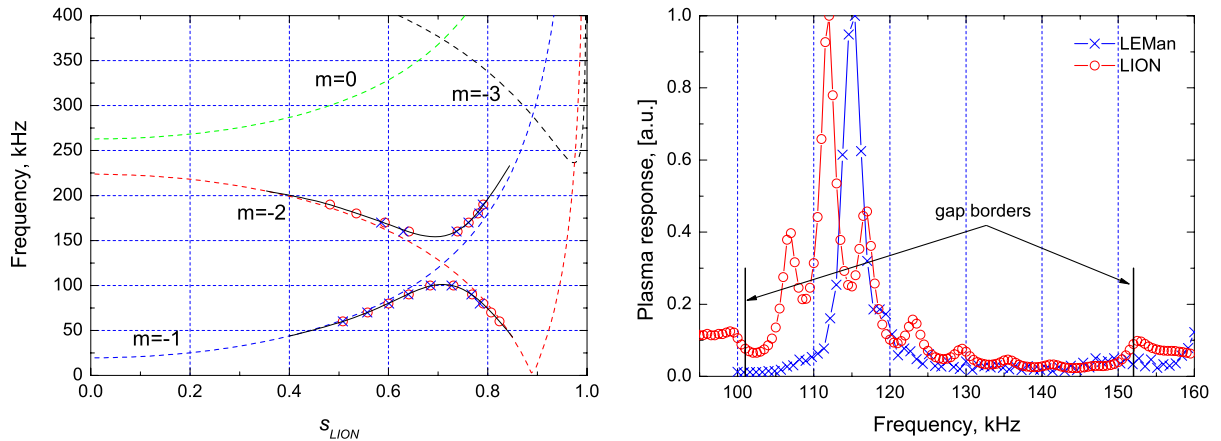


Figure 4.15. **Left:** *Alfvén continuum in tokamak geometry near the gap. Dotted lines – cylindrical modes, solid lines – approximate positions of the continuum branches in toroidal geometry.* **Right:** *Frequency scan in the gap region. For both plots: circles – LION code calculations, crosses – LEMan results.*

of the maxima given by LION and LEMan are in a good agreement; the discrepancy of $\approx 3\%$ can be explained by the difference in the plasma models and different ways to represent the underlying numerical equilibrium. Here again, the comparison is technically complicated by the difference in inputs: LION uses CHEASE equilibrium with a square root of the poloidal magnetic flux as the radial variable s ; LEMan has an interface to TERPSICHORE, which, in turn, takes VMEC input with s proportional to the toroidal flux.

4.2.4 Quasi-electrostatic wave

The quasi-electrostatic wave, or quasi-electrostatic surface wave (QEW or QESW) is not a particular feature of the tokamak geometry, it can be seen in every configuration near the position where the local Alfvén resonance condition is satisfied. It can also be obtained in the 1D cylindrical geometry. However, we decided to present it here in the 2D results section because the tokamak coupling can have interesting effects on the propagation of QEW without obstructing too much its physical nature.

It is interesting and illustrative to see how the local approach presented in section 2.6 can be directly compared to the results obtained with the global code on the example of QEW. By local approach we understand a solution of the dispersion relation written for an infinite homogeneous plasma (2.36). Applied to a plasma cylinder with a parabolic density profile, this method still gives a result that is amazingly close to the global numerical solution of the propagation problem.

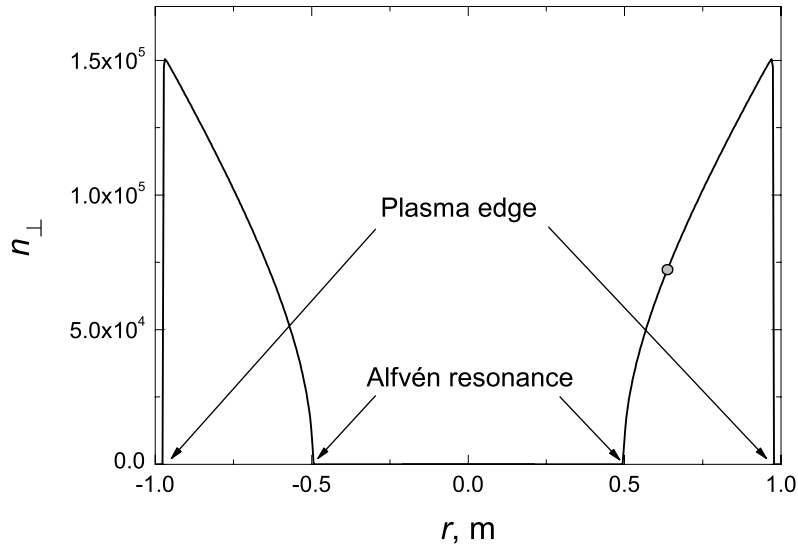


Figure 4.16. *Perpendicular refractive index of the QEW obtained from the WKB approach (1D cylinder, $B_0 = 0.8$ T, $n_0 = 4.0 \times 10^{19} \text{ m}^{-3}$, $f_{\text{antenna}} = 102$ kHz, $(m, n)_{\text{antenna}} = (20, 1)$). The fast wave solution is not shown here.*

As it was shown in the section 2.6, the QEW solution can be obtained from the cold plasma dielectric tensor dispersion relation as a finite electron mass modification of the shear Alfvén wave in the MHD limit. First, let us consider a 1D cylinder. When resolved for a simple 1D cylindrical configuration with no poloidal equilibrium magnetic field, a parabolic density profile and a parallel wave vector and a frequency fixed by the antenna, the local dispersion relation gives the solution for the perpendicular refractive index that is real outside the Alfvén resonant surface located at $r \sim 0.5$ m for the parameters chosen (Figure 4.16).

This solution describes a fast-oscillating wave in the direction perpendicular to \vec{B}_0 (high n_\perp), propagating outwards from the Alfvén resonant surface. This wave is clearly observed in the global solution obtained with LEMan for the same parameters (Figure 4.17).

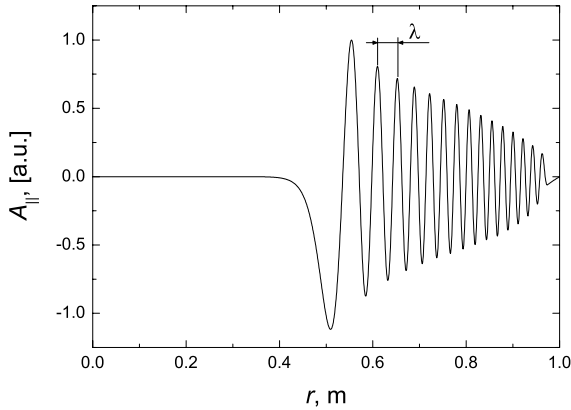


Figure 4.17. The $(20, 1)$ Fourier term of the normalised parallel component of the perturbed vector potential in a cylinder calculated with LEMan (only the real part is shown).

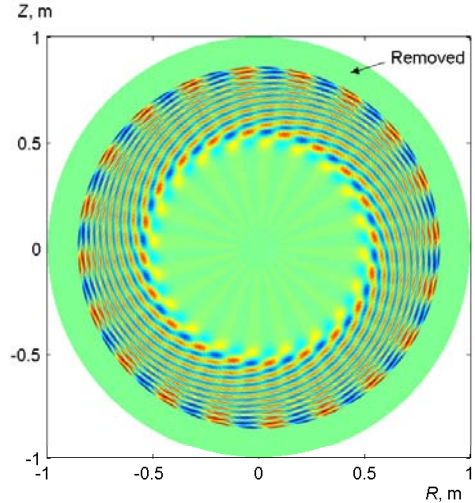


Figure 4.18. The space structure of the perturbed magnetic field poloidal component (Several external surfaces are removed from the plot).

In Figure 4.18, the same mode is plotted in real space. Several magnetic surfaces close to the plasma edge are removed from the figure to keep the color scaling of the QEW oscillations readable (otherwise, it is dominated by the direct contribution of the antenna located just outside the plasma).

A very simple calculation demonstrates the relation between the local and global pictures. If we measure the wavelength of the oscillations at some radial position as shown in Figure 4.17, we get the value of the wave vector radial component:

$$k_r = \frac{2\pi}{\lambda} = 153 \text{ m}^{-1} \quad \text{at} \quad r = 0.64 \text{ m.}$$

The poloidal component of \vec{k} is defined by the poloidal mode number, in our case it is 20:

$$k_\theta = |\nabla_\theta| = |\nabla\theta| \left| \frac{\partial}{\partial\theta} \right| = \frac{m}{r} = 31.3 \text{ m}^{-1}$$

and so we obtain the perpendicular component of \vec{k} : $k_\perp = \sqrt{k_r^2 + k_\theta^2} = 156 \text{ m}^{-1}$. The value given by the local solution of the dispersion relation at the same radial position (Figure 4.16) is surprisingly close: $k_\perp = n_\perp \omega / c = 156.4 \text{ m}^{-1}$. As the radial position moves out from the Alfvén resonance towards the plasma edge, the perpendicular refractive index rapidly increases and the radial wavelength becomes shorter, so the angle between \vec{k}_r and \vec{k}_\perp decreases and constant phase surfaces look almost like concentric circles (Figure 4.18).

We will now apply the same analysis to a tokamak configuration with circular cross section, major radius $R_0 = 5 \text{ m}$ and minor radius $a = 2 \text{ m}$. In a torus with an aspect ratio of 2.5 the coupling of poloidal modes is very important and changes the behaviour of the QEW. The Alfvén resonance positions are no longer described by the cylindrical expression, but it is still convenient to use the corresponding 1D counterparts to get a qualitative picture of the mode structure.

In Figure 4.19, we have plotted the Alfvén resonance frequency as a function of the

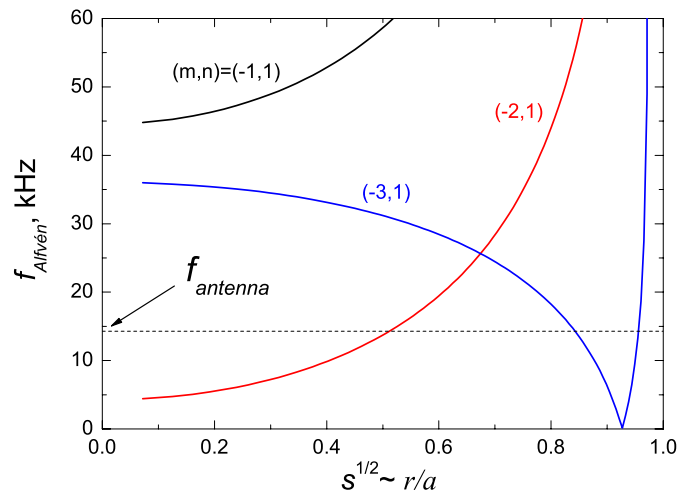


Figure 4.19. Alfvén resonance branches in a 1D cylinder with the same ι profile as in the torus.

”radial position”. In a torus, \sqrt{s} is no longer exactly equal to the minor radius, but is close to it near the axis. As can be seen from the figure, at the antenna frequency of 14.3 kHz we can expect to have two resonant surfaces located near radial positions $\sqrt{s} \approx 0.5, 0.85$ with dominating poloidal mode numbers $m = -3, -2$.

In order to use the local dispersion relation we need to know the parallel wave vector of the perturbation. Unlike in the cylindrical geometry, it cannot be obtained as a simple algebraic expression for a torus. However, we can still get a quantitative idea about the solution by using the cylindrical form $k_{\parallel} = (n + \iota m)/R$ as a first approximation with corresponding mode numbers. For a model helical antenna with only one harmonic $(m, n) = (-2, 1)$, the dominating perturbed modes are $(-3, 1)$ and $(-2, 1)$. Substituting these to the expression for the k_{\parallel} and calculating the resulting refractive index n_{\perp} , we get two different solutions shown in Figure 4.20.

The two solutions $n_{-2\perp}$ and $n_{-3\perp}$ overlap in a toroidal tube volume where the QEW can propagate. The resulting refractive index n_{\perp} is a combination of both $n_{-2\perp}$ and $n_{-3\perp}$, we model it here by a simple function $\sqrt{n_{-2\perp}n_{-3\perp}}$ that is plotted in Figure 4.20 as a solid line. A contour plot of n_{\perp} in a toroidal cross-section is presented in Figure 4.21.

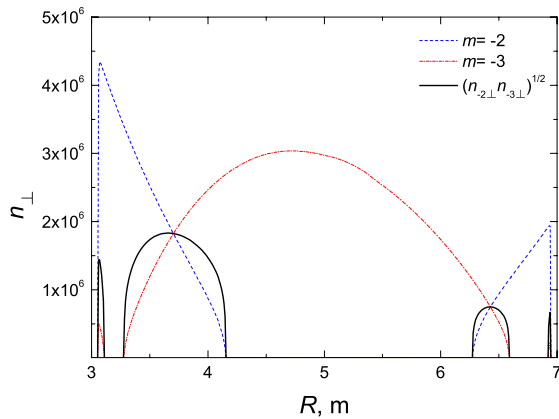


Figure 4.20. *Perpendicular refractive index as a function of radius in the equatorial plane.*

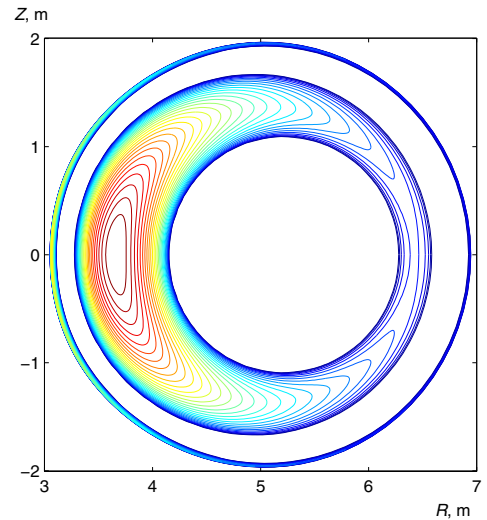


Figure 4.21. *Contour plot of the model refractive index $\sqrt{n_{-2\perp}n_{-3\perp}}$ in a toroidal cut.*

The global solution qualitatively confirms the validity of these considerations. In the plot of Fourier harmonics of the parallel component of \vec{A} we see again the short-wavelength oscillations (Figure 4.22). Now, they are confined between the two Alfvén resonances. In real space (Figure 4.23), it corresponds to a propagation in a toroidal tube of a size similar, but not exactly equal, to the one found with a qualitative local analysis. The main difference of the global solution is that the region of propagation of QEW is confined between two magnetic surfaces, unlike for the solution with an approximate expression for n_{\perp} of Figure 4.21.

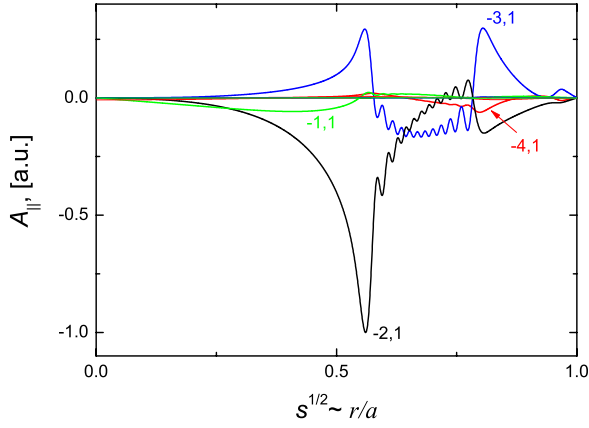


Figure 4.22. Normalised A_{\parallel} calculated with LE-*Man*, real part of Fourier components.

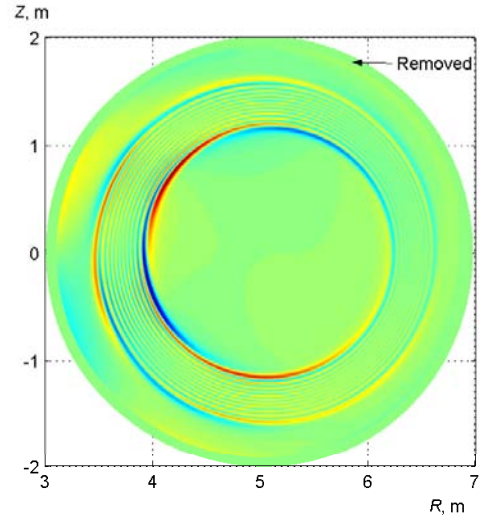


Figure 4.23. Normalised binormal component of the perturbed magnetic field of the QEW in a torus.

The comparison with the analytical expression is, of course, far from precise, unlike for a cylinder. The radial wavelength estimated from the global solution in the middle of the left part of the propagation domain (equatorial plane) in Figure 4.23 gives a value of approximately 3.4 cm. For low poloidal mode numbers the perpendicular wave vector is then obtained as $k_{\perp} \approx 2\pi/\lambda \approx 190 \text{ m}^{-1}$, so $n_{\perp} \approx 6.3 \cdot 10^5$. The value of the model n_{\perp} obtained with the local WKB approach (Figure 4.20) is roughly 2-3 times larger. Such a big difference is not surprising for a small aspect ratio torus because we used a cylindrical expression for the parallel component of the wave vector.

4.2.5 Quasi-electrostatic wave eigenmodes

Resolving the approximate dispersion relation (2.36), we can find the region of propagation of the quasi-electrostatic wave for $\omega \ll \Omega_i$:

$$n_{\perp}^2 = \left(\frac{c_A^2 k_{\parallel}^2}{\omega^2} - 1 \right) \frac{\Pi_e^2}{\omega^2}.$$

In a 1D cylinder, the region of propagation can be calculated separately for each (m, n) Fourier harmonic of perturbation. Depending on the sign of the radial derivative of $c_A k_{\parallel}$ at the value of perturbation frequency, the converted QEW in the cold plasma model can propagate either inwards or outwards from the Alfvén resonance $\omega = c_A k_{\parallel}$.

An interesting effect can be observed in a geometry with broken poloidal (or toroidal) symmetry. If two Alfvén resonant surfaces are located in the plasma and the two corresponding quasiolelectrostatic waves propagate in the same region, the converted waves can interact if their poloidal (in case of tokamak geometry) or toroidal (in mirror configuration) modes are coupled. This usually happens at frequencies just below the poloidal or toroidal gap formed by the coupling near the crossing of corresponding cylindrical continuum branches (like, for example, in the case of Figure 4.22). This situation is schematically presented in Figure 4.24.

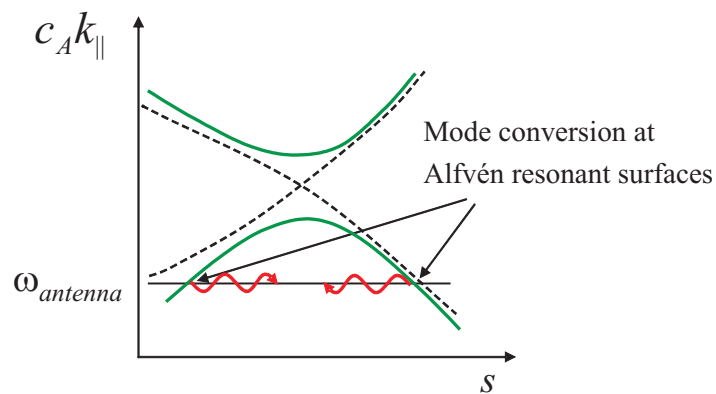


Figure 4.24. *Schematic drawing of mode conversion in the presence of two Alfvén resonances below the gap. Dashed lines — cylindrical branches, solid curves — 2D branches of the Alfvén resonances.*

If damping is not too strong, the interaction of the two short-wavelength oscillations can form a standing wave which results in a characteristic sequence of minima and maxima in the absorbed energy as a function of perturbation frequency as shown in Figure 4.25 (left plot) for the same toroidal configuration as used for calculations in the previous section.

The peaks in plasma response indicate the presence of eigenmodes formed by the interaction of the two converted waves. Indeed, each maximum corresponds to an integer

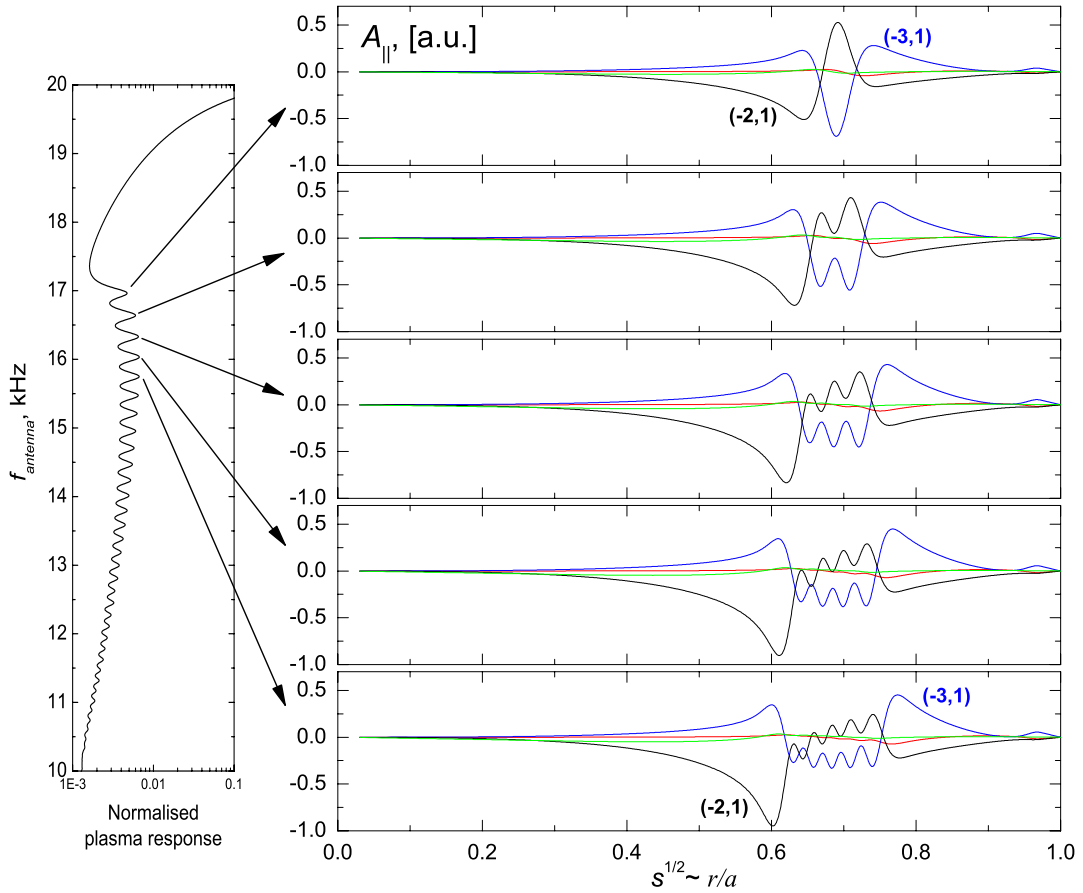


Figure 4.25. **Left:** Frequency scan of the absorbed power below the gap for a torus with aspect ratio 2.5. Horizontal axis — normalised resistive power. **Right:** wavefields (real part of the A_{\parallel} Fourier components, normalised) corresponding to peaks in the plasma response frequency scan.

number of radial wavelengths that fit between two Alfvén resonances, as clearly seen from the wavefields on the right of the Figure 4.25. As the antenna frequency decreases, the Alfvén resonant surfaces move in opposite directions (see Figure 4.19) so the interaction of the converted waves weakens and the peaks become less pronounced.

Another indication of the eigenmode nature of the peaks in this frequency scan is the type of dependence of the value of absorbed power on the imaginary part ν in the dielectric tensor. As one can see from the plot in Figure 4.26, this power is exactly inversely proportional to ν , which is a characteristic dependence for an eigenmode of a system.

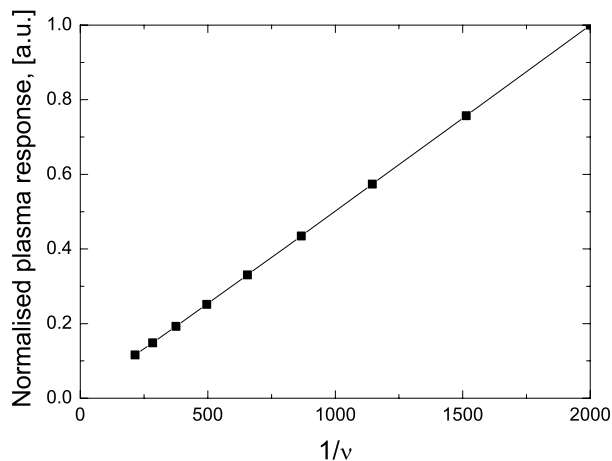


Figure 4.26. *Normalised plasma response at $f_{\text{antenna}} = 16.64$ kHz (peak position) as a function of imaginary part in the dielectric tensor.*

Thus, we can say that in the finite-electron mass model the Alfvén continuum becomes discrete, so it is no longer a "continuum" in the proper sense, but is composed of a set of discrete (damped) eigenmodes of QEW.

The quasi-electrostatic wave can only be obtained in the finite-electron mass model. In the absence of m_e and parallel electric field, there is no mode conversion at the Alfvén resonance, so the plasma response (in the continuum range of frequencies) does not have the discrete peak structure⁵.

⁵When finite Larmor radius effects are included, there is mode conversion, even with $m_e \rightarrow 0$, to the Kinetic Alfvén Wave [15, 50].

4.2.6 Ion-cyclotron range of frequencies

All of the 2D results presented above were limited to the Alfvén range of frequencies, i.e. very low frequencies below ion-cyclotron. We will now discuss how the presence of an ion-cyclotron and an ion-ion hybrid resonance affects the wave propagation for higher frequencies.

The slow and fast solutions of the cold plasma dispersion relation coexist for the frequencies below the ion-cyclotron frequency of the heaviest species in the plasma. Above this frequency, the shear Alfvén wave does not propagate and only the fast branch remains (see Figure 4.6). If the ion-cyclotron resonance $\omega = \Omega_i$ crosses the magnetic surfaces, as usually happens in the ICF range in toroidal configurations somewhere in the plasma, the nested topology of the Alfvén resonant surfaces is broken. In a tokamak, Alfvén waves cannot propagate on the low-field side of the ion-cyclotron resonance vertically crossing the plasma. The fast magnetosonic branch of the solution, on the other hand, does propagate both below and above Ω_i , so it is a possible candidate for plasma heating. However, fast wave heating is more subtle than simply exciting the wave at the ion-cyclotron frequency. Note that the cyclotron frequency does not constitute a wave resonance for the fast wave. This can be easily seen from the behaviour of the cold plasma dispersion relation near Ω_i . Indeed, all the coefficients of the dispersion relation (4.2) have the same asymptotics as ω approaches Ω_i : $a, b, c \propto 1/(\omega^2 - \Omega_i^2)$ which means that Ω_i is not a singular point of the dispersion relation and the refractive index n_\perp is finite. Moreover, noting that near Ω_i the coefficient S behaves as $-D$ (2.29), the solution of Eq.(2.32) has a circular right-handed polarization $E_x = -iE_y$ at the cyclotron frequency. Thus, the electric field rotates in the direction opposite to the cyclotron gyration of ions and does not resonate with them even if the frequency of the rotation is the same⁶.

The effect of the presence of an IC resonance in the plasma with one ion species in tokamak geometry is illustrated in Figure 4.27.

⁶These considerations are valid for the cold plasma model. Inclusion of finite temperature effects results in corrections to the wave-ion interaction of the order of $\sim (k_\perp \rho_i)^4$ for the first harmonic and of the order $\sim (k_\perp \rho_i)^2$ at the frequency of the second harmonic.

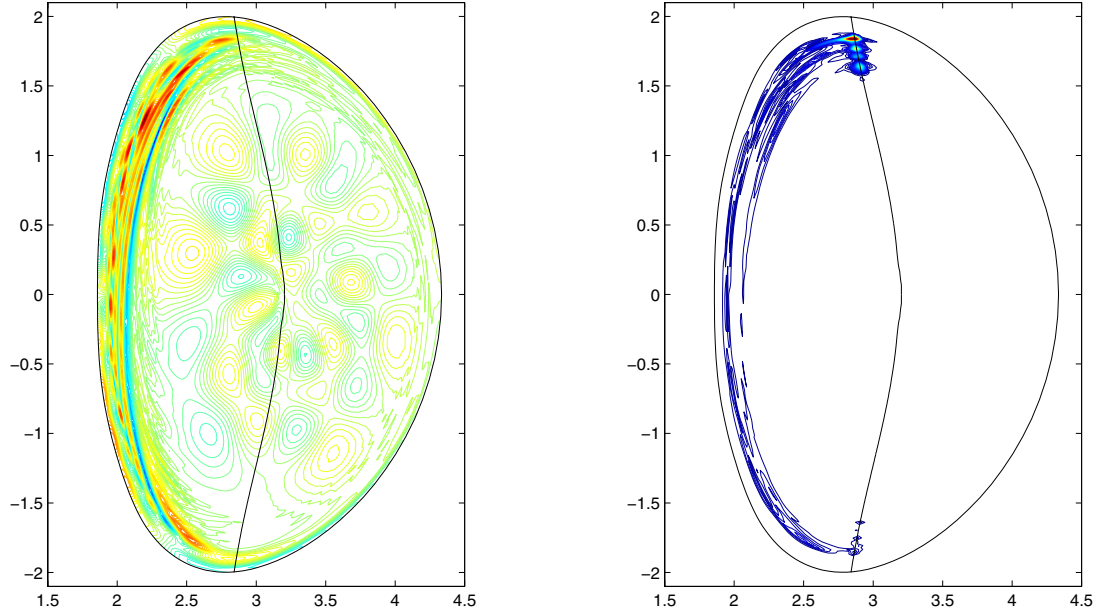


Figure 4.27. *Contour plot of the binormal component of the perturbed magnetic field (left) and absorbed power density (right). The vertical line shows the surface $\omega_{\text{antenna}} = \Omega_i$. The example corresponds to a deuterium plasma, with $B_0 = 3.4$ T, $n_0 = 3.2 \times 10^{19} \text{ m}^{-3}$, $f_{\text{antenna}} = 25.5$ MHz.*

On the high-field side from the continuous vertical line, the frequency is below the cyclotron frequency, so the Alfvén wave can propagate and we see the characteristic radial surfaces of the converted quasi-electrostatic wave. The fast magnetosonic wave is propagating both below and above Ω_i , and the wavefields do not have any particular behaviour at the ion-cyclotron resonance (except their polarisation), confirming that it does not constitute a wave resonance.

So, at least in cold plasma with one ion species, heating at the frequencies near the cyclotron resonance does not look very promising. This picture changes when a second ion species is present in the plasma. A new resonance appears in the plasma at a frequency between the cyclotron frequencies of the two species. This resonance can be found from the simplified dispersion relation neglecting low-order terms in m_i/m_e . In fusion plasma parameters, $\Pi_e \sim \Omega_e$ in the center of a tokamak, so for frequencies near Ω_i the coefficients

in Eq.(2.29) have the following dominating scalings in m_i/m_e :

$$\begin{aligned} P &\sim \frac{\Pi_e^2}{\omega^2} \sim \frac{\Pi_e^2}{\Omega_i^2} \sim \left(\frac{m_i}{m_e}\right)^2 \\ S \sim D &\sim \frac{\Pi_i^2}{\Omega_i^2} \sim \frac{m_i}{m_e}. \end{aligned}$$

The solution of the dispersion relation (4.2) in the approximation $P \gg S, D$ can then be simplified as

$$n_{\perp}^2 \approx \frac{\left(S - n_{\parallel}^2\right)^2 - D^2}{S - n_{\parallel}^2}.$$

Therefore, the resonance is given by

$$S - n_{\parallel}^2 = 0, \quad (4.4)$$

which is the same expression that describes the Alfvén resonance. In a single species plasma, the resonant frequency of (4.4) always lies below the ion-cyclotron frequency (Alfvén resonance). However, if a second species is present, another solution is possible at the frequency above the ion-cyclotron frequency of the heavier ions. In this case, the solution is approximately given by

$$\frac{\Pi_1^2}{\omega^2 - \Omega_1^2} + \frac{\Pi_2^2}{\omega^2 - \Omega_2^2} = 0,$$

which results in the resonant ion-ion hybrid frequency

$$\omega^2 = \frac{\Omega_1^2 m_1 n_2 + \Omega_2^2 m_2 n_1}{n_1 m_2 + n_2 m_1},$$

where n_1 and n_2 are the densities of the ion fractions (here, we neglected n_{\parallel} in comparison with S). Energy is damped at the hybrid resonance through the resonant absorption mechanism described by Budden [69]. If finite temperature effects are taken into account, the singularity at the resonance can be resolved by mode conversion to an ion Bernstein wave.

We will now present a few results demonstrating wave propagation in a tokamak plasma containing a hybrid resonance. We have chosen a geometry based on a JET equilibrium with $B_0 = 3.4$ T, $n_{e0} = 3.2 \times 10^{19} \text{ m}^{-3}$, $R_0 \approx 3$ m, $a \approx 1.25$ m, $q_0 = 1.03$ and

$q_a = 2.2$. The plasma is composed of 70% of deuterium and 30% of hydrogen ions. A very similar configuration was used for LION calculations [56], which gives a good comparison case.

Wave propagation in the presence of a hybrid resonance and cutoff in the plasma strongly depends on the position of the antenna. For this configuration, we used two types of antenna — a low-field side antenna with poloidal extent of about $-60.. +60$ degrees located in the narrow vacuum layer between the edge of the plasma and the conducting shell and a high-field side antenna with similar size. The toroidal wave number for these calculations is -15 .

An idea about wave propagation can be given by the WKB solution of Eq.(2.33). A radial dependence of the solution of the full cold plasma dispersion relation with k_{\parallel} approximated by n/R is shown in Figure 4.28. The n_{\perp} shown corresponds to the fast magnetosonic wave at $f = 43$ MHz. The second solution of Eq.(2.33) is strongly evanescent at this frequency and does not propagate.

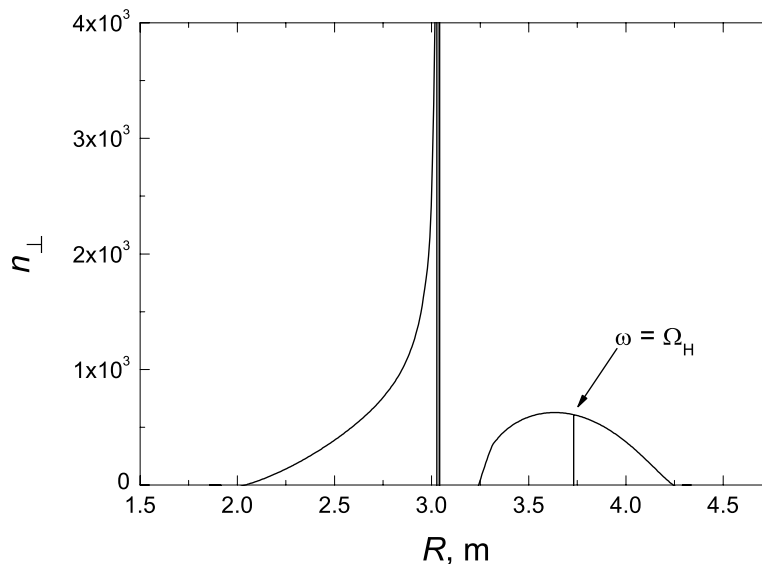


Figure 4.28. *WKB solution of the dispersion relation for two-species plasma in the equatorial plane. Parameters: deuterium plasma with 30% hydrogen, $B_0 = 3.4$ T, $n_0 = 3.2 \times 10^{19} \text{ m}^{-3}$, $f_{\text{antenna}} = 43.0$ MHz, toroidal wave number $n = -15$.*

The singularity at $R \approx 3.03$ m is, in fact, composed of two very close resonances. One of them is given by Eq.(4.4), another one corresponds to $S = 0$. For these parameters, S is much larger than the parallel refractive index, so the two resonances are nearly identical. For brevity, we will call them here the ion-ion hybrid resonance.

Coming from the high-field side (left), the fast wave encounters the hybrid resonance and is completely absorbed. When launched from the low-field side (right), the wave arrives at a cutoff first. It can partly tunnel through the evanescent region to be absorbed at the resonance, but if the distance between the resonance and cutoff is large, it is mostly reflected and, superposing with the incident wave, can form eigenmodes.

The two corresponding plasma response frequency scans are presented in Figures 4.29 and 4.30. The calculations were done for three different values of the ad hoc imaginary part in the frequency: $\nu = 2 \times 10^{-3}, 5 \times 10^{-3}$ and 1×10^{-2} . The grid is composed of 96 radial nodes and $N_\theta=150$ poloidal mesh points for equilibrium discretisation; $N_s=150$ radial elements and $N_m=45$ poloidal harmonics were used for perturbations (we will refer to these parameters as "low resolution"). Calculations for $\nu = 2 \times 10^{-3}$ require higher numerical resolution: we used $N_\theta=240$, $N_s=200$ and $N_m=73$ to verify the numerical convergence (we will call it here "high resolution").

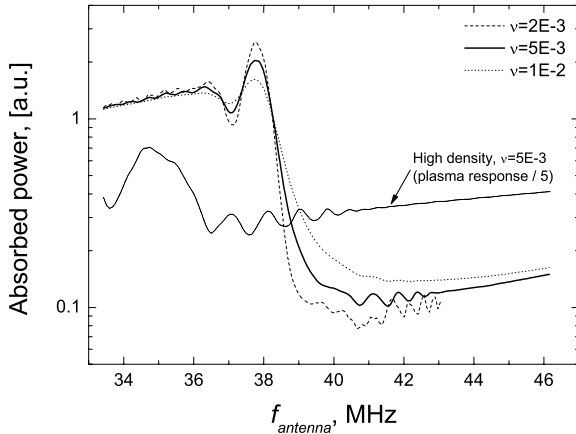


Figure 4.29. Normalised absorbed power as a function of frequency in case of high-field side heating, JET equilibrium.

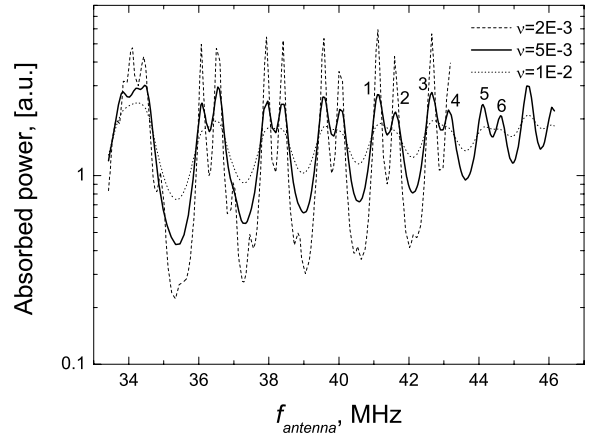


Figure 4.30. Same frequency scan for low-field side antenna.

As can be seen from the left plot, the absorbed power depends almost monotonically on the wave frequency above ≈ 41 MHz. No eigenmodes are present in the system because of the total absorption of the incident wave at the hybrid resonance. The structure of the wavefield and absorption for high-field side antenna with $f = 41.4$ MHz is shown in Figure 4.31.

As we see from these figures, the wave is localised on the high-field side of the hybrid resonance, and is mostly absorbed at this resonance. The absorption spot on the left of the Figure 4.31 is located very close to the antenna, where the directly induced wavefields are very strong.

As the frequency decreases below ≈ 39 MHz, the plasma response starts to rise very fast. At about this frequency the deuterium cyclotron resonance enters the plasma on the high-field side. The cyclotron resonance itself does not affect the propagation, but it allows the second branch of the dispersion relation solution to propagate. This branch, the Alfvén wave, at frequencies close to ion cyclotron is also called ion cyclotron wave. Resonant absorption of this wave explains the difference in the behaviour of the plasma response. As can be seen from Figure 4.32 (right), almost all the power is absorbed in the very narrow layer between the antenna and the deuterium cyclotron resonance. The peaks in the plasma response are due to the eigenmodes of the QEW that have been described above. The structure of the wavefields also indicates the presence of a shear Alfvén wave. The perpendicular components of the perturbed magnetic field are very strong in the region of absorption and smaller elsewhere (Figure 4.32, left). The parallel component of \vec{B} (not shown), on the other hand, is small in the resonant region, which is characteristic for a shear wave.

Yet another indication of the Alfvén nature of the absorption for frequencies below ≈ 39 MHz is the dependence of the plasma response on the density. For the same configuration but with a higher density the sudden increase in absorption appears at a lower frequency of ≈ 36 MHz (Figure 4.29, dashed line), as should be expected for an Alfvén wave.

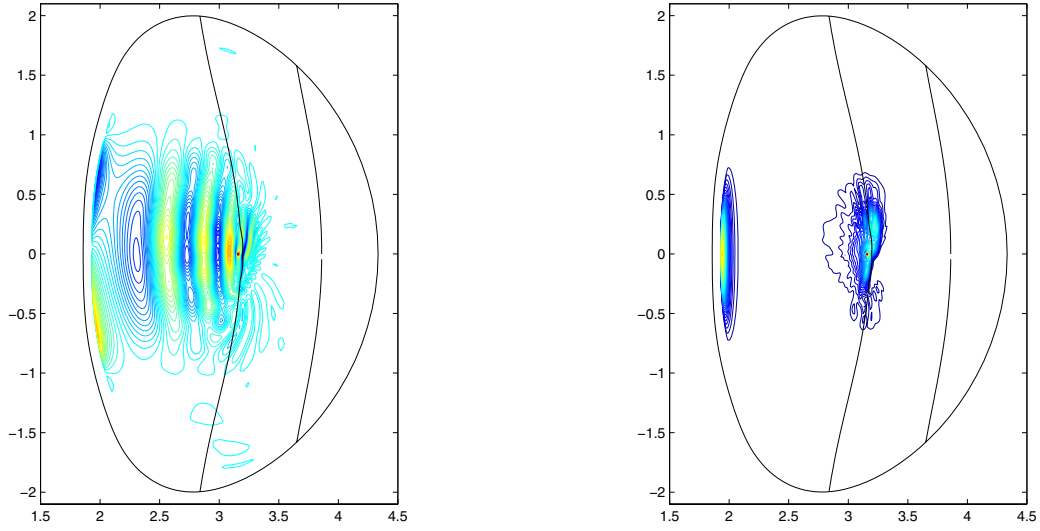


Figure 4.31. *Spatial structure of the electric field binormal component (left) and the density of absorbed power (right), HFS antenna, $f = 41.4$ MHz, $\nu = 5 \times 10^{-3}$. Left vertical line — ion-ion hybrid resonance, right line — hydrogen ion cyclotron resonance.*

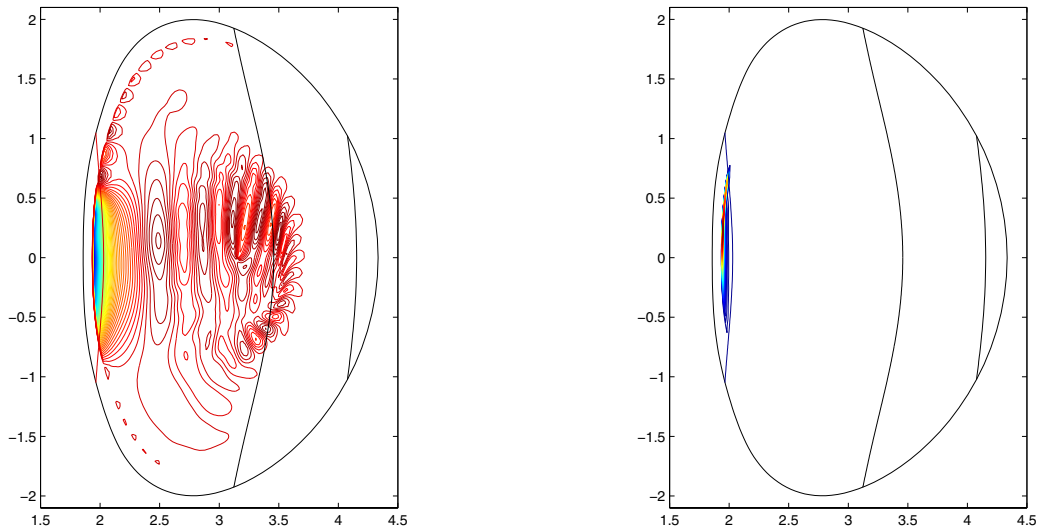


Figure 4.32. *Spatial structure of the magnetic field normal component (left) and the density of absorbed power (right), HFS antenna, $f = 37.8$ MHz, $\nu = 5 \times 10^{-3}$. Vertical lines from left to right: deuterium cyclotron resonance, hybrid resonance, hydrogen cyclotron resonance.*

The low-field side launching of the wave results in a very different pattern. The plasma response frequency scan is now a succession of distinct maxima (Figure 4.30). These peaks are explained by the formation of eigenmodes as a result of the interaction between the incident fast wave and that reflected from the cutoff. The maxima come in pairs. As can be seen from the spatial structure of the wavefields, each pair corresponds to a different number of radial nodes ("radial wave number"); inside each pair the left and right peaks are eigenmodes with lower and higher "poloidal wave numbers" correspondingly (Figure 4.33).

For all these frequencies the power is damped on the low-field side of the hybrid resonance, with maximum absorption density near the center of plasma. One example at the frequency $f = 44.1$ MHz (peak 5) is presented in Figure 4.34. As expected, the cyclotron resonance does not affect the fast wave propagation, contrarily to the hybrid ion-ion resonance.

These calculations are in a very good qualitative agreement with the LION code results for a similar equilibrium. At these frequencies, the difference of the plasma models in the two codes does not play an important role. As opposed to the Alfvén range of frequencies, in the ICRF domain finite electron mass does not introduce any new propagating solution to the dispersion relation and the modification of the fast wave propagation is negligible.

An insight into the absorption mechanisms in the configurations with high- and low-field side antennae can be gained from the analysis of the absorbed power as a function of the ad hoc imaginary part ν introduced in the frequency in the dielectric tensor to avoid singularities. The character of this dependence is very different for high- and low-field side propagations, indicating different types of energy damping.

Once again, the calculations were done for two numerical resolutions as defined above. Ideally, for a pure resonant absorption mechanism, the plasma response should not depend on ν . In our case, for the high-field side, the absorbed power varies by $\sim \pm 10\%$ while ν changes from 10^{-3} to 10^{-2} , so this is the range of ν values where resonant absorption dominates over other mechanisms (Figure 4.35). As it was demonstrated in [56], this range depends on the numerical resolution; increasing the mesh size allows us to access

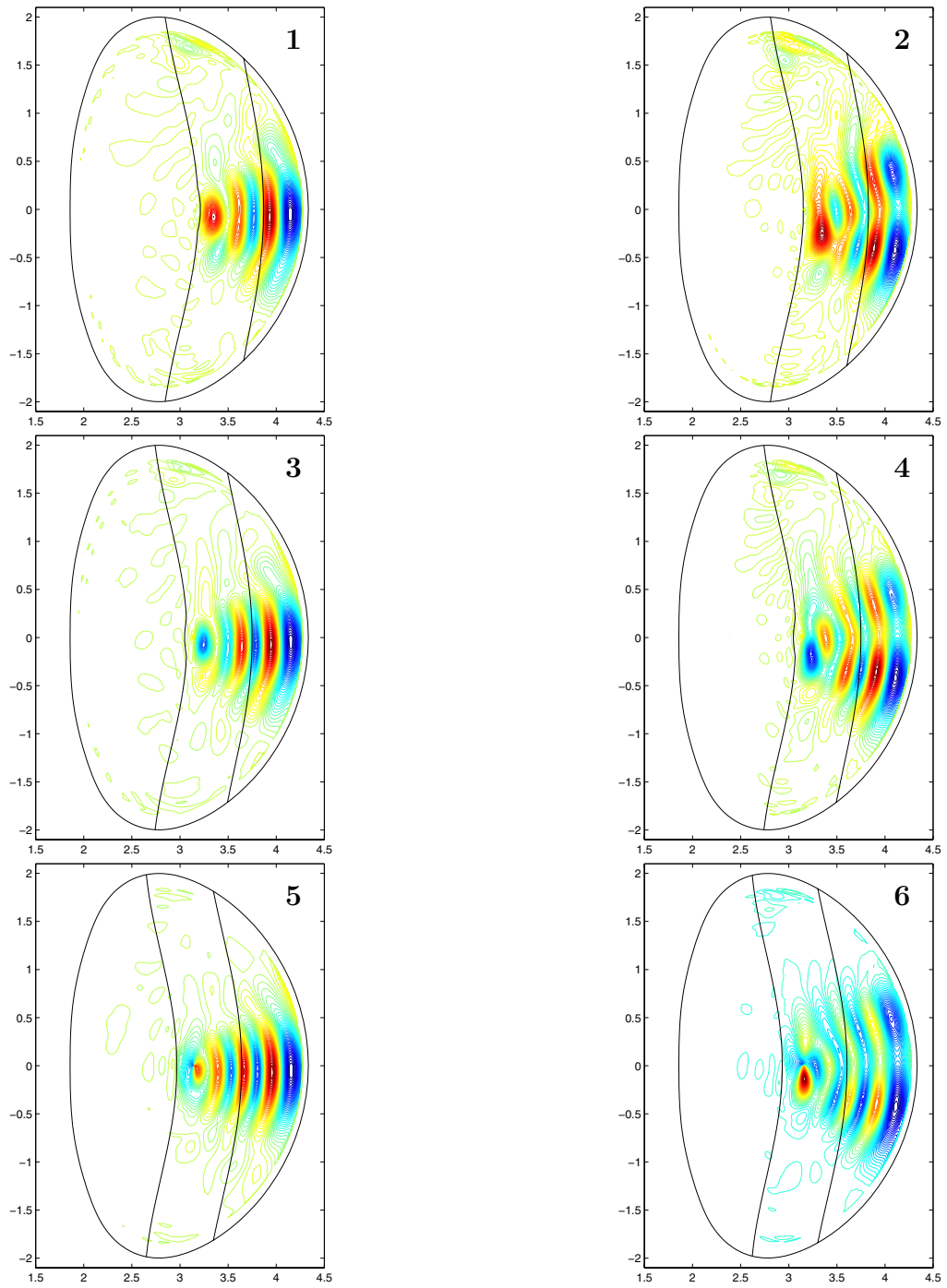


Figure 4.33. *Normal component of electric field, LFS antenna, fast wave eigenmodes (peaks 1-6 in Figure 4.30).*

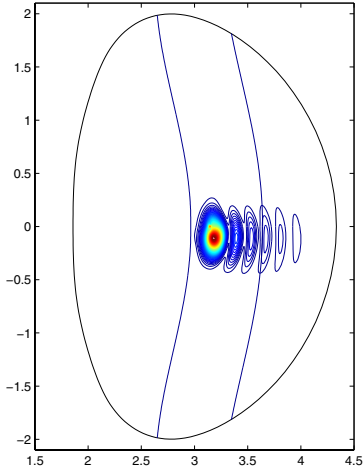


Figure 4.34. *Absorbed power density in the case of low-field side antenna, $f = 44.1$ MHz (peak 5 in Figure 4.33).*

smaller values of ν without introducing spurious numerical absorption. In our case, the results obtained for two different numerical resolutions start to deviate at $\nu \sim 10^{-3}$, so this value is an estimate of the lower limit for ν . When the imaginary part increases, at some point the direct damping of the incident wave starts to dominate over the resonant mechanism, so the absorbed power increases linearly with ν . In our case, it happens at $\nu \sim 5 \times 10^{-3}..1 \times 10^{-2}$. The reactive power, on the other hand, does not vary much, and remains constant within $\sim 2 \times 10^{-3}\%$ in the range $\nu \sim 1 \times 10^{-3}..1 \times 10^{-2}$ (dashed line in the Figure 4.35, right vertical axis).

Propagation from the low-field side shows a totally different pattern (Figure 4.36). For a frequency corresponding to an eigenmode ($f = 42.7$ MHz, peak 3 on Figure 4.30), the plasma response is approximately inversely proportional to ν in the range $\nu \sim 10^{-3}..10^{-2}$, which is characteristic for an eigenmode (note the similarity with the quasi-electrostatic wave absorption, Figure 4.26). Below this range, the numerical precision is not sufficient to correctly resolve the problem, so the absorption obtained with lower ν is wrong. Above $\nu \sim 10^{-2}$ the eigenmode absorption is competing with the direct damping of the incident wave, so the character of dependence changes. It is interesting to note that the absorbed power is almost independent of ν for $\nu \approx 10^{-2}..10^{-1}$, e.g in the range where ν becomes comparable or larger than the relative difference between the discretised eigenfrequencies $\Delta f/f \approx 0.03$. Then, the peaks are smoothed out by the large value of the damping

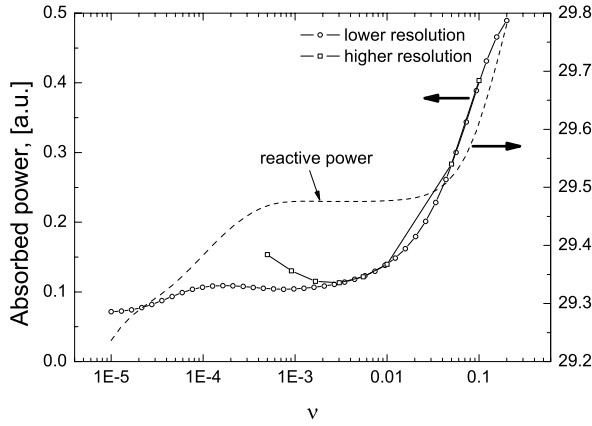


Figure 4.35. Normalised absorbed power as a function of imaginary part ν in the dielectric tensor in the case of high-field side antenna, $f = 43.0$ MHz (resonant absorption at the hybrid resonance).

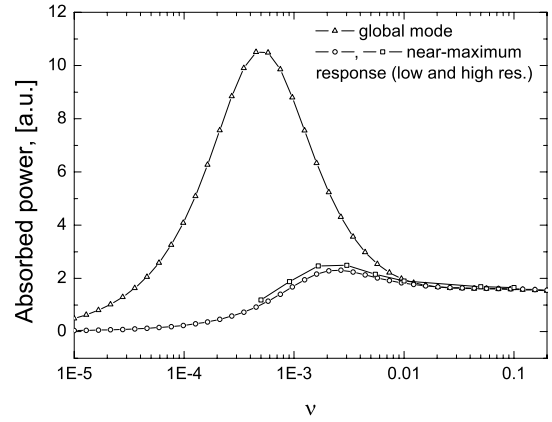


Figure 4.36. Normalised absorbed power as a function of ν for low-field side antenna. Triangles correspond to $f = 42.7$ MHz (peak 3 on Figure 4.33), circles and squares — $f = 43.0$ MHz (intermediate position between peaks 3 and 4).

parameter, the response becomes continuous and it is also a kind of resonant absorption.

The power balance for the calculations with different values of imaginary part ν is presented on Figure 4.37. In general, the relative error in energy balance decreases for higher values of ν . Here, the energy is well conserved for all of the above calculations, even for very low ν .

To briefly summarize the results presented above, we can confirm the conclusion obtained in Ref. [56]. The high-field side heating is usually considered to be more advantageous because of the almost 100% absorption of the incident wave on the hybrid resonance, but is difficult to implement because of technically complicated access to the inner part of the torus. However, even with technical difficulties apart, a "single-pass" absorption turns out not to be necessarily the most preferable scenario. A global study of the propagation problem shows that for the case of low-field side launching, the fast wave can form global eigenmodes, which strongly affect the energy coupling. In this case, the

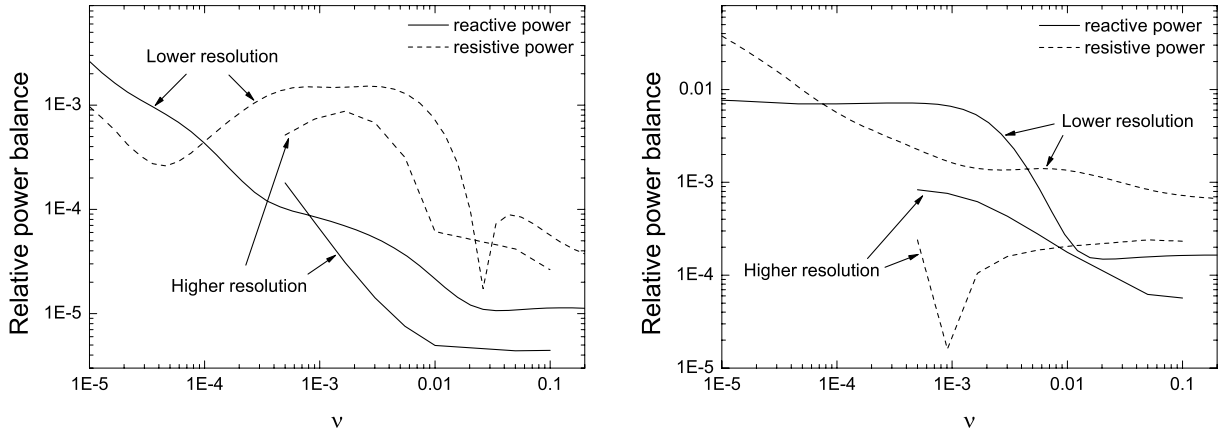


Figure 4.37. *Global power balance as a function of imaginary part in the frequency, reactive and resistive parts. Left: high-field side, right: low-field side antenna.*

absorbed power can be even higher than in the scenario with a high-field side antenna. To be more complete, a discussion about the absolute values of antenna coupling as well as about the deposition profiles and the distribution of heating power between electrons and different ion species should be based on calculations with a more sophisticated plasma model, taking into account finite temperature effects and physical resistivity, which goes beyond the scope of this work.

4.2.7 Mirror

To conclude the discussion of the wave propagation in 2D configurations, we will now briefly present the Alfvén spectrum in a mirror geometry. A pure mirror is an open configuration which cannot be exactly represented in the LEMan formulation, but we model it here by a large aspect ratio torus ($R/a \approx 100$) with superposed toroidally non-symmetric terms (“bumpy torus”).

This geometry is poloidally symmetric at zero order in a/R , so different poloidal harmonics are decoupled. This allows us to test the implementation of the toroidal coupling in the code in a simple 2D case, retaining only one poloidal mode. Coupling of toroidal harmonics has exactly the same effect on the Alfvén spectrum as we saw in the tokamak

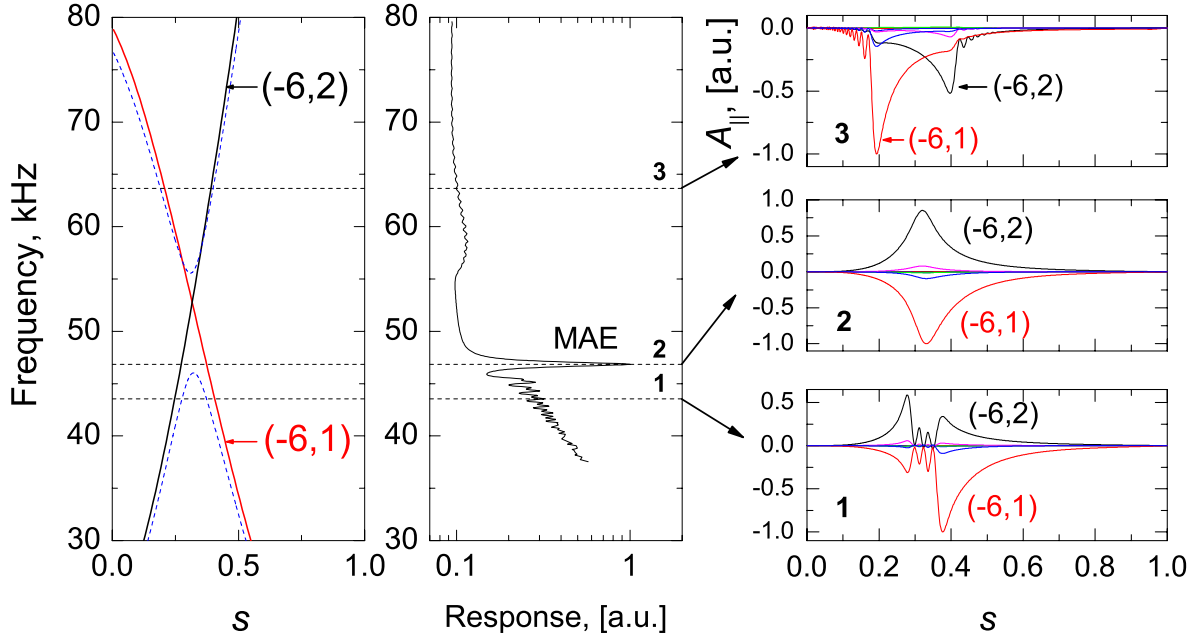


Figure 4.38. **Left:** Cylindrical branches of the Alfvén continuum (solid lines) and approximate positions of the Alfvén resonance in the mirror configuration (dashed lines), $R/a \approx 100$, 60 toroidal periods. Toroidal mode numbers per period are used. **Middle:** Frequency scan of the plasma response (normalised) in the gap region. **Right:** Wavefields (normalised $A_{||}$) for $f = 43.5$, 46.9 and 63.7 kHz. Toroidal mode-per-period notation is used.

geometry. Non-symmetric (0, 1) equilibrium terms open gaps in the Alfvén continuum at the intersection of the cylindrical continuum branches with different toroidal wavenumbers (Figure 4.38). A frequency scan of the plasma response in the gap region reveals a discrete eigenmode solution near the lower edge of the gap, this time it is a *mirror-induced Alfvén eigenmode* (MAE).

Mirror geometry provides a good case to verify the toroidal convergence of the results. As expected for the Fourier representation, power integrals converge approximately exponentially with the total number of toroidal Fourier modes, at a fixed number of poloidal harmonics and radial finite elements (Figure 4.39). Here, the convergence is defined as the relative difference $(P_{pla} - P_{pla}|_{N_n=23})/P_{pla}|_{N_n=23}$. Global power balance rapidly converges

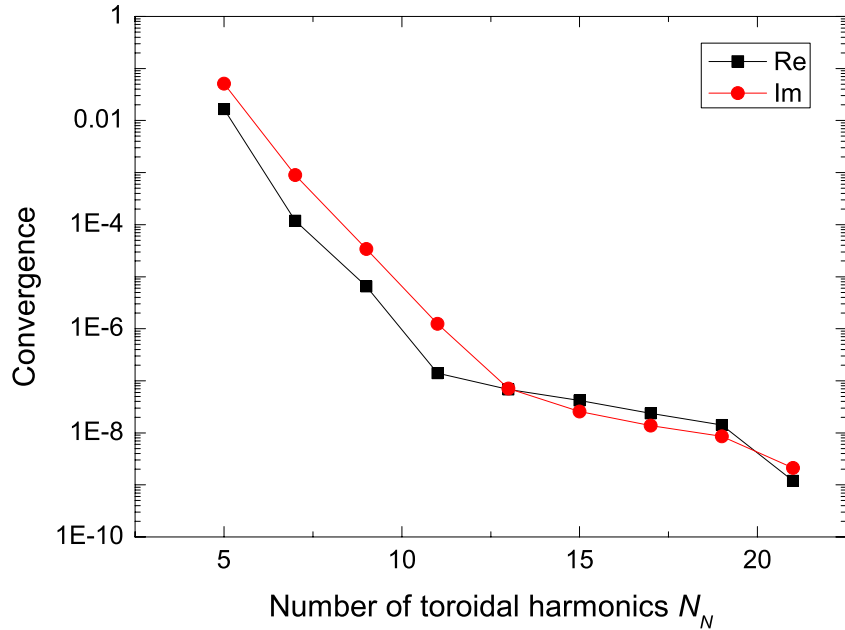


Figure 4.39. Convergence of the total absorbed (circles) and reactive (squares) powers with the number of toroidal perturbation harmonics. $N_s = 200$, $\nu = 6.5 \times 10^{-2}$.

with N_n to reach the value of $\delta_g = 1.5 \times 10^{-5}$ at $N_n = 11$.

The poloidal and toroidal mode couplings have thus been tested separately for relatively simple 2D configurations, and their effect on the low-frequency oscillation spectrum of plasma has been discussed. A fully 3D stellarator geometry includes both types of coupling simultaneously, which complicates both the computation and the interpretation of the results. In the next section, we will present results obtained for simplified and fully 3D geometries.

4.3 3D geometry

In this section, we will finally attack the full 3D problem of low-frequency wave propagation. First, to test the 3D stellarator-type coupling on a simple example allowing an easy result interpretation, we apply the code to a model 3D helical configuration with large aspect ratio. Alfvén continuum, gap structure and eigenmodes are discussed.

Then, a low-frequency spectrum of a fully 3D quasi-axisymmetric concept stellarator is analysed and compared to its cylindrical counterpart.

Finally, the code is applied to the LHD stellarator geometry. The plasma response exhibits the characteristic structure with gaps and eigenmodes. Wavefields at different frequencies are discussed, as well as the power deposition profiles.

4.3.1 Helix

Helical configuration provides an excellent case for testing stellarator-type coupling. On the one hand, in a geometry with pure helical symmetry, the results are much easier to interpret than in a realistic stellarator because the coupling is limited by the symmetry. The coupling actually affects only the modes on the same diagonal in a (m, n) matrix. Choosing helical antenna currents with only one set of (m, n) values one can single out only those modes in the (m, n) matrix that diagonally align with the antenna component. All the other harmonics do not contribute to the perturbed wavefields. This greatly facilitates the analysis of the plasma response and allows for a simple comparison with the cylindrical counterpart of the configuration.

On the other hand, the formulation of LEMan is independent from the helical or any other symmetry of the geometry, except for the toroidal periodicity. Despite the fact that using helical coordinates the configuration can be reduced to a 2D geometry, for our purposes it is a fully 3D problem. The code does not profit from the possible simplification and solves the equation in a large box of Fourier modes with different helicities. Thus, the three-dimensional structure of the code and the stellarator-type coupling can be tested without unnecessarily complicating the analysis of the results.

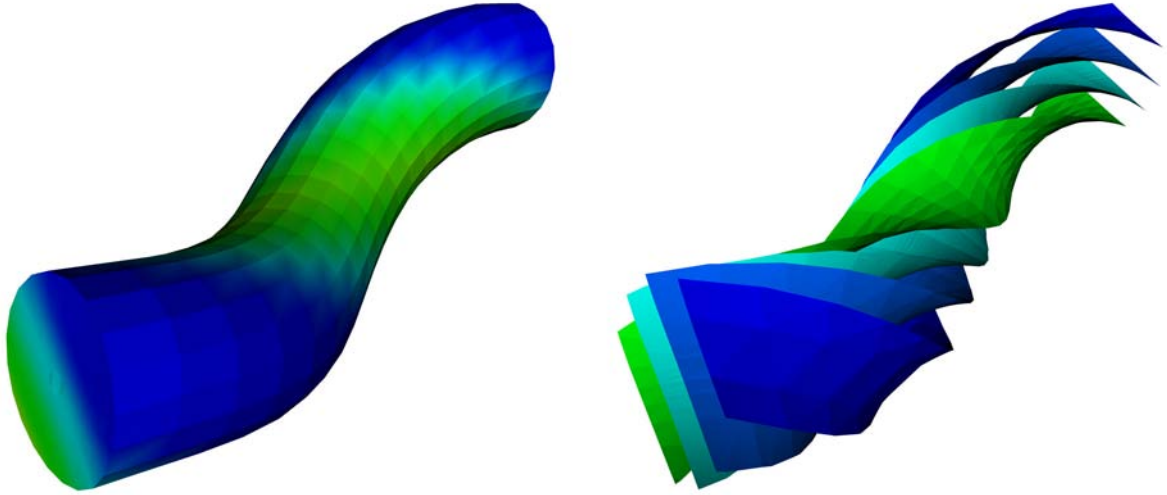


Figure 4.40. *Configuration with dominant helical terms. Aspect ratio $R/a \approx 100$, 60 toroidal periods. On the right: surfaces of constant equilibrium magnetic field.*

Just like for the mirror geometry in the section 4.2.7, we produce a helical configuration starting from a large aspect ratio torus ($R/a \approx 100$) and adding helical terms to it. The equilibrium has 60 toroidal field periods, the ι per period monotonically decreases from 1 on the axis to 0.33 at the plasma boundary, the plasma density is linear in s , thus, parabolic in r near the axis; $B_0 = 0.8$ T, $n_0 = 4.0 \times 10^{19}$ m $^{-3}$. Helical terms in the equilibrium have a dominating (1, 1) component, or, in a global notation in the toroidal direction, a (1, 60) component, which produces a helix with a circular cross-section and a non-planar axis (Figure 4.40). Not only $|\vec{B}_0|$ shown on the right, but also all the other equilibrium quantities have the same helical symmetry.

We now excite oscillations in this configuration in the range 30 kHz–140 kHz (Alfvén frequencies) with a simple helical antenna localised radially near the plasma boundary, with only one harmonic $(m_a, n_a) = (-5, 3)$ (or, in global notation, $(-5, 180)$. In the rest of this subsection, we will use mode-per-toroidal-period notation to avoid large n numbers). Due to the (1, 1) helical symmetry, the dominating perturbation modes that are excited satisfy the condition $m - m_a = n - n_a$. Below 140 kHz, only three cylindrical Alfvén continuum branches respond to this selection criterium (Figure 4.41).

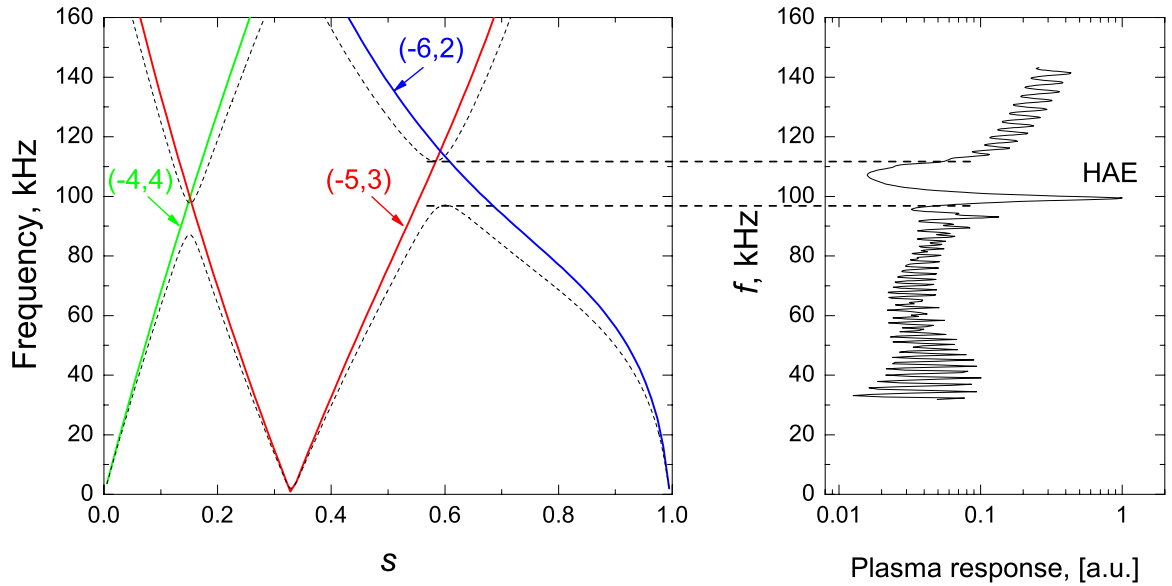


Figure 4.41. **Left:** Continuum Alfvén branches in a 1D cylinder with the same ι profile as in the helix (solid lines) and the same resonances with 3D equilibrium corrections (dashed lines). **Right:** Normalised plasma response.

A frequency scan of the plasma response confirms the expected mode coupling structure. A gap in frequencies is formed near the crossing of the cylindrical modes. This time, it is induced by the $(1, 1)$ equilibrium term. The peak residing in the gap at $f = 99.3$ kHz therefore corresponds to a *helicity-induced* Alfvén eigenmode, HAE. The gap formed due to the coupling between $(-6, 2)$ and $(-5, 3)$ harmonics and the corresponding eigenmode dominate the plasma response. The contribution of the gap and the eigenmode induced by the interaction between $(-5, 3)$ and $(-4, 4)$ harmonics is much smaller and is not visible on the plasma response.

An illustration of the Alfvén mode structure is shown in Figure 4.42 (left). The frequency of local Alfvén resonances is plotted here versus their radial position for the full helical geometry, taking into account 3D terms in the equilibrium and mode coupling. Not only the harmonics $m - m_a = n - n_a$, but also several neighbouring diagonals are included in this plot. These results are obtained using a code developed by Nicolas Mellet which is designed to calculate the Alfvén continuum branches in a 3D geometry

by directly searching the zeros of the dispersion function for the Alfvén wave [70]. The resonance positions are calculated using the full 3D expression for the k_{\parallel} operator, in the approximation $\omega \ll \Omega_i$. Resonance positions obtained with LEMan for several frequencies are denoted with cross markers.

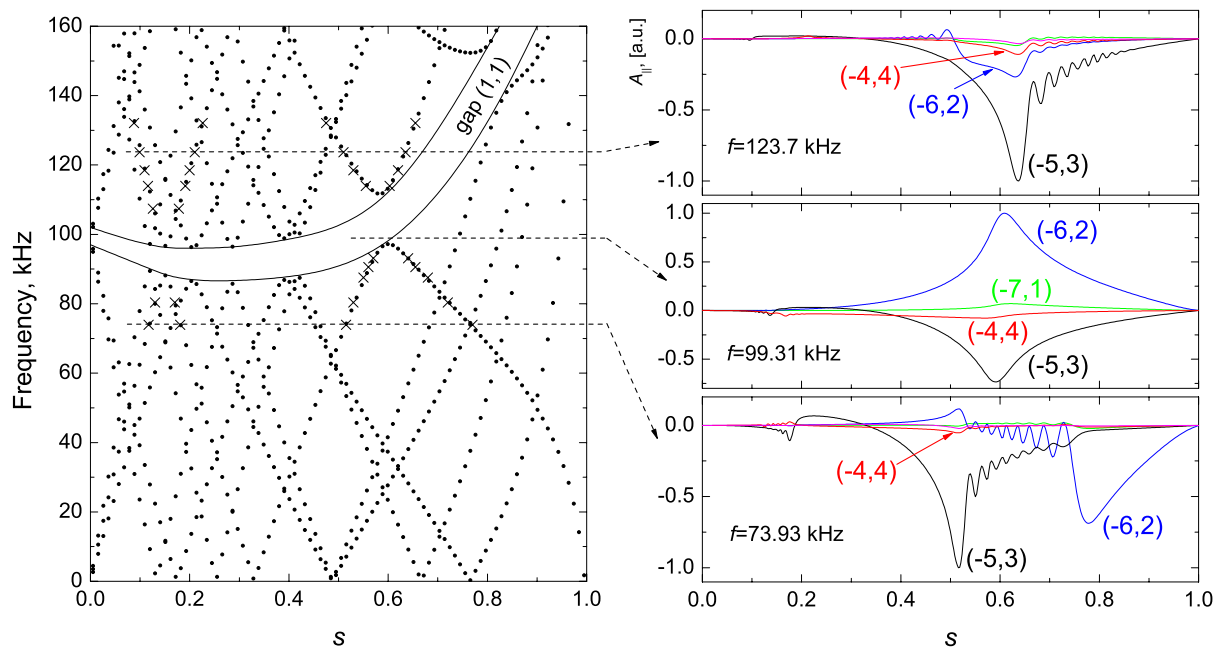


Figure 4.42. **Left:** Alfvén continuum and $(1,1)$ gap structure in the full helical geometry. Crosses — resonance positions obtained with LEMan. **Right:** Wavefields (normalised A_{\parallel}) at three frequencies; only dominating harmonics are shown.

The perturbed wavefields corresponding to several frequencies are shown on the right in Figure 4.42. At the eigenfrequency $f = 99.3$ kHz, the wavefields have a characteristic global structure with a maximum near the crossing of the cylindrical Alfvén branches. Below and above the gap the wavefields are dominated by the local Alfvén resonance and the resulting converted QEW wave.

The dominating harmonics are those that satisfy the selection condition $m - m_a = n - n_a$, but other modes are present as well because of the finite aspect ratio which

yields other types of coupling. These calculations were done with 100 radial elements and 54 Fourier harmonics mostly aligned along the diagonal passing through (m_a, n_a) , very similar to the table shown in Figure 3.2. Grouping the modes in the direction of dominating coupling helps to reach the desired convergence using less computational resources (these calculations require ~ 2 Gb of memory and ~ 150 seconds of CPU time for one frequency). The power balance for these results is very well satisfied: the precision of the local balance on each magnetic surface is $\lesssim 2 \times 10^{-3}$ (both for the reactive and the resistive parts), the global energy is conserved with the excellent accuracy of $\lesssim 10^{-6}$ for the reactive part and $\lesssim 10^{-11}$ for the resistive part.

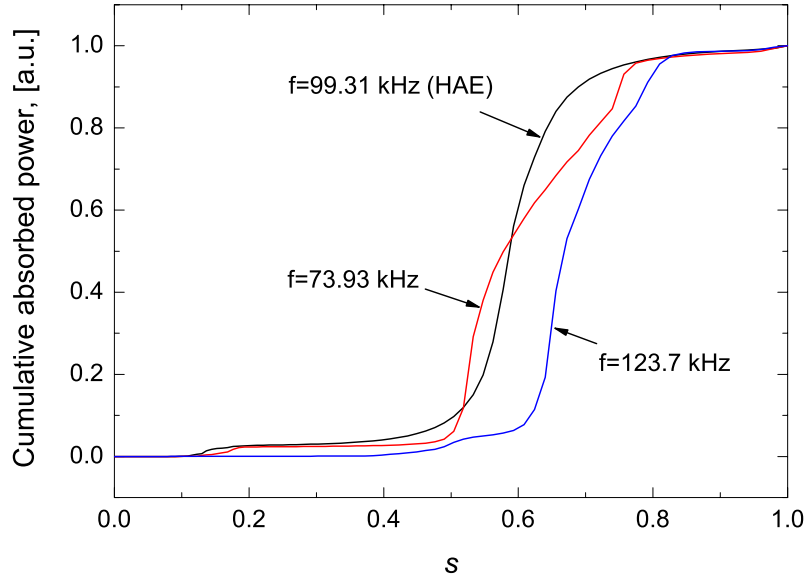


Figure 4.43. *Cumulative integral of absorbed power (normalised to the maximum value for each frequency) versus radial position.*

The integrals of the absorbed power Eq. (3.27) for each magnetic surface for the same frequencies as the wavefields in Figure 4.42 are shown in Figure 4.43. The axis does not present any unphysical energy sink. This confirms that the formulation of the numerical scheme in LEMan near the origin works correctly for this 3D configuration with a non-planar magnetic axis.

4.3.2 Quasi-axisymmetric device

We will now consider low-frequency oscillations in a fully 3D stellarator geometry, based on a *quasi-axisymmetrical* (QAS) stellarator concept. The QAS stellarator designs constitute one of the recently discovered paths [71–75] to improve the confinement properties of the classical stellarators, which were previously of significant concern due to the expected high losses of the α -particles and large diffusion coefficients of the thermal particles. These losses are associated with trapping of particles between the regions of high magnetic field strength and subsequent drifts across the field lines due to field gradients and curvature. An arbitrary 3D configuration is, potentially, more likely to create these regions of particle trapping because of the complicated geometry of the magnetic field. The recently proposed concept of advanced stellarators is based on exploiting the possible symmetries of the $|\vec{B}_0|$ topology, still retaining the 3D geometry of the magnetic surfaces. Thus, the advantages of the classical stellarator (reduced need for externally driven plasma currents, no disruptions, potentially higher plasma densities) and the tokamak confinement properties can be combined to reduce the neoclassical transport in advanced stellarators to near-tokamak level. The idea of a QAS device is to create a three-dimensional configuration with a two-dimensional axisymmetric (or near-axisymmetric) topology of the magnetic field strength in flux coordinates, like that of tokamaks (Figure 4.44).

However, as far as the Alfvén modes are concerned, the quasi-axisymmetry of the geometry does not at all simplify the oscillation spectrum. Different toroidal modes do interact to form gaps and eigenmodes because the coupling is defined not only by the topology of the $|\vec{B}_0|$, but by all the metric coefficients, which are not quasi-axisymmetric. Therefore, fully 3D calculation tools are required for the wave propagation analysis.

The configuration to be discussed in this section is based on the QAS geometry with the following parameters: aspect ratio $R/a \approx 3.5$, two toroidal field periods, $B_0 = 0.8$ T, $n_0 = 4.0 \times 10^{19} \text{ m}^{-3}$, oscillations excited by a helical antenna with $(m_a, n_a) = (-6, 2)$.

The low-frequency oscillation spectrum of this configuration has a very complicated structure. Due to both poloidal and toroidal dependencies in the equilibrium, virtually all

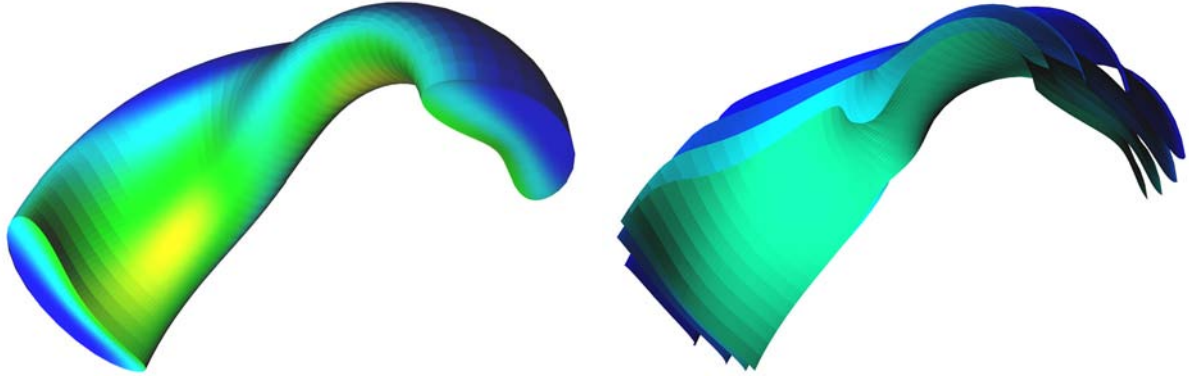


Figure 4.44. *One of the two toroidal periods of the QAS configuration with aspect ratio $R/a \approx 3.5$. **Left:** external magnetic surface geometry. **Right:** Several surfaces of constant equilibrium magnetic field, approximately axisymmetric in flux coordinates.*

the harmonics are coupled. Even for a simple antenna with only one mode, a large number of poloidal and toroidal harmonics are excited and contribute to the plasma response, considerably complicating the analysis. In this configuration, the gaps are "closed", so for any perturbation frequency there is a resonant surface of one (or several) continuum branches. Eigenmodes still exist, but they are less visible on the frequency scan because they are embedded in the Alfvén continuum and are harder to identify.

The plasma response in the interval $10 \text{ kHz} \leq f \leq 80 \text{ kHz}$ is presented in Figure 4.45. An example of the perturbed wavefields at one antenna frequency $f = 48.5 \text{ kHz}$ is shown on the right. The picture looks very complicated, but, surprisingly, close parallels can be drawn with the cylindrical counterpart of this configuration (i.e. a cylinder with the same ι profile). The corresponding cylindrical Alfvén continuum branches are plotted in the left figure. We see that the cylindrical branches $(-9,4)$ and $(-7,2)$ cross at $s \approx 0.73$, which is close to the surface of maximum amplitude of these modes at this frequency in the QAS. Three cylindrical branches $(-2,0)$, $(-2,2)$ and $(-10,4)$ cross at $s \approx 0.3$, which, again, is very close to the surface where these modes have maximum values. We have

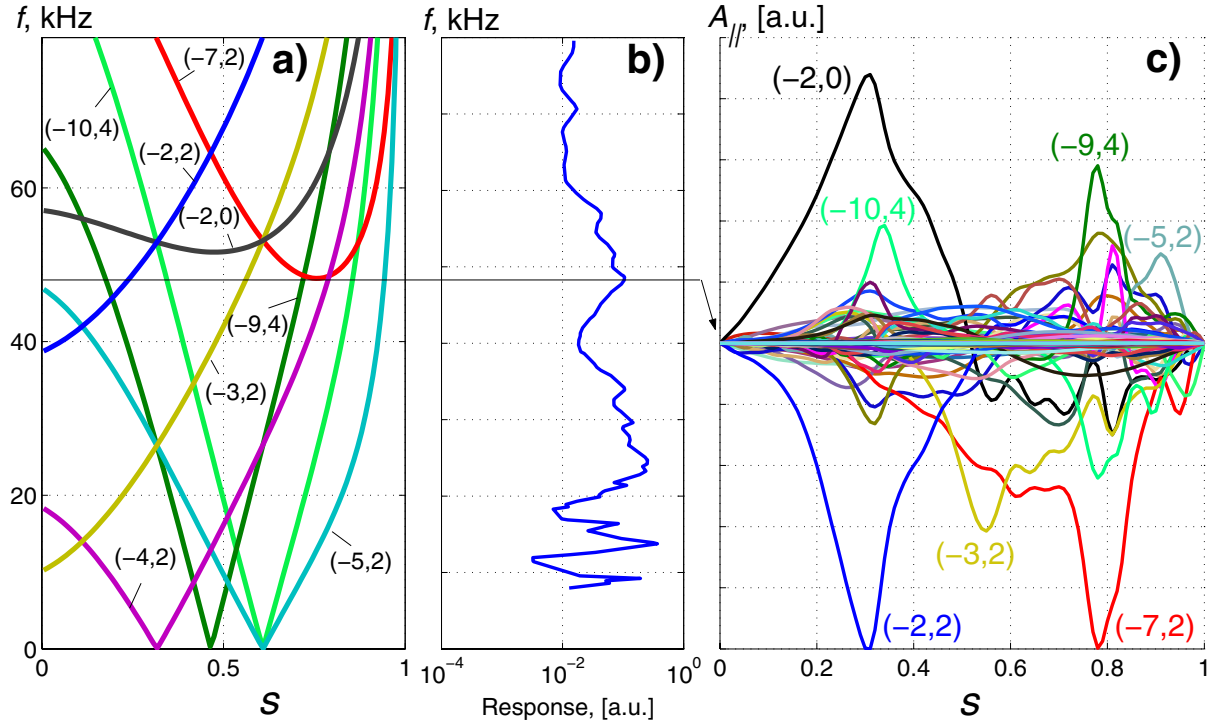


Figure 4.45. **a)** Alfvén continuum structure for a cylinder with the same i profile as the QAS, **b)** Normalized plasma response, **c)** Parallel component of the perturbed \vec{A} ([a.u.]) at $f=48.5$ kHz. Only dominant Fourier harmonics are shown.

already seen a very similar picture in other, simpler, configurations, when the coupled mode wavefields reach maximum values near the radial position where the intersection of the corresponding cylindrical branches would be. Also, the $(-3,2)$ mode in the QAS appears to have an Alfvén resonant surface at $s = 0.55$ where it is converted to the QEW wave propagating outwards, i.e. very close to its cylindrical position.

Thus, even for this fully 3D configuration with complex couplings, a comparison with its cylindrical analogue can help to identify the main modes and is very useful.

4.3.3 Large Helical Device

The Large Helical Device (LHD) in Japan is the largest new operating fusion facility. This stellarator with two helical wound superconducting coils is designed to demonstrate

disruption-free steady-state operation at a performance that allows extrapolation to a burning plasma experiment. The configuration has 10 toroidal field periods, major radius $R_0 = 3.9$ m, average minor radius of plasma $a = 0.50 - 0.65$ m, total plasma volume $V_p = 20 - 30$ m³, magnetic field in the plasma center $B_0 \approx 3$ T, total heating power $P = 30$ MW, $t_{pulse} = 10$ s $-\infty$. The performance of LHD is comparable to that of the present tokamaks: it reaches electron and ion temperatures $T_e \approx 10$ keV and $T_i \approx 5$ keV respectively, a plasma to magnetic energy ratio $\beta > 3\%$ at a pulse length of approximately 2 minutes. The geometry of the LHD plasma was used for the scheme in Figure 2.1.

The cylindrical branches of the Alfvén continuum and the plasma response to a $(-7, 10)$ antenna excitation in the frequency range 0.1 – 0.6 MHz are shown in Figure 4.46. In this 3D configuration, all couplings are possible, but the low-frequency

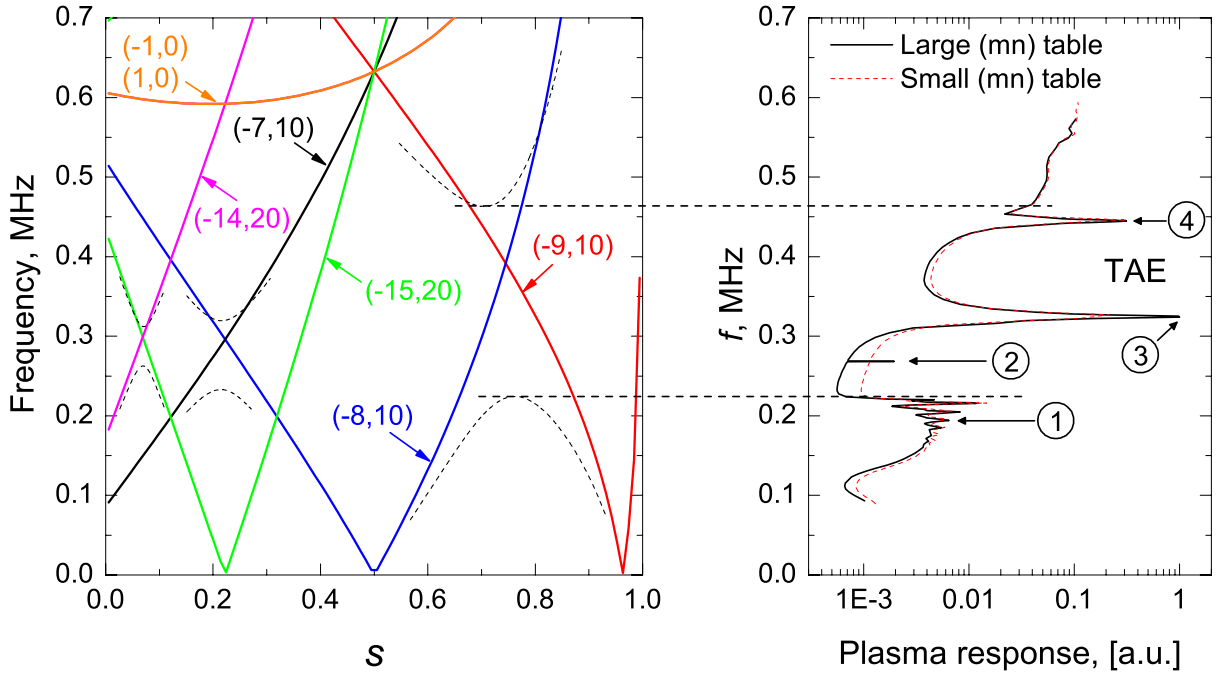


Figure 4.46. **Left:** Cylindrical Alfvén continuum branches (solid lines) and gaps near the crossings in the LHD geometry (dashed lines). **Right:** Normalised plasma response calculated for two sizes of perturbation harmonic table. Wavefields for frequencies 1–4 are shown in the Figure 4.47.

spectrum is mainly defined by the toroidal coupling. Once again, we see the characteristic structure of the gap between $f \approx 0.23$ and 0.46 MHz induced by the $(1, 0)$ equilibrium terms, and a clear eigenmode (TAE) generated by the coupling of $(-9, 10)$ and $(-8, 10)$ perturbation harmonics.

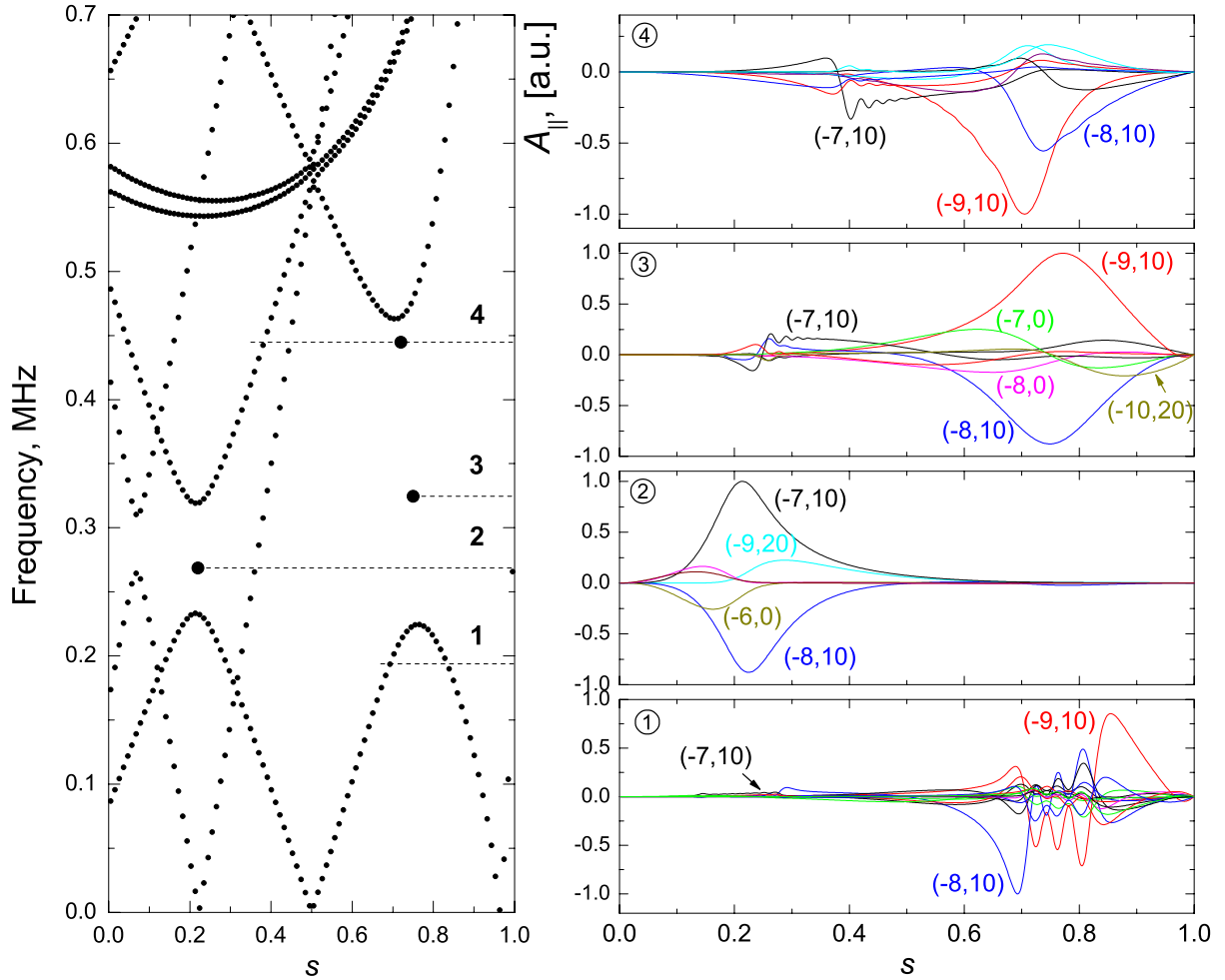


Figure 4.47. **Left:** Alfvén continuum structure in the full 3D LHD geometry. **Right:** Wavefields (normalised $A_{||}$) at the frequencies marked 1–4 in Figure 4.46; only dominating harmonics are shown.

A look at the wavefields (Figure 4.47) helps to identify the peaks in the plasma response. Below the gap (example "1", $f = 0.194$ MHz), the dominating effect is the conversion to the QEW, so the fast oscillations of the plasma response below $f \approx 0.23$ MHz are

produced by the eigenmodes of the QEW confined between two resonant surfaces. The small peak denoted "2" ($f = 0.269$ Mhz) corresponds to the TAE mode formed by the interaction of $(-8, 10)$ and $(-7, 10)$ modes with the maximum amplitude near $s = 0.22$, the crossing of the cylindrical branches. Peak "3" ($f = 0.325$ Mhz) is the dominating TAE formed by $(-9, 10)$ and $(-8, 10)$ harmonics. For the peak "4" ($f = 0.445$ Mhz), the dominating mode numbers and the character of the wavefields indicate that it probably corresponds to a second TAE mode residing in the same gap and produced, again, by the interaction of $(-9, 10)$ and $(-8, 10)$ harmonics.

As a final remark about the spectrum, we note the difference between the behaviour of the $(-1, 0)$ and $(1, 0)$ branches in the cylindrical approximation and in a 3D geometry. For a cylindrical k_{\parallel} expression ($k_{\parallel} = (n + im)/R$), both modes have the same frequency (Figure 4.46, left). In a 3D geometry, the symmetry breaking removes this degeneracy and the modes become separated (Figure 4.47, left).

Power absorption profiles for the frequencies "1" – "4" are shown in Figure 4.48. At the frequency in the continuum spectrum part ($f_1 = 0.194$ MHz) the energy is mostly damped by the QE wave propagating between two Alfvén resonant surfaces. For the

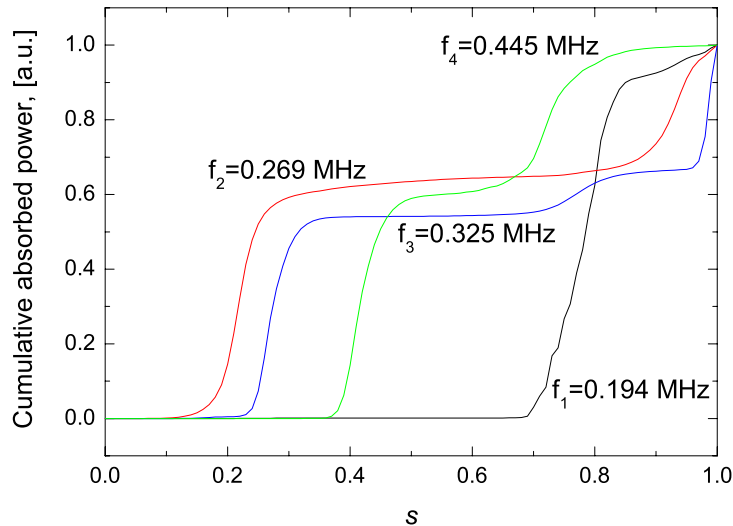


Figure 4.48. *Cumulative integral of absorbed power (normalised to the maximum value for each frequency) the versus radial position.*

(almost) pure TAE mode at $f_2 = 0.269$ MHz the power is mostly absorbed near the region of localisation of the eigenmode, i.e. near $s \approx 0.22$. The mode with the maximum absorption, the TAE at $f_3 = 0.325$ MHz, resonates with the local continuum branch dominated by $(-7, 10)$ harmonic and so is strongly absorbed through the local Alfvén resonance and the converted QEW. Note that the power deposition position for this mode differs from the TAE localisation region; it shifts closer to the plasma core, near $s \approx 0.24$. This situation could potentially be interesting for heating purposes. However, we should not forget that the cold plasma model cannot correctly answer the question of the radial distribution of the energy absorption. To get a more realistic picture of damping, a kinetic plasma model is required.

These calculations are performed with 100 radial elements and 135 Fourier harmonics selected according to the directions of dominating couplings in such a way that the amplitudes of the perturbed modes on the edge of the (m, n) table do not exceed 0.5% of the maximum mode amplitude. Runtime on the SX5 machine is about 1600 seconds for one frequency using ≈ 12 GB of memory. In Figure 4.46 (right), the dashed line shows the plasma response calculated for a smaller table of perturbation harmonics, $N_{mn} = 107$. These results are still reasonably converged, the frequency scan recovers the main features of the spectrum. However, it fails to reproduce the $(-8, 10) - (-7, 10)$ eigenmode (peak "2"), so in this sense $N_{mn} = 107$ is not sufficient.

The results obtained with $N_{mn} = 135$ are well converged. The axis treatment ensures a correct representation of the solution near the origin; the relative error of the unicity for the potentials and fields is very small ($\leq 6 \times 10^{-6}$); there is no unphysical energy sink on the axis. The energy is well conserved. The local power balance on each surface is satisfied within $\sim 5\%$, the global balance, as before, has a much better precision: $\delta_g \approx 5 \times 10^{-4}$. This precision is lower than that obtained here previously for simpler configurations due to the complexity of the 3D stellarator equilibrium and the arising couplings. It is nonetheless still good enough for the Alfvén mode studies, validating the applicability of the LEMan code in a fully 3D realistic stellarator geometry using relatively modest computational resources by 3D simulation standards.

Chapter 5

Conclusions

In the present work, we have developed a new full-wave code LEMan for the solution of the linearised set of Maxwell's equations in a general 3D stellarator geometry. The code determines small-amplitude perturbations in a plasma excited by an external antenna. The global solution to the wave equation is found without any assumption on the wavelength and accounts for all 3D geometrical effects. The wave equation is formulated in terms of the electromagnetic potentials in order to avoid the effect of numerical pollution. The continuous problem is discretised using linear or Hermite cubic finite elements in the radial direction and Fourier decompositions in the poloidal and toroidal angles. Special care is taken to treat the magnetic axis region and to assure the global and local energy conservation. The formulation of LEMan is implemented in the Boozer magnetic coordinate frame. The initial underlying equilibrium is produced by the VMEC code, the mapping to the Boozer coordinates is performed by the TERPSICHORE code. The full cold plasma model is implemented for the wave-plasma interaction description.

The code has been applied and verified in 1D, 2D and 3D geometries. The convergence properties of the code have been studied in detail, confirming the expected scaling of the error measure with the size of discretisation. No unphysical spurious solutions have been observed in the oscillation spectrum.

Low-frequency wave propagation in the Alfvén frequency range in configurations with different symmetries has been analysed. The code successfully reproduces all the funda-

mental properties of the Alfvén spectrum. Gaps in the Alfvén continuum and the corresponding eigenmodes (TAE, EAE, MAE, HAE) have been demonstrated in tokamak, mirror, helical and realistic 3D stellarator geometries. We have successfully benchmarked LEMan against results of the LION code. Also, calculations with LEMan for the TAE frequency have been shown to be in a good agreement with measurements of low-frequency plasma oscillations in the JET tokamak. These results also provide an additional comparison with the 2D kinetic NOVA-K code. In tokamak and stellarator geometries, a scenario with damping of a global mode energy through a local shear Alfvén resonance has been presented. A calculation of the exact radial distribution of absorbed power, however, requires an implementation of a more sophisticated plasma model. Mode conversion to the quasi-electrostatic wave has been studied, and eigenmodes of the QEW in the continuous part of the Alfvén spectrum have been found.

The code has also been applied in the ion cyclotron frequency range in JET tokamak geometry. Wave propagation and absorption have been studied for a two ion species plasma in the presence of the ion-ion hybrid resonance for low- and high-field launching antennas. While high-field heating in this case is characterised by a 100% single pass absorption of the incident wave at the hybrid resonance, the low-field antenna spectrum has a structure with multiple maxima representing the eigenmodes of the fast wave. Due to these eigenmodes, the absorbed power can be even larger than for the high-field launching, but, again, this discussion requires that finite temperature effects be taken into account.

The energy conservation has been demonstrated to be very well satisfied, even for complicated 3D geometries. The discretisation size required for a good power balance in a 3D stellarator in the Alfvén range of frequencies is already near the limit of the computational resources accessible on a single processor. For ICRF studies in stellarators, parallelisation will be required, as well as splitting the matrix into smaller pieces.

The applicability of LEMan to fully 3D stellarator geometry has thus been verified. The code provides a solution to the 3D wave propagation problem with very limited computational resources for a 3D numerical tool. The matrix construction time takes only a small fraction of the total runtime, therefore, potentially, a more sophisticated plasma

model can be implemented without considerably increasing the CPU time requirements. LEMan can serve as a solid basis for the future extension of the plasma model and be coupled to other codes, for example the 3D particle drift orbit code VENUS which also utilises the electromagnetic potential formulation.

Appendix A

Numerical pollution

As it was noted in the chapter 2, numerical pollution of the spectrum is a very important effect to consider when solving Maxwell's equations. In fact, this problem can appear not only for the wave equation, but for any Helmholtz equation of the type

$$-\Delta u - k^2 u = f.$$

If no special care is taken to avoid it, these equations are known to sometimes lead to spurious numerical solutions. To be complete, we feel it useful to give here a more detailed description of how this effect can introduce unphysical numerical solutions in application to our problem [15].

An illustration of the spectral pollution can be easily demonstrated in 1D slab geometry in vacuum. Without loss of generality, we direct the axes so that only two components of the wavevector remain, k and k_z . The solution to the discretised wave equation can then be compared to the exact dispersion relation $\omega^2/c^2 = k^2 + k_z^2$.

The discretised homogeneous wave equation formulated in terms of electric field or E/M potentials can be written in the matrix form

$$\hat{M} \cdot X = 0. \tag{A.1}$$

It is very similar to the equation (3.14), but now X stands for either the unknown electric field components for the field formulation, or the E/M potentials for the potential

formulation. We will look for a solution in the form of a plane wave

$$X_j = X_0 e^{ikx_j},$$

where $x_j = jh$, $j \in N$ is a homogeneous mesh. Finite element discretisation with localised functions in the x direction assures that all matrix elements M_{ij} vanish for $|i - j| > 1$. For linear FE, M_{ij} is just one number, for Hermite cubic interpolation functions each M_{ij} is a 2×2 matrix. The discretised dispersion relation in a boundless 1D slab can then be formulated as

$$\left(\hat{M}_{j,j-1} + \hat{M}_{j,j} + \hat{M}_{j,j+1} \right) \cdot X_0 e^{ikx_j} = 0, \quad \forall j \in N. \quad (\text{A.2})$$

A non-trivial solution of Eq.(A.2) exists if the determinant of $\hat{M}_{j,j-1} + \hat{M}_{j,j} + \hat{M}_{j,j+1}$ is zero. This equation can be solved for ω analytically using symbolic manipulation software like Maple or Mathematica (otherwise, it results in very long tedious calculations, especially for cubic finite elements).

The parallel refractive index $F = \omega / ck_z$ of the discretised solution compared to the exact solution for the wave equation formulated in terms of the electromagnetic potentials

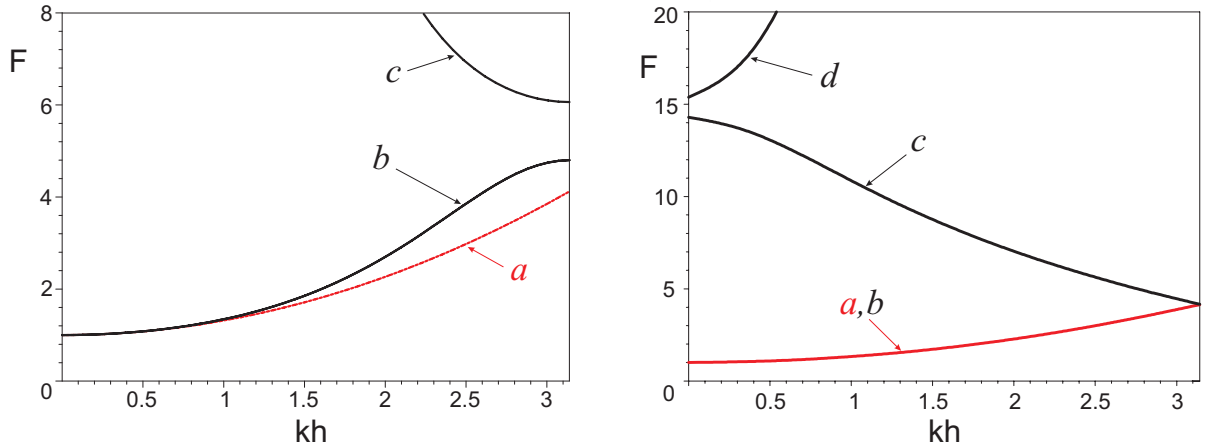


Figure A.1. *Parallel refractive index $F = \omega / ck_z$ of the discrete solution of the potential formulation of the wave equation as a function of kh . **Left:** Linear finite elements. (a) – exact solution, (b, b, c) – numerical solutions. **Right:** Hermite cubics. (a) – exact solution, (b, b, c, c, d) – numerical solutions.*

is plotted in Figure A.1. The arbitrary parameters k_z and h are set to $k_z = 1.414$ and $h = 2\pi/5 = 1.26$.

On the left plot numerical results are shown for the linear finite elements. Branch (b) is a numerical approximation to the exact solution (a) and converges to it at high numerical precision $kh \rightarrow 0$. It can be verified that the root (c) does not satisfy the Coulomb gauge condition $\nabla \cdot \vec{A} = 0$ and cannot be excited when the divergence of \vec{A} is set to zero on the boundary. For Hermite cubic discretisation (right plot), the approximation to the numerical solution (b) is very close to the exact dispersion relation (a). Again, the two remaining branches (c) and (d) cannot be excited if the gauge is imposed on the boundary. In the scheme with the potential formulation of the wave equation, no solution is possible that is not an approximation to the exact dispersion relation, therefore this approach is pollution-free.

The situation is different for the field formulation of the wave equation (Figure A.2). In case of linear FE, several numerical solutions exist at low resolution (large kh), one of

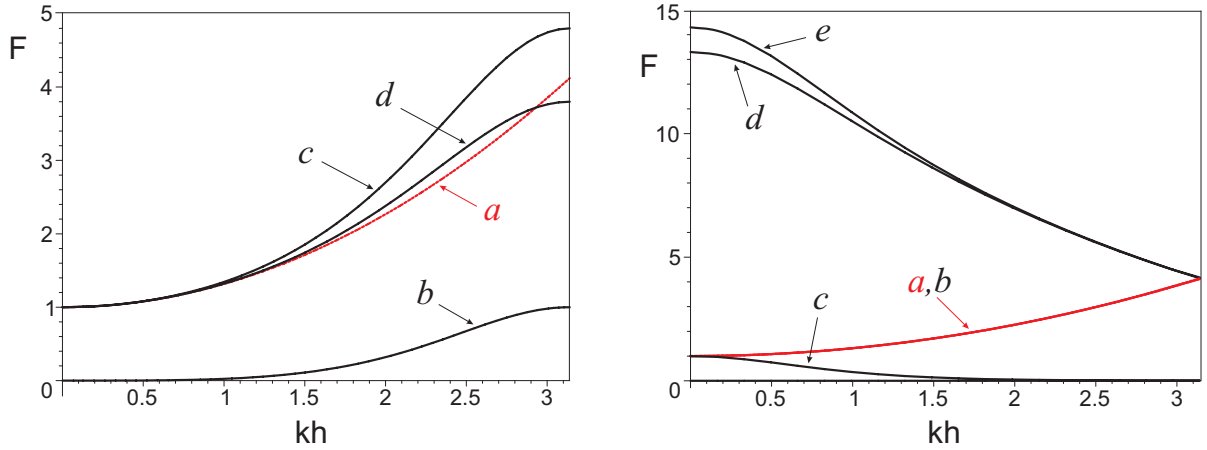


Figure A.2. *Parallel refractive index $F = \omega/c k_z$ of the discrete solution of the wave equation formulated in terms of the electric field versus the discretisation precision kh .*

Left: *Linear finite elements. (a) – exact solution, (b, c, d) – numerical solutions.*

Right: *Hermite cubics. (a) – exact solution, ($F \equiv 0$, b, c, c, d, e) – numerical solutions.*

them (b) does not converge to the exact dispersion relation (a) with decreasing mesh step. The situation does not improve for cubic FE. The electric field formulation still allows for unphysical solutions. This time, the spurious (c) branch appears below the cut-off at frequencies comparable to the exact dispersion relation, which makes it hard to filter from the exact solution.

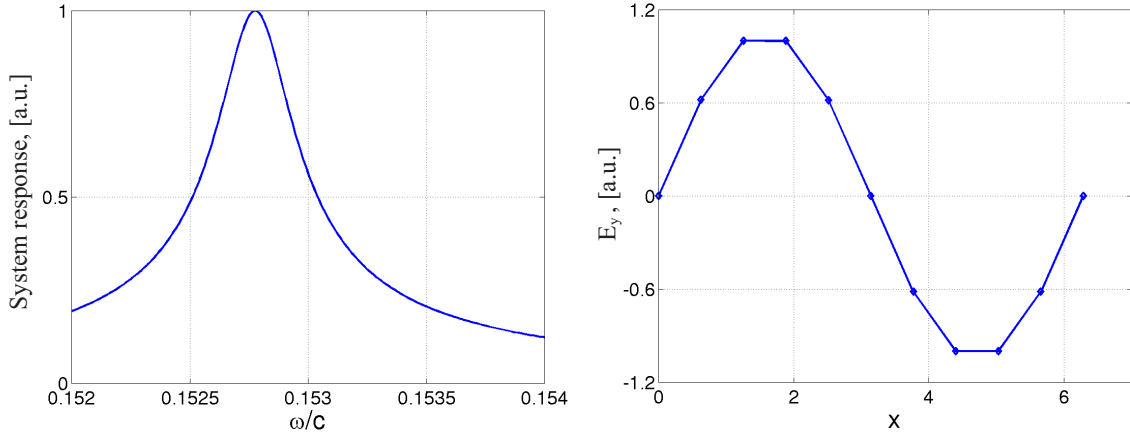


Figure A.3. *Illustration of the numerical pollution in field formulation discretised with linear finite elements. Left: Frequency scan of the system response to external excitation with an unphysical maximum. Right: Wavefield of the spurious solution.*

A simple illustration to the spectrum pollution is shown in Figure A.3. The wave equation in field formulation is resolved with linear finite elements on a mesh with $N = 10$ intervals; $h = 2\pi/N = 0.628$. This time, the 1D vacuum slab is bounded so that k components of the solution are fixed: $k_x = k_y = k_z = 1$. The exact dispersion relation is satisfied at $\omega/c = \sqrt{k_x^2 + k_y^2 + k_z^2} = 1.73$. However, not only this solution is present in the oscillation spectrum, but also a spurious branch. A frequency scan of the system response reveals an unphysical peak at $\omega/c \approx 0.153$. The wavefield corresponding to this solution looks totally regular, so it is hard to discriminate from the approximation to the true solution of the continuous problem.

Appendix B

Derivation of transformation matrices \widehat{TU} , \widehat{TL}

Expansion of the wave equation and matrix element construction is done using the transformation matrices \widehat{TU} , \widehat{TL} introduced in Eqs.(3.9), (3.10). Multiplying the orthogonal representation of \vec{A} by the contravariant basis vectors, we obtain the expressions for the contravariant components of \vec{A} :

$$\begin{aligned}\vec{A} &= A_n \frac{\nabla s}{|\nabla s|} + A_b \frac{\vec{B} \times \nabla s}{B|\nabla s|} + A_{\parallel} \frac{\vec{B}}{B}, \\ A^s &= \vec{A} \cdot \nabla s = A_n |\nabla s|, \\ A^\theta &= \vec{A} \cdot \nabla \theta = A_n \frac{\nabla s \cdot \nabla \theta}{|\nabla s|} + A_b \frac{(\vec{B} \times \nabla s) \cdot \nabla \theta}{B|\nabla s|} + A_{\parallel} \frac{\vec{B} \cdot \nabla \theta}{B}, \\ A^\phi &= \vec{A} \cdot \nabla \phi = A_n \frac{\nabla s \cdot \nabla \phi}{|\nabla s|} + A_b \frac{(\vec{B} \times \nabla s) \cdot \nabla \phi}{B|\nabla s|} + A_{\parallel} \frac{\vec{B} \cdot \nabla \phi}{B}.\end{aligned}$$

Substituting \vec{B} in its covariant or contravariant form in Boozer coordinates (2.11) yields

$$\begin{aligned}
(\vec{B} \times \nabla s) \cdot \nabla \theta &= -\frac{I(s)}{\sqrt{g}}, \\
(\vec{B} \times \nabla s) \cdot \nabla \phi &= -\frac{J(s)}{\sqrt{g}}, \\
\vec{B} \cdot \nabla \theta &= \nabla \phi \times \nabla s \cdot \nabla \theta \quad \psi'(s) = \frac{\psi'}{\sqrt{g}}, \\
\vec{B} \cdot \nabla \phi &= \nabla s \times \nabla \theta \cdot \nabla \phi \quad \Phi'(s) = \frac{\Phi'}{\sqrt{g}},
\end{aligned}$$

and so we immediately obtain the \widehat{TU} matrix coefficients:

$$\widehat{TU}(s, \theta, \phi) = \begin{pmatrix} |\nabla s| & 0 & 0 \\ \frac{\nabla s \cdot \nabla \theta}{|\nabla s|} & -\frac{I}{B|\nabla s|\sqrt{g}} & \frac{\psi'}{B\sqrt{g}} \\ \frac{\nabla s \cdot \nabla \phi}{|\nabla s|} & -\frac{J}{B|\nabla s|\sqrt{g}} & \frac{\Phi'}{B\sqrt{g}} \end{pmatrix}.$$

The \widehat{TL} matrix elements can be obtained, for example, by applying the transformation from contravariant to covariant form using the metric elements g^{ij} . The final expression for \widehat{TL} after simplifications is written as:

$$\widehat{TL}(s, \theta, \phi) = \begin{pmatrix} \frac{1}{|\nabla s|} & -\frac{g_{s\theta}I + g_{s\phi}J}{B|\nabla s|\sqrt{g}} & \frac{g_{s\theta}\psi' + g_{s\phi}\Phi}{B\sqrt{g}} \\ 0 & \frac{\Phi'|\nabla s|}{B} & \frac{J}{B} \\ 0 & -\frac{\psi'|\nabla s|}{B} & -\frac{I}{B} \end{pmatrix}.$$

The scalar products $\nabla s \cdot \nabla \theta$ and $\nabla s \cdot \nabla \phi$ can be expressed in terms of lower metric elements g_{ij} which are available from TERPSICHORE output, along with the other equilibrium quantities required to calculate the transformation matrices ($|\nabla s|$, I , J , B , \sqrt{s} , ψ' , Φ'). The \widehat{TU} , \widehat{TL} values are thus obtained on the TERPSICHORE grid. Interpolation to the LEMan grid used for perturbations is quite delicate near the axis, where the precision of the equilibrium usually deteriorates. In order to avoid introducing large numerical errors, we extract the main asymptotics of the \widehat{TU} , \widehat{TL} elements near the axis (for example, $\widehat{TU}_{11} \sim \sqrt{s}$, $\widehat{TU}_{22} \sim 1/\sqrt{s}$) and perform the numerical derivation and the

interpolation required for the matrix construction on the remaining slowly varying part. This method helps to improve the convergence of the solution and the power balance near the axis.

It can be easily verified that, in fact, there is no need to calculate \widehat{TL} separately because it is directly related to the matrix \widehat{TU} . On the one hand, we have

$$\vec{A} = A_i^{ph} \vec{e}_i^{ph}, \quad \vec{A} = A_i \vec{e}^i.$$

Using the orthogonality of the physical basis vectors \vec{e}_i^{ph} , we obtain

$$A_j^{ph} = A_i \vec{e}^i \vec{e}_j^{ph} = \widehat{TU}_{ij} A_i.$$

On the other hand, comparing this expression with the definition of the \widehat{TL} matrix

$$A_i = \widehat{TL}_{ij} A_j^{ph},$$

we obtain a simple relation between the two matrices:

$$\widehat{TL} = \left(\widehat{TU}' \right)^{-1},$$

where prime denotes matrix transposition.

Bibliography

- [1] T. Mutoha, R. Kumazawa, T. Seki, et al. Ion cyclotron range of frequencies heating and high-energy particle production in the Large Helical Device. *Nucl. Fusion*, **43**:738, 2003.
- [2] S. Masuda, R. Kumazawa, K. Nishimura, et al. Strong electron heating in CHS ICRF heating experiments. *Nucl. Fusion*, **37**:53, 1997.
- [3] D.A. Hartmann et al. Plasma heating and sustainment in the ion cyclotron range of frequencies on the stellarator W7-AS. *in Fusion Energy 1998 (Proc.17th Conf. Yokohama, Japan), (International Atomic Energy Agency, Vienna, 1999), 2,575*.
- [4] A. Fasoli, D. Testa, S. Sharapov, H. L. Berk, B. Breizman, A. Gondhalekar, R. F. Heeter, M. Mantsinen, and contributors to the EFDA-JET Workprogramme. MHD spectroscopy. *Plasma Phys. Control. Fusion*, **44**:B159, 2002.
- [5] A. B. Mikhailovskii. *Zh. Eksp. Teor. Fiz.*, **68**:1772, 1975.
- [6] M. N. Rosenbluth and P. H. Rutherford. Excitation of Alfvén waves by high-energy ions in a tokamak. *Phys. Rev. Lett.*, **34**(23):1428, 1975.
- [7] K. T. Tsang, D. J. Sigmar, and J. C. Whitson. Destabilization of low mode number Alfvén modes in a Tokamak by energetic or alpha particles. *Phys. Fluids*, **24**(8):1508, 1981.
- [8] G. Y. Fu and J. W. Van Dam. Excitation of the toroidicity-induced shear Alfvén eigenmode by fusion alpha particles in an ignited tokamak. *Phys. Fluids*, **1**(10):1949, 1989.
- [9] C.-Y. Teo, A. Weller, C. Konrad, W7-AS Team, and NBI Team. Further observations of neutral beam driven global Alfvén eigenmodes in Wendelstein W7-AS. *Nucl. Fusion*, **38**(3):409, 1998.

- [10] V.S. Belikov, Ya. I. Kolesnichenko, and V. N. Oraevskij. *Zh. Eksp. Teor. Fiz.*, **55**:2210, 1968.
- [11] Ya. I. Kolesnichenko, V. V. Lutsenko, H. Wobig, Yu. V. Yakovenko, and O. P. Fesenyuk. Alfvén continuum and high-frequency eigenmodes in optimized stellarators. *Phys. Plasmas*, **8**(2):491, 2001.
- [12] C. Nührenberg. Compressional ideal magnetohydrodynamics: Unstable global modes, stable spectra, and Alfvén eigenmodes in Wendelstein 7-X-type equilibria. *Phys. Plasmas*, **6**(1):137, 1999.
- [13] L. Villard, K. Appert, R. Gruber, and J. Vaclavik. Global waves in cold plasmas. *Comput. Phys. Reports*, **4**:95, 1986.
- [14] C. Z. Cheng. Kinetic extensions of magnetohydrodynamics for axisymmetric toroidal plasmas. *Phys. Rep.*, **211**(1):1, 1992.
- [15] A. Jaun, K. Appert, J. Vaclavik, and L. Villard. Global waves in resistive and hot tokamak plasmas. *Comput. Phys. Comm.*, **92**:153, 1995.
- [16] M. Brambilla. Numerical simulation of ion cyclotron waves in tokamak plasmas. *Plasma Phys. Control. Fusion*, **41**(1):1, 1999.
- [17] D. Borba and W. Kerner. CASTOR-K: stability analysis of Alfvén eigenmodes in the presence of energetic ions in tokamaks. *Journ. Comp. Phys.*, **153**:101, 1999.
- [18] H. Qin, W. M. Tang, and G. Rewoldt. Linear gyrokinetic theory for kinetic magnetohydrodynamic eigenmodes in tokamak plasmas. *Phys. Plasmas*, **6**(6):2544, 1999.
- [19] E. F. Jaeger, L. A. Berry, E. D’Azevedo, D. B. Batchelor, and M. D. Carter. All-orders spectral calculation of radio-frequency heating in two-dimensional toroidal plasmas. *Phys. Plasmas*, **8**(5):1573, 2001.
- [20] E. F. Jaeger, L. A. Berry, E. D’Azevedo, D. B. Batchelor, M. D. Carter, K. F. White, and H. Weitzner. Advances in full-wave modeling of radio frequency heated, multi-dimensional plasmas. *Phys. Plasmas*, **9**(5):1873, 2002.

- [21] A. Fukuyama and T. Akutsu. Full wave analysis of ICRF waves and Alfvén eigenmodes in toroidal plasmas. *43rd Annual Meeting of the APS Division of Plasma Physics, Long Beach, California, Oct. 29 - Nov. 2, 2001.*
- [22] V. Vdovin, T. Watari, and A. Fukuyama. 3D Maxwell-Vlasov boundary value problem solution in stellarator geometry in ion-cyclotron frequency range. *Laboratory report NIFS-469, Japan, 1996.*
- [23] O. Fischer, W.A. Cooper, and L. Villard. Magnetic topology and guiding centre drift orbits in a reversed shear tokamak. *Nucl. Fusion*, **40**:1453, 2000.
- [24] R. D. Hazeltine. *Plasma Confinement*. Addison-Wesley Publishing Company, Redwood City, California, 1992.
- [25] A. H. Boozer. Guiding center drift equations. *Phys. Fluids*, **23**(5):904, 1980.
- [26] A. H. Boozer. Plasma equilibrium with rational magnetic surfaces. *Phys. Fluids*, **24**(11):1999, 1981.
- [27] A. H. Boozer. Transport and isomorphic equilibria. *Phys. Fluids*, **26**(2):496, 1983.
- [28] A. H. Boozer. Evaluation of the structure of ergodic fields. *Phys. Fluids*, **26**(5):1288, 1983.
- [29] S. Hamada. Hydromagnetic equilibrium and their proper coordinates. *Nucl. Fusion*, **2**:23, 1962.
- [30] W. D’haeseleer, W. N. G. Hitchon, W. I. van Rij, S. P. Hirshman, and L. Shohet. *Flux Coordinates and Magnetic Field Structure*. Springer Verlag, New York, 1991.
- [31] L. S. Soloviev. *Zh. Eksp. Teor. Fiz.*, **53**:626, 1967.
- [32] S. P. Hirshman. Steepest-descent moment method for three-dimensional magnetohydrodynamic equilibria. *Phys. Fluids*, **26**(12):3553, 1983.
- [33] S. P. Hirshman, W. I. van Rij, and P. Merkel. Three-dimensional free boundary calculations using a spectral Greens function method. *Comput. Phys. Comm.*, **43**:143, 1986.
- [34] S. P. Hirshman and D. K. Lee. MOMCON: A spectral code for obtaining three-dimensional magnetohydrodynamic equilibria. *Comput. Phys. Comm.*, **39**:161, 1986.

- [35] S. P. Hirshman. Improved radial differencing for three-dimensional magnetohydrodynamic equilibrium calculations. *Journ. Comp. Phys.*, **87**:396, 1990.
- [36] S. P. Hirshman and O. Betancourt. Preconditioned descent algorithm for rapid calculations of magnetohydrodynamic equilibria. *Journ. Comp. Phys.*, **96**(1).
- [37] D. V. Anderson, A. Cooper, U. Schwenn, and R. Gruber. Linear MHD stability analysis of toroidal 3D equilibria with TERPSICHORE. *Proc. of the Joint Varenna-Lausanne International Workshop on Theory of Fusion Plasmas (Editrice Compositori, Bologna)*, page 93, 1988.
- [38] D. V. Anderson, W. A. Cooper, R. Gruber, S. Merazzi, and U. Schwenn. Methods for the efficient calculation of the (MHD) magnetohydrodynamic stability properties of magnetically confined fusion plasmas. *Int. J. Supercomput. Appl.*, **4**(3).
- [39] W. A. Cooper. Variational formulation of the linear MHD stability of 3D plasmas with noninteracting hot electrons. *Plasma Phys. Control. Fusion*, **34**(6).
- [40] G. Y. Fu, W. A. Cooper, R. Gruber, U. Schwenn, and D. V. Anderson. Fully three-dimensional ideal magnetohydrodynamic stability analysis of low-n modes and Mercier modes in stellarators. *Phys. Fluids*, **4**(6).
- [41] T. H. Stix. *Waves in Plasmas*. American Institute of Physics, New York, 1992.
- [42] K. Appert, D. Berger, R. Gruber, F. Troyon, and J. Rappaz. *J. Appl. Math. Phys. (ZAMP)*, **25**:229, 1974.
- [43] J. Rappaz. Approximation of the spectrum of a noncompact operator given by the magnetohydrodynamic stability of a plasma. *Numer. Math.*, **28**:15, 1977.
- [44] J. Rappaz. Spectral pollution of a non-compact operator. *Comput. Phys. Comm.*, **24**:323, 1981.
- [45] K. Appert, B. Balet, R. Gruber, F. Troyon, and J. Vaclavik. Numerical problems associated with the presence of continuous spectra. *Comput. Phys. Comm.*, **24**:329, 1981.
- [46] X. Llobet, K. Appert, A. Bondeson, and J. Vaclavik. On spectral pollution. *Comput. Phys. Comm.*, **59**:199, 1990.

- [47] R. Gruber. Finite hybrid elements to compute the ideal magnetohydrodynamic spectrum of an axisymmetric plasma. *Journ. Comp. Phys.*, **26**:379, 1978.
- [48] E. Yamashita. *Analysis Methods For Electromagnetic Wave Problems*. Artech House Books, 1990.
- [49] G. W. Wei. Discrete singular convolution for the solution of the Fokker-Planck equation. *J. Chemical Phys.*, **110**(18):8930, 1999.
- [50] A. Jaun. *Linear wave propagation in a hot axisymmetric toroidal plasma*. PhD thesis, EPFL, 1995.
- [51] J. Vaclavik and K. Appert. Theory of plasma heating by low frequency waves: magnetic pumping and Alfvén resonance heating. *Nucl. Fusion*, **31**(10):1945, 1991.
- [52] Th. J. R. Hughes. *The Finite Element Method. Linear Static and Dynamic Finite Element Analysis*. Prentice-Hall, London, 1987.
- [53] E. Tennfors. Two-ion ICRF heating in tokamaks. *Plasma Phys. Control. Fusion*, **28**(9B):1483, 1986.
- [54] National Energy Research Scientific Computing Center, Annual report. 2003.
- [55] S. Wolfram. *Mathematica*. Cambridge University Press, 1999.
- [56] L. Villard. *Propagation et absorption d'ondes aux frequences d'Alfvén et cyclotroniques ioniques dans les plasmas toriques*. PhD thesis, EPFL, 1987.
- [57] J. D. Jackson. *Classical Electrodynamics*. Wiley Text Books, 1998.
- [58] K. Appert, J. Vaclavik, and L. Villard. Spectrum of low-frequency, nonaxisymmetric oscillations in a cold, current-carrying plasma column. *Phys. Fluids*, **27**(2):432, 1984.
- [59] A. de Chambrier, A. D. Cheetham, A. Heym, F. Hofmann, B. Joye, R. Keller, A. Lietti, J. B. Lister, and A. Pochelon. Alfvén wave coupling experiments of the TCA tokamak. *Plasma Phys.*, **24**:893, 1982.
- [60] K. Appert, R. Gruber, F. Troyon, and J. Vaclavik. Excitation of global eigenmodes of the Alfvén wave in Tokamaks. *Plasma Phys.*, **24**(9):1147, 1982.

- [61] D. W. Ross, G. L. Chen, and S. M. Mahajan. Kinetic description of Alfvén wave heating. *Phys. Fluids*, **25**(4):652, 1982.
- [62] C. Z. Cheng and M. S. Chance. Low-n shear Alfvén spectra in axisymmetric toroidal plasmas. *Phys. Fluids*, **29**(11):3695, 1986.
- [63] F. Zonca and L. Chen. Resonant damping of toroidicity-induced shear-Alfvén eigenmodes in Tokamaks. *Phys. Rev. Lett.*, **68**(5):592, 1992.
- [64] D. Testa, G.Y. Fu, A. Jaun, A. Fasoli, O. Sauter, and JET-EFDA contributors. Experimental test of damping models for $n = 1$ toroidal Alfvén eigenmodes in JET. *Nucl. Fusion*, **43**:479, 2003.
- [65] A. Fasoli, D. Borba, G. Bosia, D. J. Campbell, J. A. Dobbing, C. Gormezano, J. Jacquinet, P. Lavanchy, J. B. Lister, P. Marmillod, J.-M. Moret, A. Santagiustina, and S. Sharapov. Direct measurement of the damping of toroidicity-induced Alfvén eigenmodes. *Phys. Rev. Lett.*, **75**:645, 1995.
- [66] A. Fasoli, D. Borba, B. Breizman, C. Gormezano, R. F. Heeter, A. Jaun, M. Mantsinen, S. Sharapov, and D. Testa. Fast particles-wave interaction in the Alfvén frequency range on the Joint European Torus tokamak. *Phys. Plasmas*, **7**(5):1816, 2000.
- [67] L. L. Lao, H. St. John, R. D. Stambaugh, A. G. Kellman, and W. Pfeiffer. Reconstruction of current profile parameters and plasma shapes in tokamaks. *Nucl. Fusion*, **25**(11):1611, 1985.
- [68] H. Lütjens, A. Bondeson, and A. Roy. Axisymmetric MHD equilibrium solver with bicubic Hermite elements. *Comput. Phys. Comm.*, **69**(2-3):287, 1992.
- [69] K. G. Budden. *Radio Waves in the Ionosphere: The Mathematical Theory of the Reflection of Radio Waves from Stratified Ionised Layers*. Cambridge University Press, London, 1961.
- [70] N. Mellet. *Détermination des surfaces magnétiques résonantes d'Alfvén dans des configurations 2D et 3D*. Diploma project report, CRPP, EPFL, 2004.
- [71] J. Nührenberg and R. Zille. Quasi-helically symmetric toroidal stellarators. *Phys. Lett. A*, **129**(2):113, 1988.

- [72] J. Nührenberg, W. Lotz, and S. Gori. Quasi-axisymmetric tokamaks. *Theory of Fusion Plasmas*, E. Sindoni, F. Troyon and J. Vaclavik eds., SIF, Bologna, 1994.
- [73] P. R. Garabedian. Stellarators with the magnetic symmetry of a tokamak. *Phys. Plasmas*, **3**(7):2483, 1996.
- [74] K. Matsuoka S. Okamura, M. Fujiwara, M. Drevlak, P. Merkel, and J. Nührenberg. Post-chs project. *Plasma Phys. Rep*, **23**(7):542, 1997.
- [75] H. E. Mynick, T. K. Chu, and A. H. Boozer. Class of model stellarator fields with enhanced confinement. *Phys. Rev. Lett.*, **48**:322, 1982.

Acknowledgments

I am deeply grateful to my thesis supervisor Anthony Cooper who has helped me a lot in accomplishing this work. He has always been available and willing to share his immense knowledge of the stellarator physics and the aspects of 3D geometry. It was a real pleasure to work with him.

I am particularly indebted to Laurent Villard, whose help in understanding the physics of the wave propagation can not be underestimated. He has always found a very clear way to explain the complicated physics and to introduce me to the field of plasma waves. His encouragement and confidence were extremely valuable to me, and discussions with him have always been very interesting and motivating.

Special thanks go to André Jaun. Many ideas implemented in this thesis were inspired by his work. His help during the first several months of the thesis was of great importance to me.

I would also like to thank Dr. Sergei Medvedev from the Keldysh Institute of Applied Mathematics for his valuable advice on the numerical implementation of the code. An important contribution to the visualisation of the complicated 3D data was made by Dr. Jean Favre from the Centro Svizzero di Calcolo Scientifico, and Dr. Francesco Benvenuto gave some advice on the code optimisation. I thank them for their help.

I also thank Dr. O. Sauter, Prof. A. Fasoli, Dr. D. Testa and Prof. A. Jaun for providing the experimental JET data that were used here for comparisons.

I am grateful to Prof. H. Brune, Dr. W.A. Cooper, Prof. A. Jaun, Prof. V.D. Shafranov, Prof. M. Deville and MER L. Villard who honoured me by accepting to be the members of my thesis jury.

I thank Prof. M.Q. Tran and Dr. K. Appert who have given me the opportunity to work in the CRPP.

My special thanks go to Edith Grüter, Paula Halter and the CRPP secretariat for their very efficient work that has always been of great help.

Finally, I would like to thank my parents for their support, Nathalie for her patience especially during the last stressful months of the thesis and all my friends both in the CRPP and outside who have made these years a very enjoyable time which I will always remember with pleasure.

This work was partly supported by the Swiss National Science Foundation.

Curriculum vitae

Pavel Popovitch

- 30.05.1976 Born in Moscow, Russia.
- 1983 – 1993 Primary and secondary school, Moscow.
- 1993 – 1999 University studies at the Plasma Physics Department,
Moscow State Engineering & Physics Institute (Technical University).
Diploma project at the Plasma Theory Division, Nuclear Fusion Institute,
Russian Research Center "Kurchatov Institute".
Degree: Engineer-physicist.
- 1999 – 2004 Research and assistantship at the
Centre de Recherches en Physique des Plasmas (CRPP),
Swiss Federal Institute of Technology (EPFL), Lausanne, Switzerland.